Department Chemie
der Technischen Universität München

Density Functional Studies
Relevant to Methanol Steam Reforming on PdZn

Kok Hwa Lim

Vollständiger Abdruck der von der Fakultät für Chemie der Technischen Universität München zur Erlangung des akademischen Grades eines

Doktors der Naturwissenschaften (Dr. rer. nat.)

genehmigten Dissertation.

Vorsitzender: Univ.-Prof. Dr. Klaus Köhler
Prüfer der Dissertation:

1. Univ.-Prof. Dr. Notker Rösch
2. Univ.-Prof. Dr. Johannes A. Lercher

Die Dissertation wurde am 17 Januar 2006 bei der Technischen Universität München eingereicht und durch die Fakultät für Chemie am 13 Februar 2006 angenommen.

Gedruckt mit Unterstützung des Deutschen Akademischen Austauschdienstes

In memory of my parents

For Nicole and Emma

"The LORD Will Provide"

Genesis 22:14

God will make the way
When there seems to be no way
He works in ways we cannot see
He will be my guide
Hold me closely to his side
With love and strength for each new day
He will make a way

(Integrity's Hosanna! Music, 1999)

"Trust in the LORD with all your heart
and lean not on your own understanding;
in all your ways acknowledge him,
and he will make your paths straight."

Proverbs 3:5-6

Acknowledgements

First and foremost, I would like to thank my Doktorvater, Prof. Dr. Notker Rösch for giving me the opportunity to do my doctoral thesis in his research group. I am grateful for his support throughout these years.

I would also like to thank Priv.-Doz. Prof. Dr. Konstantin M. Neyman for his guidance and Prof. Dr. Zhao Xu Chen who had not only introduced me to this topic, but also taught me to run VASP code on various platforms. The many discussions with Dr. L. V. Moskaleva and Dr. I. V. Yudanov were greatly appreciated. I thank Dr. S. Krüger for the many administrative supports and scientific discussions.

I appreciate the camaraderie shared among the past and present research group members: Dr. A. Gordienko, Dr. R. Deka, A. Deka, M. Suzen, Dr. G. N. Vayssilov, R. S. Ray, Dr. F. Schlosser, A. Genest, Dr. V. Nasluzov, Dr. A. Matveev, Dr. D. Ganyushin, S. Bosko, E. Vladimirov, A. Kremleva, Dr. K. Siriwong, Dr. C. Inntam, Dr. P. Chuichay, Dr. C. Bussai, Dr. S. Majumder, A. B. Mohammad, Dr. G. M. Xiong, Dr. G. Jezierski and those not mentioned here. They have not only made my stay here enjoyable, but also taught me many things.

I am grateful too, for the doctoral fellowship from Deutscher Akademischer Austauschdienst (DAAD). The staff from DAAD was helpful during my application in Singapore and during my stay in Germany. The German language courses sponsored by DAAD at the beginning of the fellowship have enriched my awareness of the German culture, hence making my stay in Germany much easier. Financial support from Deutsche Forschungsgemeinschaft is also gratefully acknowledged.

I am indebted to my in-laws, brother, relatives and friends for their constant support throughout the years. Many of them visited us in Munich to make us less homesick. I would also like to thank my friend Wai Kiong, for sharing his German educational experience with me, without which, I would not know such a wonderful place to further my education. The Singaporean students in Munich were very helpful during my settling down period here.

Most importantly, I thank my wife Nicole for her unfailing love, patience and understanding. She has also been a great source of encouragement in my spiritual growth. Last but not least, my special thanks to Emma, who unknowingly inspires me with her strengths and surprises me daily with her joy.

Kok Hwa LIM
Munich, Germany
January 2006

Zusammenfassung

Die Zersetzung von Methoxid durch Bruch von C-H- bzw. C-O-Bindungen wurde für die Oberflächen (111), (100) und (221) einer 1:1 Pd-Zn Legierung mit einer Dichtefunktional-Methode untersucht. Zum Vergleich wurden auch Rechnungen für Cu(111) und Pd(111) durchgeführt. Für die drei PdZn-Oberflächen wurde gefunden, dass der Bruch einer C-H-Bindung leichter vonstatten geht als derjenige der C-O-Bindung. Auf planaren PdZn-Oberflächen ist die Spaltung der C-H-Bindung langsam, die Aktivierungsbarriere E_a beträgt ~90 kJ mol^{-1}. Aber diese Reaktion läuft wesentlich schneller an einer Pd-Stufe der PdZn(221) Oberfläche ab (E_a ~ 50 kJ mol^{-1}). Auf PdZn(111) ist die Desorption von Formaldehyd kinetisch bevorzugt gegenüber einer Dehydrogenierung. Die Reaktivitäten entsprechender Oberflächen einer PdZn-Legierung und Cu sind insgesamt recht ähnlich. Gemäß einer thermodynamischen Analyse ist PdZn(111) unter den Bedingungen der Methanol-Dampfreformierung am wahrscheinlichsten mit OH-Adsorbaten bedeckt.

Abstract

The decomposition of methoxide, specifically the cleavage of C-H and C-O bonds, was studied by density functional calculations for various surfaces of the 1:1 PdZn alloy: (111), (100) and the stepped surface (221). For comparison, these reactions were also investigated on Pd(111) and Cu(111). On all three PdZn surfaces addressed, scission of C-H bonds was determined to be more favorable than breaking of the C-O bond. On flat PdZn surfaces, C-H bond cleavage of methoxide is slow, with activation barriers E_a of ~90 kJ mol^{-1}, but the reaction becomes much faster on the Pd step of PdZn(221) where E_a ~ 50 kJ mol^{-1}. On PdZn(111), dehydrogenation of formaldehyde is kinetically less favorable than its desorption. Overall, the reactivity of PdZn alloy surfaces of was found to be similar to that of the corresponding Cu surfaces. According to a thermodynamic analysis, OH is the most likely water-related species present on PdZn(111) under the conditions of methanol steam reforming.

Contents

List of abbreviations

BE	Binding energy
CI	Configuration interaction
DF	Density functional
FS	Final state
GGA	Generalized gradient approximation
HREELS	High-resolution vibrational electron loss spectroscopy
IRAS	Reflection-adsorption IR spectroscopy
IS	Initial state
KS	Kohn Sham theory
LEED	Low energy electron diffraction
MEP	Minimum energy path
MSR	Methanol steam reforming
NEB	Nudged elastic band
PAW	Projector-augmented wave
PED	Photoelectron diffraction
RWGS	Reverse water gas shift
STM	Scanning tunneling microscopy
TPD	Temperature programmed desorption
TS	Transition state
UHV	Ultra-high vacuum
UPS	Ultraviolet photoelectron spectroscopy
VASP	Vienna ab initio simulation package
WGS	Water gas shift
XPS	X-ray photoelectron spectroscopy
ZPE	Zero point energy

Chapter 1
Introduction

Increasing regulations on the emission of air pollutants have stimulated interest in fuel cells, which use hydrogen as energy source, in particular for vehicles [1,2]. One strategy of hydrogen production relies on an efficient *in situ* conversion of methanol to hydrogen [3]. A typical process for this purpose is methanol steam reforming (MSR), $CH_3OH + H_2O \rightarrow H_2 + CO_2$ [1,2]. The commonly used catalyst for this reaction is Cu/ZnO; its active component has been assigned to metallic Cu [4]. However, Cu/ZnO is not stable at elevated temperatures above 600 K because of metal sintering [2]. Recently, a Pd/ZnO catalyst has been found to have an activity and selectivity for methanol steam reforming comparable to that of Cu/ZnO [5]. It exhibits good thermal stability and its reactivity differs significantly from that of metallic Pd [5]: on Pd/ZnO (and Cu/ZnO) the main products are carbon dioxide (CO_2) and hydrogen (H_2), whereas carbon monoxide (CO) and H_2 are selectively produced on Pd. This difference between Pd/ZnO and Pd has been ascribed to the formation of Pd-Zn alloys [5–7]. Recent studies identified 1:1 Pd-Zn alloy (denoted as PdZn hereafter) as one of the active components of the novel Pd/ZnO catalysts [8].

Methanol steam reforming is established to begin with the formation of adsorbed methoxide species, CH_3O, (Fig. 1.1 – reaction 1) which decompose further on [5]. This postulate regarding methoxide as important stable intermediate in methanol transformations is supported by surface science experiments, which found stable methoxide species on various transition metals surfaces [9]. Two reaction pathways are possible for methoxide decomposition (Fig. 1.1): (a) C-H bond breaking that leads to the formation of formaldehyde (CH_2O) (reaction 2) and (b) C-O bond scission which results in stable adsorbed methyl (CH_3) species (reaction 3) [10–14]. Apparently, the reaction system can follow both pathways, depending on the catalyst composition and the surface structure. Molecular beam

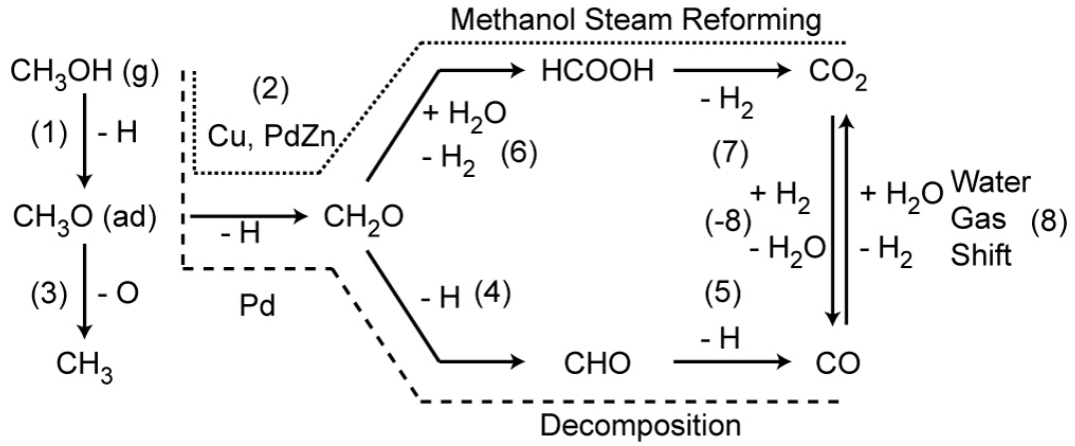

Figure 1.1. Possible reaction pathways suggested by Iwasa et. al. [5] for methanol decomposition and steam reforming reaction on Pd, Cu and PdZn catalysts.

investigations combined with time-resolved reflection-adsorption IR spectroscopy (IRAS) showed that dehydrogenation of methoxide to carbon monoxide represents the dominating reaction channel on Pd metal surfaces [15]. On the other hand, C-O bond scission had been reported to proceed at much lower rates, eventually forming hydrocarbon (CH_x) or carbon (C) species, corroborating that C-H bond breaking of methoxide is the main reaction pathway on Pd surfaces [12,16]

The reaction behavior of methoxide on Zn surfaces is different from that on Pd surfaces. X-ray (XPS) and ultraviolet photoelectron spectroscopy (UPS) as well as high-resolution vibrational electron energy loss spectroscopy (HREELS) investigations on the interaction of methanol with Zn surfaces revealed that hydrogen abstraction from methanol occurs first to give methoxide species, followed by scission of the C-O bond and subsequent formation of hydrocarbons [17]. Therefore, in contrast to the situation on Pd surfaces where C-H breaking of methoxide prevails, exclusively C-O bond cleavage apparently takes place on Zn surfaces. Because decomposition of methoxide occurs differently on monometallic Pd and Zn surfaces, one of the crucial questions concerning methanol steam reforming over PdZn catalysts is whether both C-H and C-O bonds of methoxide can break on this substrate under typical reaction conditions, and if so, which of the two bonds is easier to break. It is important to address the decomposition of methoxide because the C-H bond breaking of this intermediate is commonly thought to be the rate-limiting step of methanol decomposition and steam reforming reactions [9-13,18].

When methanol was replaced by formaldehyde as reactant, similar products of methanol decomposition and MSR were obtained over the Pd and PdZn alloy catalysts [5]. This suggests that formaldehyde is another crucial intermediate that determines the selectivity of the steam reforming reaction. Indeed (see Fig. 1.1), formaldehyde can either undergo decomposition to formyl species (reaction 4) and then decompose further to carbon monoxide (reaction 5) or it can react with water related species to form formic acid (HCOOH) intermediate (reaction 6), which subsequently decomposes to carbon dioxide (reaction 7).

Fuel cells currently used in vehicles are very sensitive to poisons, especially to carbon monoxide, which even at the ppm level has a detrimental effect on the performance of the fuel cell [19]. Water gas shift (WGS) (Fig. 1.1, reaction 8) and reverse water-gas shift (RWGS) reactions (Fig. 1.1, reaction -8) are shown to be negligibly slow on the PdZn catalyst during MSR reactions to convert carbon dioxide to carbon monoxide and vice versa [20]. The observed production of carbon monoxide has been exclusively assigned to the methanol decomposition which occurs in parallel to MSR reaction [20]. Therefore, a detailed understanding of the mechanism of methanol decomposition is necessary to provide indispensable guiding information for designing and producing new, more efficient steam reforming catalysts that do not promote formaldehyde decomposition (reaction 4), which would lead to the undesirable carbon monoxide.

On a group VIII metal (e.g. Pt, Pd), the formation of carbon dioxide under steam reforming conditions has been attributed to methanol decomposition followed by the WGS reaction (Fig. 1.1, reactions 1, 2, 4, 5, 8) [21]. However, the actual active species of WGS reaction is unclear, in particular, whether adsorbed carbon monoxide reacts with surface oxygen or hydroxyl groups that lead to the formation of carbon dioxide [22]. At variance with the group VIII metals, kinetic studies on Cu and PdZn alloy catalysts have excluded WGS reaction as the main source of carbon dioxide formation under MSR conditions [18,20,21]. It has been proposed that methanol is converted directly to carbon dioxide through formic acid type of intermediates [18,21]. The mechanism of formaldehyde reacting with water related species to form formic acid intermediate (reaction 6), which subsequently decomposed to carbon dioxide (reaction 7) was supported by scanning tunneling microscopy (STM) experiments [23,24] and density functional (DF) cluster calculations on Cu surfaces [25,26]. STM data showed that formaldehyde reacts with surface oxygen on the Cu(110) surface to form dioxymethylene (H_2COO), which decomposes to formate (HCOO) [23]. The latter species was observed as an intermediate that forms carbon dioxide during formic acid

decomposition on the Cu(110) surface [24]. These experimental reaction pathways involving reaction of formaldehyde with surface oxygen and subsequent decomposition of the intermediates have been supported by DF cluster studies on Cu(111) surface [25,26]. Results of the DF calculations showed that the reaction $CH_2O_{(a)} + O_{(a)} \rightarrow H_2COO_{(a)}$ on the Cu(111) surface is exothermic with a low reaction barrier [25]. In addition, the reactions $H_2COO_{(a)} \rightarrow HCOO_{(a)} + 1/2\ H_{2\ (g)}$ and $HCOO_{(a)} \rightarrow CO_{2\ (g)} + 1/2\ H_{2\ (g)}$ were calculated to be exothermic on the Cu(111) surface [26]. Although possible reaction pathways for formaldehyde to carbon dioxide have been postulated [25,26], it is not clear whether surface oxygen is present on the catalyst surface under MSR conditions.

A recent review on H_2O interaction with surfaces [27] reports that H_2O dissociates on clean Cu(111) [28], but absence of H_2O dissociation has also been claimed [29]. On the other hand, there are no observations of H_2O dissociation on clean Pd(111) and Pt(111) surfaces. The observed H_2O dissociation at clean Cu(111) surface is likely due to oxygen impurities [30]. This is supported by the observation that the H_2O dissociates on a Cu(111) surface with oxygen impurities [30]. Also, an OH phase is formed by reacting H_2O with surface O on Ag(110) [31] and Pt(111) [32]. All these observations are in agreement with recent periodic DF calculations [33] that H_2O dissociation reactions, $H_2O_{(a)} \rightarrow OH_{(a)} + H_{(a)}$ and $H_2O_{(a)} + O_{(a)} \rightarrow 2OH_{(a)}$, are exothermic on Cu(111), but endothermic on Pt(111). However, $OH_{(a)} \rightarrow H_{(a)} + O_{(a)}$ is endothermic on both Cu(111) and Pt(111) surfaces. Because H_2O exhibits such diverse dissociation behavior on Cu and Pt catalysts, it is important to characterize the type of H_2O related species present on the bimetallic PdZn alloy surface, in particular under MSR conditions, to obtain a complete understanding of all the elementary reaction steps on the bimetallic PdZn alloy surface.

The goals of the present work were

(1) to determine the effects of surface morphology on the rate determining steps of MSR,
(2) to determine conditions where the production of the undesirable CO is minimized, and
(3) to determine likely H_2O-related species responsible for CO_2 production during MSR.

This dissertation is organized as follows. In Chapter 2, theoretical background and the computational method used are presented. In Chapter 3, structure and adsorption energies of various adsorption complexes on the (111) surfaces of Pd, Cu and PdZn alloy are discussed. Also, the reactivity of methoxide decomposition on these surfaces is considered as our

idealized substrates for the complex surface structures of real catalysts. In Chapters 4 and 5, we bridge the "material gap" of real catalysts surface by studying the effects of the more open (100) surface and the stepped (221) surface of the PdZn alloy on the reactivity of methoxide decomposition. Chapter 6 is devoted to formaldehyde decomposition to delineate peculiarities in the reactivity of this species on Pd(111) and Cu(111) metals in comparison to reactions on PdZn(111) alloy. Thermodynamic and kinetic arguments are presented in Chapter 7 to close the "pressure gap" between DF calculations and realistic catalyst systems for the most probable H_2O related components on PdZn(111) and Cu(111) under MSR conditions. Finally, our results are summarized in Chapter 8.

Chapter 2

Computational Details and Theoretical Background

First principles electronic structure calculations contain no external parameters other than a most basic description of the system. Such calculations allow one to predict the thermochemistry and activation barriers of model reaction systems in comparison to experimental data. It also enables one to understand physical properties, such as the binding energy of an atom or a molecule, motivated in particular by the possibility to produce reliable data [34]. First principles electronic structure calculations are referred to as *ab initio* calculations in the physics community. Such calculations are based on quantum mechanics developed in the early 1920s. In 1926, Heisenberg developed the matrix mechanics [35] and Schrödinger proposed the basic non-relativistic wave equation governing the motion of nuclei and electrons in molecules [36]. The Schrödinger equation is easily solved for the hydrogen; with the inclusion of relativistic effects via the Dirac equation [37], theoretical results are in almost perfect agreement with experimental spectroscopic data [35]. However, the exact solution of wave equations is impossible for other systems and only numerical solutions are available.

In this work, the electronic structure calculations were carried out at the density functional (DF) level [38,39]. The idea of describing the total energy as a functional of electron density started from the Thomas-Fermi and Thomas-Fermi-Dirac models of atoms [40], but became established for molecules only when Hohenberg and Kohn [38] showed that the energy of a system is a unique functional of the density. Kohn and Sham (KS) [39] then established the framework of modern Density Functional Theory in the form which is now routinely applied to chemical systems. KS theory in principle allows one to solve the Schrödinger wave equation to obtain the exact ground state energy. However, the exact form of the exchange-correlation potential V_{xc} of KS theory is not known and

approximations have to be used instead, e.g. the generalized gradient approximation (GGA), or hybrid functionals [41].

2.1 Computational Details

All calculations described in the subsequent chapters were performed with the plane-wave based Vienna *ab initio* simulation package (VASP) [42–44] using GGA in the form of the exchange-correlation functional PW91 [45]. The interaction between atomic cores and electrons was described by the projector augmented wave method [46,47]. For integrations over the Brillouin zone, we combined (5×5×1) Monkhorst-Pack grids [48] with a generalized Gaussian smearing technique [49]. We adopted an energy cut-off of 400 eV throughout which, according to our test calculations of CO on Pd(111), guarantees convergence of binding energies to better than 1 kJ mol^{-1} (see Fig. 2.1). All atomic coordinates of the adsorbates were optimized until the force acting on each atom was less than 0.1 eV/ nm.

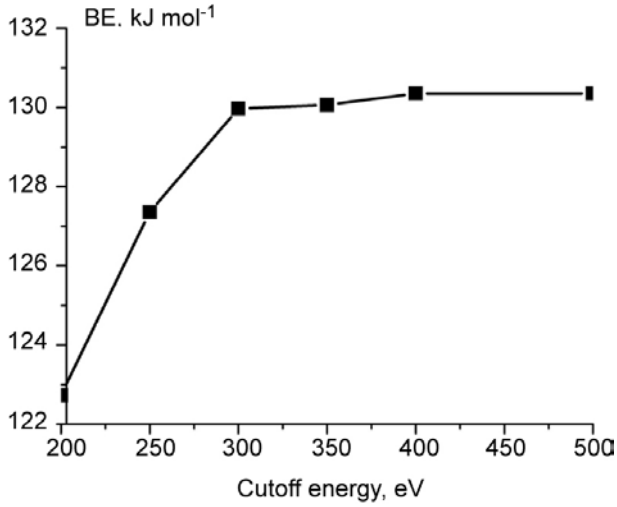

Figure 2.1. Dependence of CO binding energy on Pd(111) surface on the energy cutoff applied, using a surface coverage of 1/3. The Pd(111) surface was modeled by a slab of four metal layers.

2.2 Surface Models

The metals Cu and Pd exhibit a face-centered cubic crystal structure with optimized lattice parameters of 362.8 pm and 395.4 pm respectively, compared to experimental values of 361.5 pm (Cu) and 389.1 pm (Pd) [50]. The (1:1) PdZn alloy features the tetragonal structure of CuAu ($L1_0$-type) which belongs to space group $P4/mmm$ [51]; its optimized lattice parameter is 414.8 pm (experimental value 411 pm) with the c axis shortened compared to the cubic structure (c/a = 0.816) [50].

The substrates were modeled by four-layer slabs as justified by our test calculations. They showed that for such slab models the binding energy of CO on Pd(111) has converged to about ±2 kJ mol^{-1} (see Fig. 2.2). Thus, four-layer slab models represent an acceptable compromise between accuracy and computational economy. The unit cells consist of four atoms per layer for the (111) and (100) surfaces and 8 atoms per layer for the (221) surface; these models enabled us to consider surface coverages as low as 1/4 for the (111) and (100) surfaces and 1/8 for the (221) surface. A vacuum spacing of ~1 nm was adopted to separate the periodically repeated slabs. Adsorbates were positioned on one side of each slab. Specific details of the chosen surface models and the adsorption sites studied are given in the various chapters.

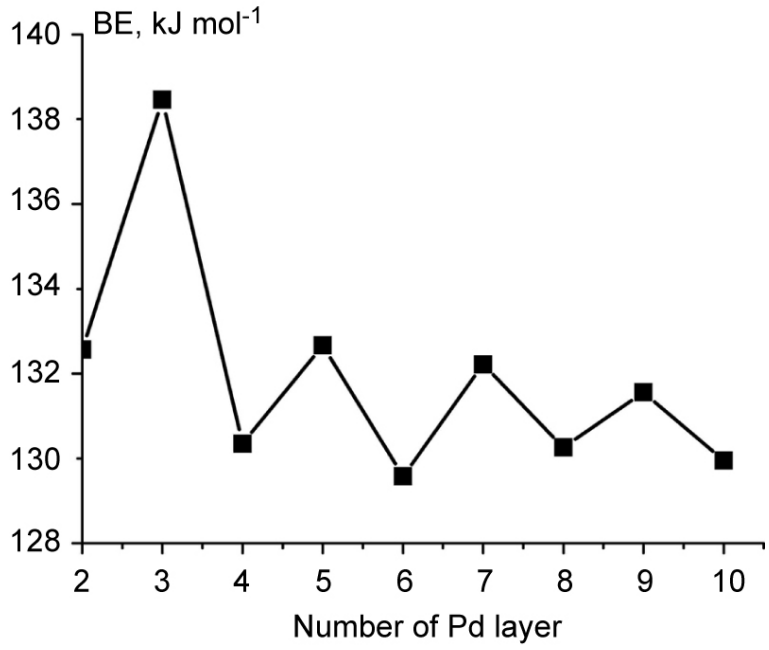

Figure 2.2. CO adsorption energy on fcc sites of Pd(111) slab as a function of the number of metal layers. The surface coverage in these test calculations is 1/3.

2.3 Transition State Search

Transition states (TS) of reactions were located using the nudged elastic band (NEB) method [52]. According to this method, the search for a TS is initiated by interpolating a series of structures (images) between the initial state (IS) and the final state (FS). The transition state search is then transformed into a minimization problem by defining an object function

$$S(\vec{R}_1,.....,\vec{R}_{P-1}) = \sum_{i=0}^{P} V(\vec{R}_i) + \sum_{i=1}^{P} \frac{k}{2}(\vec{R}_i - \vec{R}_{i-1})^2 . \qquad (2.3.1)$$

Here, the first sum is over the "true" potential of all intermediate images of the system, and the second sum is the "spring energy" associated with springs that keep adjacent images together. The initial and final images are kept fixed throughout the search. The structures of all images are then optimized in parallel, to map the minimum energy path (MEP). For each image and in each optimization iteration, the forces on the nuclei are decomposed into components normal to and along the reaction path under investigation. The parallel component of the "true force" is set to zero to prevent the images from sliding down to either IS or FS structures while the perpendicular component of the "spring force" is projected out to avoid a "corner cutting" problem where a stiff spring constant causes the MEP search to miss the saddle point region and overestimate the barrier [53]. A NEB calculation yields a MEP and the highest point along that path is the TS.

Finally, we use a normal mode analysis to verify that the TS obtained from the NEB method exhibits exactly one imaginary frequency. The vibrational frequencies were obtained by diagonalizing the Hessian matrix which was approximated via finite differences of forces, determined by displacing each center of the adsorbates ±3 pm along each of the Cartesian coordinates as implemented in VASP [42–44]. In this approximation, the effects of the substrate on the vibration frequencies are deemed to be small and hence neglected by keeping the substrate fixed during the frequency calculation.

2.3.1 Application of Nudged Elastic Band Method

Before starting a TS search, one has to determine the IS and FS of the reaction (see the flow chart in Fig. 2.3). Usually, the most stable adsorbed structure of the reactant is chosen as IS

and the most stable co-adsorbed complexes of the products are chosen as FS. For instance, for methoxide C-O bond breaking on Cu(111), in the IS methoxide is located at an fcc site and, in the FS, methyl and hydrogen are located at fcc sites.

During the implementation of the NEB method for searching a TS, we noted that using many images to map the MEP requires a large amount of computational time because images obtained from linear interpolation between IS and FS structures usually are poor approximations; thus, often many geometry optimizations were required for each image. To obtain better starting approximations for the images, we reduced the surface models to one substrate layer, vacuum thickness to 0.7 nm, and the energy cutoff to 300 eV. In addition, we modified the search strategy as in most cases we were not interested in mapping the full MEP, but only in locating a transition state. In addition to these restrictions, we used only one image for each NEB calculation. Afterwards, we analyzed the structure (e.g.. for C-O bond breaking, by comparing the C-O bond distance to the values in the IS and FS structures, by inspecting the movement of the O atom or the methyl moiety with respect to the IS) and the total energy (whether the energy is near a value reported in the literature for the barrier of a similar system) of the optimized image to see whether it was to be used as initial or final structure for the next image search. Usually 7 to 8 images were required before an approximate TS (TS^{approx}) was obtained, i.e. a structure that represents a barrier and a bond breaking geometry similar (±20 pm) to values reported in the literature for comparable systems; a normal mode analysis was used to confirm that the obtained structure approximated a TS.

Once TS^{approx} is found, we moved to the full surface model described in Section 2.2. Here, we again begin with the search with one image at a time, using the TS structure obtained from the one-layer slab model as starting point for the TS search, while IS is the most stable reactant structure and FS is the most stable co-adsorbed products. Again after optimization, we determine if the optimized structure belongs to the final state or the initial state structure. Thereafter, the optimized structure and the TS^{approx} structure were used as images for the next NEB search and so on. Usually, the TS structure was obtained with about 4 images.

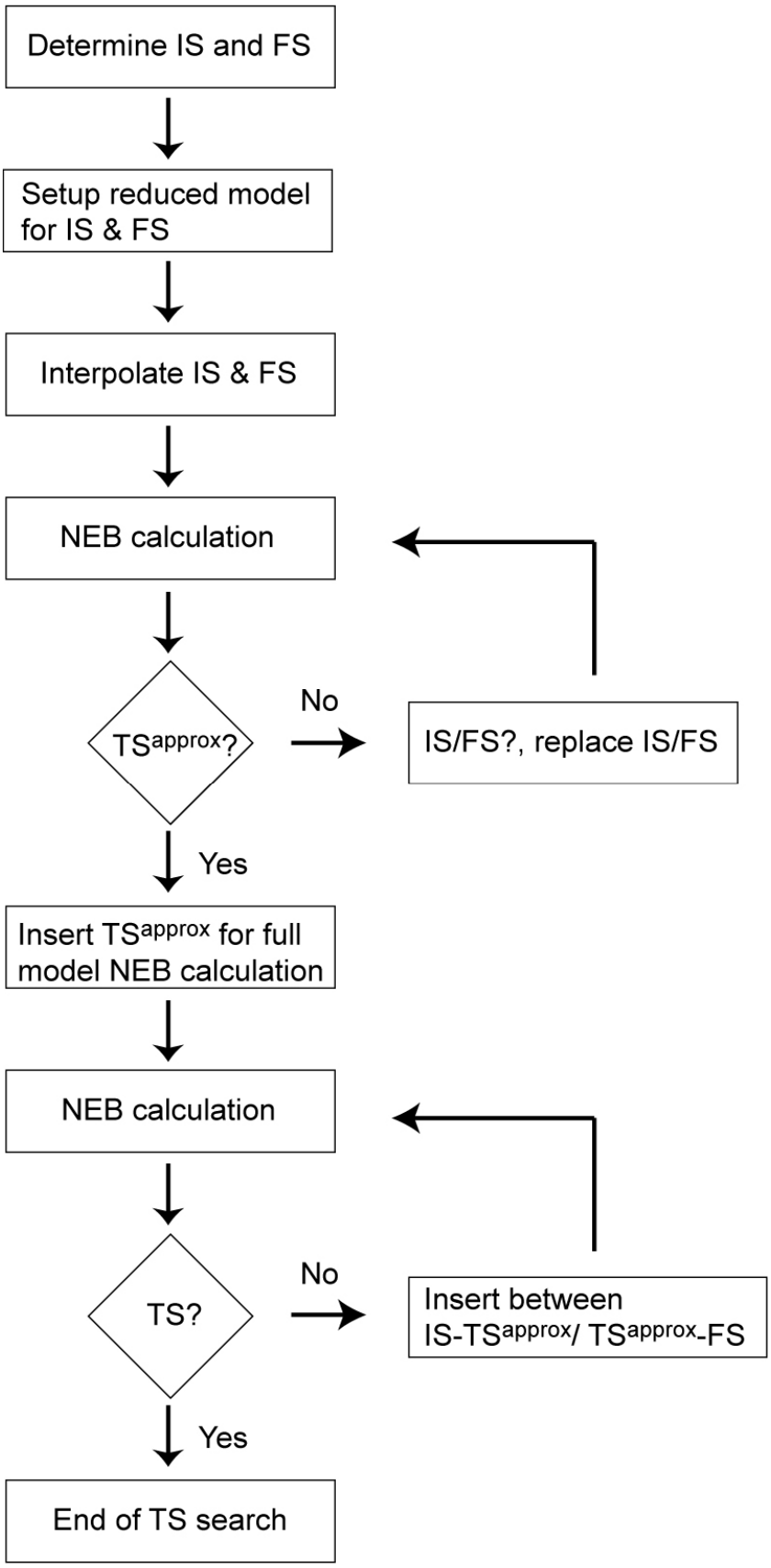

Figure 2.3. Flow chart describing essential steps of a transition state search.

2.4 Definition of Basic Observables/ Parameters

2.4.1 Binding Energy

The binding energy (BE) of an adsorbate to a substrate is calculated according to the expression

$$BE = E_{ad} + E_{sub} - E_{ad/sub}\,, \tag{2.4.1}$$

where $E_{ad/sub}$ is the total energy of the slab model, covered with the adsorbate in the optimized geometry, E_{ad} and E_{sub} are the total energies of the adsorbate in the gas phase and of the clean substrate, respectively. With this definition, a positive value implies a release of energy or a favorable adsorption.

2.4.2 Reaction Rate

The rate constant κ and the pre-exponential factor A^0 of a uni-molecular decomposition reaction of an adsorbed species on a surface were calculated using conventional transition state theory [54]:

$$\kappa = \frac{k_B T}{h}\frac{q^*}{q}e^{-E_a/RT} = A^0 e^{-E_a/RT}\,. \tag{2.4.2}$$

Here, k_B is the Boltzmann constant, h is Planck's constants; E_a is the activation energy corrected for zero-point vibrational energies, and R is the gas constant. At a given temperature T, the pre-exponential factor A^0 is determined by the partition functions q^* for the TS and q for the initial state (IS). Partition functions of adsorbed species contain neither translational nor rotational contributions and the electronic contribution is unity as the electronic energy level difference usually is of the order of 1 eV [55]. All vibrational modes corresponding to displacements of the atoms of the adsorbates, both with respect to each other and to the substrate, were computed in the harmonic approximation [55].

Chapter 3

Methoxide Decomposition on (111) Surfaces of Pd, Cu and PdZn

In this chapter, employing density functional slab models, we study two competing decomposition pathways of adsorbed methoxide species (see Fig. 1.1), namely dehydrogenation to formaldehyde (reaction 2) and C-O bond breaking to methyl (reaction 3). This study aims to contribute to the understanding of these reaction mechanisms. These two reactions are deemed crucial to the MSR process, because dehydrogenation of methoxide to formaldehyde is commonly believed to be the rate determining step [9-13,18].

Although real catalysts feature complex surface structures, it is nevertheless useful to study the mechanism of elementary reaction steps for idealized model surface systems, e.g. single-crystal surfaces, if only for reference purposes [56]. We pursue this model strategy as a first step toward understanding the reactivity of more complex surfaces of PdZn alloy catalysts; see the two following chapters. In the present study, we focused on adsorption and reactions pertinent to methoxide decomposition on the most stable regular (111) surface of PdZn alloy [50]. For monometallic Pd and Cu substrates, interactions of the same species with the most stable (111) crystal planes were also addressed for comparison. We will deal with adsorption complexes of C, H, O, CO, CH_3, CH_2O, and CH_3O on PdZn(111), Pd(111), and Cu(111) surfaces. These are the reactant and product species pertinent to the decomposition process of methoxide. Thereafter, we will study the C-H and C-O bond breaking of methoxide on the three substrates using the NEB method.

3.1 Models

For Pd(111) and Cu(111), we studied four adsorption sites: top, bridge, as well as fcc and hcp hollows. The sites studied on PdZn(111) surface are illustrated in Fig. 3.1. The combination sites top(Pd)-bridge-top(Zn), tbt^{PdZn} (11), and top(Pd)-bridge-top(Pd), tbt^{Pd2} (12), were only used for studying adsorption of formaldehyde.

3.2 Adsorption Complexes on (111) Surfaces of Pd, Cu and PdZn

Adsorbate-substrate interactions on alloy surfaces are often discussed in terms of an *ensemble* effect and a *ligand* or *electronic* effect [57]. The *ensemble* effect refers to spatial configuration of atoms that make up an adsorption site. The *ligand* effect denotes modifications of the adsorption properties of a given site due to (electronic) interaction with neighboring atoms around the site. Before comparing the calculated results for various adsorbates, we discuss ensemble and ligand effects on the alloy surface for adsorbed atomic oxygen as an example.

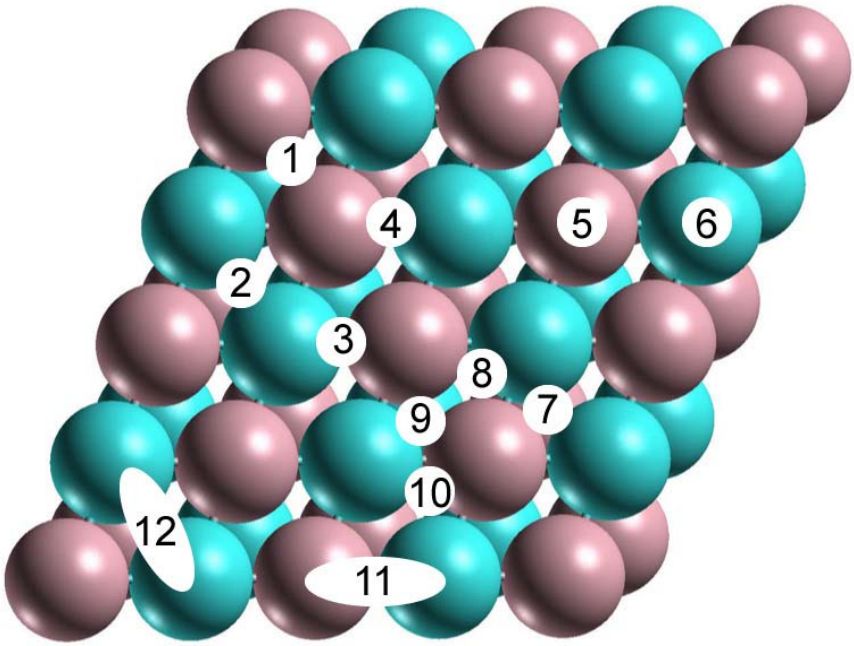

Figure 3.1. Adsorption sites on the PdZn(111) surface: B^{Zn2} (1), B^{Pd2} (2), $B_1{}^{PdZn}$ (3), $B_2{}^{PdZn}$ (4), T^{Zn} (5), T^{Pd} (6), H^{Pd2Zn} (7), F^{PdZn2} (8), H^{PdZn2} (9), F^{Pd2Zn} (10), tbt^{PdZn} (11), tbt^{Pd2} (12). Light red spheres – Zn, blue spheres – Pd.

Table 3.1 displays the geometric parameters and binding energies for an oxygen atom adsorbed at four different three-fold hollow sites of PdZn(111). The sites F^{PdZn2} and H^{PdZn2} feature the same configuration of nearest-neighbor metal atoms attached to the adsorbate: two Zn centers and one Pd center. Thus, the difference in the adsorption properties of the sites F^{PdZn2} and H^{PdZn2} is (by the above definition) due to the ligand effect. The calculated O-Zn distance for the F^{PdZn2} and H^{PdZn2} sites is almost the same, and the binding energies, ~440 kJ mol^{-1}, differ by only 13 kJ mol^{-1}. Pertinent adsorption characteristics of the sites H^{Pd2Zn} and F^{Pd2Zn} also are very similar: the interatomic distances O-Zn and O-Pd vary by merely 1 pm and the binding energies, ~390 kJ mol^{-1}, differ by 11 kJ mol^{-1}.

Differences between adsorption parameters of the sites F^{PdZn2} and F^{Pd2Zn} manifest an ensemble effect. The largest difference is calculated for the height of oxygen: 117 pm for F^{PdZn2}, and 11 pm longer for F^{Pd2Zn}. The corresponding alteration of the binding energy, 64 kJ mol^{-1}, is significantly larger than the ligand effect, 11–13 kJ mol^{-1}. A similar situation was found for the sites H^{PdZn2} and H^{Pd2Zn}: the difference in the heights of an O atom, 11 pm, is accompanied by an energy variation of 40 kJ mol^{-1}. The smaller oxygen heights of the sites F^{PdZn2} and H^{PdZn2} sites, compared to F^{Pd2Zn} and H^{Pd2Zn}, are consistent with stronger binding on the former two adsorption positions.

These findings show that the ligand effect on the adsorption energy, ~10 kJ mol^{-1}, is up to 6 times smaller than the corresponding ensemble effect. Calculated adsorption parameters of other adsorbates on PdZn(111) exhibit similar trends.

In this chapter, we restrict ourselves to the discussion of energetics of adsorption

Table 3.1. Calculated distances[a] (pm) for adsorption complexes of an O atom at three-fold hollow sites[b] of PdZn(111) and the corresponding binding (adsorption) energies BE (kJ mol^{-1}).

Observable	F^{PdZn2}	H^{PdZn2}	H^{Pd2Zn}	F^{Pd2Zn}
O-Zn	193	192	189	190
O-Pd	213	221	213	212
z(O)	117	118	129	128
BE	449	436	396	385

[a] O-Zn and O-Pd – bond lengths; z(O) – height of O above the "top" (111) plane of the substrate.

[b] For the definition of the adsorption sites, see text and Fig. 3.1.

complexes at top and three-fold hollow sites, which usually feature the smallest and largest binding energies, of the three substrates under investigation. The Cartesian coordinates and calculated total energies for all sites studied are collected in Appendix A. Table 3.2 summarizes the binding energy values calculated for various adsorbates at top and hollow sites of Pd(111), Cu(111) and PdZn(111) surfaces.

3.2.1 Atomic Carbon

The adsorption energy of atomic carbon on Pd(111) was estimated to be 669 kJ mol^{-1}, using a bond-order conservation (BOC) approach [58]. Recent cluster model DF calculations on the system C_8/Pd_{79} with eight adsorbed C atoms on fcc sites of Pd(111) facets (performed with the gradient-corrected exchange-correlation potential by Becke and Perdew, BP [59,60]) resulted in an adsorption energy of 664 kJ mol^{-1} per C atom [61]; on the larger nanocluster Pd_{140}, the adsorption energy was calculated only slightly smaller, 644 kJ mol^{-1} [62]. DF calculations with the exchange-correlation potential PW91 on three-layer slab models at 1/3

Table 3.2. Calculated binding energies BE (kJ mol^{-1}) for complexes of various adsorbates on three-fold hollow (fcc, hcp) and top (T) sites of Pd(111), Cu(111) and PdZn(111) surfaces.

Adsorbate	Pd			Cu			PdZn			
	fcc	hcp	top	fcc	hcp	top	H^{Pd} [a]	H^{Zn} [a]	T^{Pd}	T^{Zn}
C	634	642	406	474	466	282	448	416	316	190
H	274	268	224	237	237	183	249	225	214	146
O	420	399	255	465	455	294	396	449	238	274
CO	179	177	123	83	80	69	96 [b]	96 [c]	96	14
CH_3	152	142	170	144	142	127	134	145 [c]	145	102
CH_3O	162	153	90	236	235	167	194	221	112	161

[a] H^{Pd} denotes both F^{Pd2Zn} and H^{Pd2Zn} sites, H^{Zn} denotes both F^{PdZn2} and H^{PdZn2} sites; only the largest binding energy is shown. See text for details.

[b] Optimization of the CO position with initial adsorbate location at the site H^{Pd} resulted in a complex at the site B^{Pd2}; see Fig. 3.1 (2).

[c] Optimization of the CO and CH_3 positions with initial adsorbate location at the site H^{Zn} led to the corresponding structures at T^{Pd}.

coverage showed that fcc and hcp sites feature essentially the same adsorption energy of carbon, ~620 kJ mol^{-1}; C atoms on top sites are destabilized by about 230 kJ mol^{-1} with respect to hollow sites [63]. The binding energy values of C on Pd(111) as calculated in the present work (Table 3.2), 634 kJ mol^{-1} (fcc) and 642 kJ mol^{-1} (hcp), are ~15 kJ mol^{-1} larger than the value of ~620 kJ mol^{-1} reported earlier [63]. For the most part, this difference should probably be assigned to the different thickness of the slabs used in these two investigations (3 layers vs. 4-layer for our model) which employed the same exchange-correlation potential PW91. According to our calculations, the hcp site is insignificantly favored over the fcc position. The present binding energies of atomic C at three-fold hollow sites deviate only slightly from the cluster model values, 664 kJ mol^{-1} [61] and 644 kJ mol^{-1} [62], despite notable differences in these two computational technologies including different GGA energy functionals (BP, PW91). In line with previous results [61,63], carbon atoms tend to occupy highly-coordinated positions on a Pd surface. The large energy difference (> 230 kJ mol^{-1}) between top and hollow sites indicates that the potential energy surface (PES) of adsorbed carbon atoms on Pd(111) is significantly corrugated, implying that diffusion of adsorbed single carbon atoms is disfavored.

Our calculations of adsorbed carbon atoms on Cu(111) favor the fcc site very slightly (by 8 kJ mol^{-1}) over the hcp position (Table 3.2). The binding energies at fcc and hcp sites, 474 and 466 kJ mol^{-1}, are in good agreement with the value ~500 kJ mol^{-1} predicted by the BOC method [58]. At variance with the adsorption complexes C/Pd(111) [61], there is no cluster model study of the system C/Cu(111) where an attempt was made to eliminate the cluster size effect on the calculated adsorption energy. Hence, it is not surprising that the DF GGA cluster model values of the adsorption energy for carbon on hollow sites of Cu(111) surface scatter substantially, from 360 to 500 kJ mol^{-1} [64,65]. The difference of C binding energy on the top and hollow sites of Cu(111), ~190 kJ mol^{-1}, is about 40 kJ mol^{-1} smaller than on Pd(111), implying that the PES of adsorbed atom C on Cu(111) is slightly less corrugated than on Pd(111).

The most stable site of adsorbed carbon atom on PdZn(111), H^{Pd}, features a binding energy of 448 kJ mol^{-1} (Table 3.2.), which is 32 kJ mol^{-1} larger than on the H^{Zn} site. Key to rationalizing this result is the binding energies of C at the two top sites: the one at T^{Zn}, 190 kJ mol^{-1}, is 126 kJ mol^{-1} smaller than that at T^{Pd}. Thus, the bonding interaction of C with Pd centers in the alloy is notably stronger than with Zn atoms and a C atom should be stabilized most on sites with as many Pd atoms as possible. The binding energy at the site H^{Pd} of

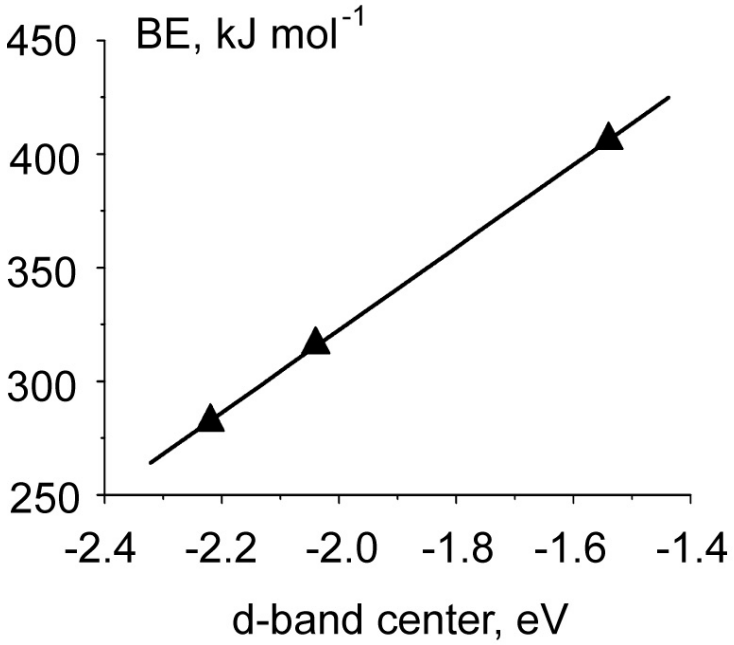

Figure 3.2. Correlation of the binding energy, BE, of a carbon atom adsorbed at top sites of Pd(111) and Cu(111) or at site T^{Pd} of PdZn(111) with the center of the valence d-band (local partial DOS) of Pd and Cu atoms of the outermost surface layer of the slab models.

PdZn(111), 448 kJ mol^{-1}, is ~190 kJ mol^{-1} smaller than on three-fold hollow sites of Pd(111), but close to that on Cu(111), ~470 kJ mol^{-1}. Thus, the strength of the interaction of C with PdZn is similar to that with Cu. One can try to rationalize trends in adsorption energies on metals based on the d-band center model [66], according to which a lower energy of the d-band center (center of local partial density of states, DOS, with respect to Fermi level) corresponds to weaker bonding with adsorbates. The valence d-band centers of Cu, -2.22 eV, and of the Pd local density of states (DOS) of PdZn alloy, -2.04 eV, are lower than the d-band center of Pd metal, -1.54 [50]. This correlates with the finding that the binding energies of adsorbed carbon atoms are smaller on PdZn(111) and Cu(111) surfaces than on Pd(111). The calculated energies of the d-band centers of clean (111) surfaces of these three substrates [50] and the binding energies of a carbon atom at the corresponding top sites correlate linearly (Fig. 3.2), in agreement with the d-band center approach.

3.2.2 Atomic Hydrogen

Low-energy electron diffraction (LEED) showed that on a Pd(111) surface H atoms reside at fcc three-fold hollow sites [67]. Many theoretical studies on Pd surfaces corroborated that H

atoms prefer high-coordination hollow sites, but there is no agreement concerning the most favorable site [61,68]. We found essentially the same adsorption energy of H, ~270 kJ mol^{-1}, on fcc and hcp sites of Pd(111); this value is somewhat lower than the GGA (BP) result of the cluster model H_8/Pd_{79}, 311 kJ mol^{-1} [61], but close to the experimental value, 259 kJ mol^{-1}; see Ref. 58. On the least favorable site, on-top, H adsorption is only ~50 kJ mol^{-1} less stable (Table 2). Such a small range of energy values indicates a rather flat PES of H on Pd(111), implying significant mobility of adsorbed H.

It is known that H adsorbates on Pd show a propensity to diffuse to subsurface position at increased coverage [69] and recent experiments indicate that the H surface to subsurface diffusion is easier on the more open Pd surfaces compared to Pd(111) [70], yet at low coverage, atomic species in subsurface positions appear to be thermodynamically disfavored compared to the adsorption at the surface [61]. Our calculations of subsurface hydrogen at octahedral sites (hole below the fcc site) finds that the binding energy at the octahedral hole is 52 kJ mol^{-1} less favorable than the fcc site [71]. Using single point calculations at different height from the surface and a fitting curve (see Fig. 3.3) estimates the diffusion barrier of atomic hydrogen from fcc to octahedral sites to be ~79 kJ mol^{-1} [71], in agreement with the

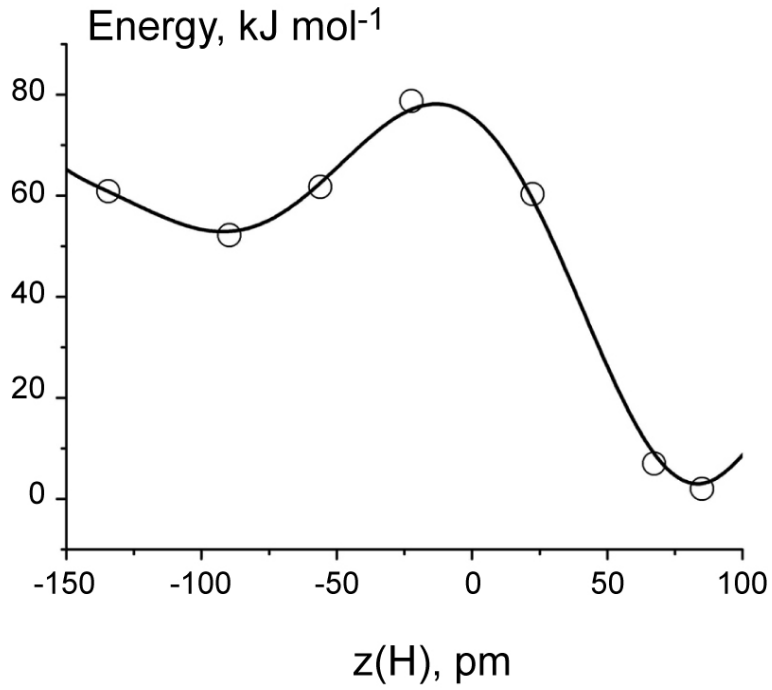

Figure 3.3. Potential energy profile of atomic H vs. height of hydrogen from surface, z(H) along the surface normal centered at the fcc sites. Local minimum corresponds to H in octahedral subsurfaces (left) and at fcc sites (right).

reported values for cluster method calculated with the BP functional, i.e. reaction energy = 50 kJ mol^{-1}, activation energy = 60 kJ mol^{-1} [61]. The more favorable energetics observed in the (moderately large) cluster model, Pd_{79} may likely be due to less steric interaction compared to the slab model where coverage of 1/4 is used.

Previous slab model DF calculations of adsorbed H atom on Cu(111) resulted in equal occupancy at fcc and hcp sites, with a binding energy of 229 kJ mol^{-1} [72]. This situation is reproduced in our calculations (Table 3.2): both fcc and hcp sites are characterized by binding energy of 237 kJ mol^{-1}, in good agreement with the experimental result 234 kJ mol^{-1} [58]. The binding energy difference of hydrogen at the on-top and hollow sites of Cu(111) is slightly larger, 54 kJ mol^{-1}, than for H/Pd(111), again indicative for the significant mobility of the adsorbate.

The most favorable site of single H atom on PdZn(111) is H^{Pd} with an adsorption energy of 249 kJ mol^{-1}. The energies at top sites, 214 kJ mol^{-1} (T^{Pd}) and 146 kJ mol^{-1} (T^{Zn}), manifest that H interacts more strongly with Pd than with Zn, consistent with the stronger binding at H^{Pd} than at H^{Zn}. The range of binding energy values of hydrogen adsorbed on PdZn(111) alloy, ~100 kJ mol^{-1}, is about twice as large as for the monometallic substrates Pd(111) and Cu(111); hence, the PES of adsorbed H is expected to be more corrugated on the alloy. The energies of the valence d-band centers of Cu metal and of the Pd local DOS of PdZn alloy is lower than that of Pd metal. This is in line with the finding that the binding energies of hydrogen atom at a T^{Pd} site of PdZn(111) and the top site of Cu(111), 214 and 183 kJ mol^{-1}, respectively, are smaller than for the on-top position of Pd(111), 224 kJ mol^{-1}.

3.2.3 Atomic Oxygen

Low-energy ion scattering measurements indicated that at a coverage of 1/4, O atoms are adsorbed at hcp sites of the Pd(111) surface [73], whereas a recent LEED study concluded that oxygen atoms prefer fcc sites [74], in agreement with DF calculations [75,76]. Our calculations (Table 3.2) also support the latter viewpoint: the complex of O with the hcp site of Pd(111) is 21 kJ mol^{-1} less stable than that at the fcc position, 420 kJ mol^{-1}. The latter value agrees with the BP GGA adsorption energy of an O atom at fcc sites of the cluster Pd_{79}, 419 kJ mol^{-1} [61]. The present binding energy at the top site is ~150 kJ mol^{-1} lower than at the

hollow sites. This difference is ~80 kJ mol^{-1} smaller than for C/Pd(111), showing that on Pd(111), the PES of absorbed O atoms is flatter than that of the stronger interacting atoms C.

On a Cu(111) surface, three-fold hollow sites are experimentally found to be preferred by atomic O [77,78]. Our calculated binding energies favor fcc over hcp sites, in line with recent slab model DF-GGA results [79]; the difference, however, is minor. The binding energy at the on-top site is 160–170 kJ mol^{-1} smaller than on the hollow sites (Table 3.2). One also finds that O atoms bind to all studied sites on Cu(111) 40–55 kJ mol^{-1} more strongly than to the corresponding sites of Pd(111). This is at variance with the d-band center model [66], probably because of notable bonding contributions from s and p bands of Cu to the O-Cu interaction.

On the alloy surface PdZn(111), we calculated atomic O to prefer hollow sites H^{Zn} with a binding energy of 449 kJ mol^{-1}; this is notably (more than 10 %) larger than that at H^{Pd} sites. Oxygen interacts with Zn atoms of PdZn(111) more strongly than with Pd atoms as reflected by the binding energy on T^{Zn} sites, 274 kJ mol^{-1}, which is 36 kJ mol^{-1} larger than at T^{Pd}. Therefore, O atoms on a PdZn(111) substrate prefer hollow sites with more Zn atoms, at variance with C and H atoms (see above). According to the d-band center model [66], one expects a smaller binding energy for oxygen atoms at Pd atoms of PdZn(111), compared to Pd atoms of Pd(111) [50]. This is true for top sites where only the electronic effect plays a role. On the other hand, the binding energy at the site H^{Zn}, 449 kJ mol^{-1}, is larger than for O adsorbate at the fcc site of Pd(111) surface (Table 3.2). One can rationalize this trend as an ensemble effect by recalling that O-Zn bonding is stronger than O-Pd bonding: at H^{Zn} sites of PdZn(111), O binds to one Pd and two Zn centers, whereas on fcc sites of Pd(111) the adsorbate binds to three Pd centers.

3.2.4 Carbon Monoxide

CO is often used as probe molecule in surface science and catalysis. Many studies have been performed on CO adsorption over metal surfaces, for example Ref. 80. In our previous analysis of the electronic structure of PdZn alloy and monometallic Pd and Cu substrates, we concluded that the binding energy of CO over PdZn is reduced compared to that on Pd(111) and is close to the value on Cu [50]. Recent scalar relativistic DF calculations of CO interactions with nanosize cluster models $Pd_{140-n}Zn_n$, where cluster size effects were

essentially eliminated, corroborated the above binding energy relations for Pd(111) and PdZn(111) substrates [81].

Here we present slab model data computed for CO adsorption on the (111) surface of Pd, Cu and PdZn single-crystal substrates. It is widely accepted that adsorption of CO on metal surfaces takes place via the so-called Blyholder mechanism [82]: donation of electron density from the 5σ orbital of CO molecule to the metal and back-donation from the substrate into the 2π* orbital of CO. A detailed experimental and theoretical analysis actually allows one to discriminate three-orbital interactions in both σ and π channels [83].

STM measurements indicate that CO adsorbed on Pd(111) occupies hollow sites [84]. DF slab model results provided evidence that fcc and hcp sites exhibit basically the same adsorption propensity for CO, with essentially equal binding energies of 194 kJ mol^{-1} (fcc) and 191 kJ mol^{-1} (hcp) at 1/3 coverage [85]. Our calculated binding energies, 179 kJ mol^{-1} (fcc) and 177 kJ mol^{-1} (hcp), also support this conclusion. The binding energy on-top of Pd atoms is calculated almost 60 kJ mol^{-1} smaller than at hollow sites; this result is comparable to the binding energy difference calculated for H adsorbed at hollow and top sites of Pd(111) (Table 3.2).

The CO molecule interacts with a Cu(111) surface significantly less strongly. PW91 slab model calculations showed that CO favors the hollow sites of Cu(111), with fcc and hcp sites again being essentially isoenergetic, 87 kJ mol^{-1} [86]. We found a similar situation (Table 3.2). The very small energy difference, ~10 kJ mol^{-1}, between top and hollow sites of adsorbed CO on Cu(111) is a clear manifestation of the very flat nature of the corresponding PES, and thus high CO mobility predicted.

On the (111) surface of PdZn alloy CO interacts much more weakly with Zn atoms at top sites T^{Zn} (BE = 14 kJ mol^{-1}) than with T^{Pd} sites (BE = 96 kJ mol^{-1}; Table 3.2). Consequently, during the geometry optimization starting with CO at F^{PdZn2} and H^{PdZn2} sites, the adsorbate drifted to T^{Pd} sites; similarly, starting from F^{Pd2Zn} and H^{Pd2Zn} sites, CO moved to the bridge site B^{Pd2} (Fig. 3.1). CO complexes at T^{Pd} and B^{Pd2} featured essentially equal binding energies, 96 kJ mol^{-1}, half of the binding energies on hollow sites of Pd(111), 177–179 kJ mol^{-1}, and close to the adsorption energy on Cu(111) (Table 3.2). These results agree with the experimental observation that CO binds weaker on PdZn alloy than on metallic Pd [87], and they corroborate the d-band model prediction [50].

We calculated the harmonic vibrational frequency of a free CO molecule at 2135 cm^{-1}. Upon adsorption, this vibrational band shifts to the red. The calculated frequencies, 2026 cm^{-1} at T^{Pd} and 1872 cm^{-1} at B^{Pd2}, fit the experimental values of 2040 cm^{-1} and 1902 cm^{-1}, respectively [88]. Because O atoms bind strongly with Zn centers, we also tried an O-bonded adsorption mode of CO at the site T^{Zn}, but during the optimization the CO bond axis rotated and finally led to the conventional bonding configuration with the C atom directed to the surface. We also examined CO "lying-down", with the molecular axis parallel to the substrate surface and with the O center close to Zn and C close to Pd atoms; however, we were not able to locate a stable structure. All these attempts demonstrate that CO binds to a PdZn(111) surface with the same bonding mode as on a pure (transition) metal surface, i.e. via its C atom.

3.2.5 Methyl

On a Pd(111) surface, GGA-PW91 slab model calculations favor on-top adsorption for methyl radicals, whereas at the LDA level (VWN functional [89]) hollow sites were slightly preferred [63]. Our calculations of adsorption complexes CH_3/Pd(111) yielded binding energies at hollow sites of 152 kJ mol^{-1} (fcc) and 142 kJ mol^{-1} (hcp); on-top sites were characterized by a somewhat stronger adsorption bond, 170 kJ mol^{-1} (Table 3.2). This propensity of methyl adsorbates on Pd(111) to occupy on-top sites is in contrast to adsorbed C, H and O species, which favor hollow sites with their higher coordination. The flat PES of CH_3/Pd(111) implies easy diffusion of adsorbed methyl groups on the Pd(111) substrate. In the most stable on-top configuration, CH_3 moieties freely rotate around the C_3 symmetry axis essentially without a barrier (1 kJ mol^{-1}). At the hollow sites, the computed rotational barrier of CH_3 groups around the C_3 axis is 14 kJ mol^{-1}, implying only a moderate hindrance.

Photoelectron diffraction (PED) results for CH_3/Cu(111) at 1/3 coverage revealed that methyl groups occupy fcc sites on Cu(111) [90]. RPBE GGA [91] slab model calculations [92] showed that the bonding of the adsorption complexes with hcp and fcc sites are characterized by essentially the same energy, ~185 kJ mol^{-1}, with the hcp configuration favored by 3 kJ mol^{-1} only. A three-layer slab model at a coverage of 1/6 furnished a GGA-PW91 binding energy of 151 kJ mol^{-1} for both fcc and hcp sites [93]. Our calculations also showed that hollow sites CH_3/Cu(111) complexes feature almost equal stability, 144 kJ mol^{-1} (fcc) and 142 kJ mol^{-1} (hcp).

At variance with Pd(111), on a Cu(111) surface CH_3 adsorbate favors hollow sites. The different site preference on Pd(111) and Cu(111) can be attributed to a weaker bonding interaction of Cu 3d orbitals with CH_3 compared to Pd 4d orbitals. The electronic structure of a CH_3 adsorption complex can be interpreted in a way that the adsorbate achieves a closed-shell electron configuration, similar to that of the anion CH_3^-, after having accepted an electron from the substrate. The 2σ molecular orbital of CH_3 has been shown [94] to dominate the bonding interaction with a transition metal substrate (M); according to that analysis, 2σ-d(M) bonding results in the preference of on-top sites, whereas 2σ-s(M) favors hollow positions. Thus, the 2σ-4d(Pd) interaction is important for CH_3 on Pd(111), whereas 2σ-4s(Cu) bonding prevails on Cu(111). The latter finding is due to more compact nature of Cu 3d orbitals.

Methyl groups interact with the substrate via the carbon atom. As atomic C interacts stronger with Pd than with Zn centers (Section 3.2.1), it is plausible that the calculations favor CH_3 adsorption at T^{Pd} sites of PdZn(111) (Table 3.2). At this most favorable site of PdZn(111), the calculated binding energy was 25 kJ mol^{-1} smaller than at the on-top site of Pd(111), in line with the d-band center model [50]. Complexes with H^{Pd} sites were found to be 11 kJ mol^{-1} less stable than with T^{Pd} sites. In a structure optimization starting with CH_3 at the H^{Zn} position, the methyl group moved to the site T^{Pd}. Adsorption weakens the C-H bonds, which is reflected by the red-shift of the C-H stretching frequency; in the free CH_3 radical, that frequency is calculated at 3087 cm^{-1} whereas it decreases to 3007 cm^{-1} for adsorbed CH_3 on T^{Pd} of PdZn(111).

3.2.6 Formaldehyde

CH_2O molecules adsorb on transition metal surfaces in two bonding modes, η^1-(O) and η^2-(C,O) or top-bridge-top mode (tbt structure) [95]. In the η^1-(O) configuration, the molecule binds to the surface via the O atom using one of its lone pairs. In the η^2-(C,O) mode, the adsorbate interacts with the substrate via both C and O atoms. On clean surfaces of group VIII metals, the η^2-(C,O) mode is preferred in general, although both adsorption configurations have been detected experimentally [95]. Our calculated results of CH_2O species adsorbed on Pd(111) are consistent with these findings. All η^1-(O) configurations of adsorption complexes we inspected exhibited negative binding energy, i.e. this type of structures is unstable. In the

η^2-(C,O) structure, with a positive binding energy, the molecular plane of CH_2O is almost parallel to the substrate surface. In cluster calculations using small Pd_8 and Pd_{19} models of Pd(111), the η^2-(C,O) structure was favored [96,97]. Slab model DF investigations exclusively reported η^2-(C,O) structures as most stable [98,99]. Our calculated binding energy of CH_2O/Pd(111) complexes, 43 kJ mol^{-1}, is close to the value of 50 kJ mol^{-1} determined from temperature-programmed-desorption (TPD) data [100] as well as to results of other slab model calculations, 54–61 kJ mol^{-1} [98,99]. These small binding energy values manifest rather weak interactions of CH_2O with a Pd(111) surface.

Unlike on group VIII metals, formaldehyde is thought to adsorb on Cu surfaces in η^1-(O) mode [95]. The different decomposition behavior of formaldehyde on group IB and VIII metal surfaces has been attributed to different bonding modes [5]. To find out whether formaldehyde prefers an η^1-(O) structure on Cu(111), we tried to optimize this structure, but failed to find a stable configuration. Instead, we calculated CH_2O species to exhibit a tbt structure on a Cu(111) surface as well. The binding energy of only 11 kJ mol^{-1} implies a negligible interaction between CH_2O and Cu(111) substrate. Note that such a weak binding has to be considered outside the range where DF-GGA energy functionals are reliable; this is mainly due to the fact that contemporary exchange-correlation potentials do not account for dispersive interactions [34].

On a PdZn(111) surface, we identified two η^2-structures. In the less stable tbt^{Pd2} complex (see Fig. 3.1), C and O atoms bind to two adjacent Pd atoms, with C-Pd and O-Pd distances of 246 pm and 237 pm, respectively (see Appendix A). These distances are longer than the corresponding values on a Pd(111) surface, indicating that the adsorbate-substrate interaction is weaker on PdZn(111). Indeed, the calculated binding energy for the tbt^{Pd2} configuration is only 10 kJ mol^{-1}. The second η^2-structure is of type tbt^{PdZn} (see Fig. 3.1), in which the C atom binds to a Pd atom while the O atom binds to an adjacent Zn atom. The binding energy is calculated at 23 kJ mol^{-1}, slightly larger than for the tbt^{Pd2} site. The C-Pd distance, 225 pm, is shorter than in the tbt^{Pd2} structure (246 pm). The O atom actually resides on a position slightly displaced from the perfect bridge site between Zn and Pd atoms. As just pointed out, predictions of DF calculations for all complexes CH_2O/PdZn(111) have to be interpreted with care: probably the only reliable conclusion is that the adsorption interaction is very weak. Thus, in most of these energy estimates, adsorbed CH_2O species can be considered as essentially free molecules.

3.2.7 Methoxide

CH_3O is an intermediate of methanol dehydrogenation. Cluster [96,97] and slab model calculations [99] showed that hollow sites are favored on Pd(111). We calculated the binding energy of CH_3O at hollow sites of Pd(111) at 162 kJ mol^{-1} (fcc) and 153 kJ mol^{-1} (hcp); these values are 60–70 kJ mol^{-1} larger than for on-top adsorption complexes (Table 3.2). The distance between the H of the methoxide moiety and the substrate Pd atoms is longer than in the case of CH_3/Pd(111) and the interaction of H atoms with the substrate is very weak. This can also be seen from the negligible rotational barrier around the C_3 axis of CH_3O at the fcc site, 2 kJ mol^{-1}, as compared to 14 kJ mol^{-1} for CH_3 on Pd(111).

The structure of the adsorption complex CH_3O/Cu(111) has been investigated experimentally by several groups [101]. It is generally accepted that one type of three-fold hollow sites is preferred by CH_3O and the C-O bond is oriented perpendicular to the surface. Although PED investigations established fcc sites as most favorable [102], a very recent study using normal incidence X-ray standing wavefield absorption revealed that CH_3O populates both fcc and hcp sites [103]. Binding energies of 241 kJ mol^{-1} (fcc) and 211 kJ mol^{-1} (hcp) were computed for this system at the B3LYP level, modeled by a Cu_7 cluster [104]; unfortunately, these data showed a very strong cluster size effect when compared to the value of 161 kJ mol^{-1} (fcc) which has been reported earlier by the same group for somewhat larger substrate models [105]. Configuration interaction (CI) calculations for a Cu_7 cluster model predicted 272 kJ mol^{-1} for fcc and 234 kJ mol^{-1} for hcp adsorption sites [106]. Our calculations show essentially equal binding energies 236 kJ mol^{-1} (fcc) and 235 kJ mol^{-1} (hcp), supporting the experimental finding that CH_3O populates both types of three-fold sites [103]. At the on-top site, the binding energy was calculated about 70 kJ mol^{-1} smaller; this corrugation of PES for Cu(111) is similar to that of Pd(111) (60-70 kJ mol^{-1}), indicating a comparable propensity for diffusion of CH_3O on Cu(111) and Pd(111).

On the (111) surface of PdZn alloy, we calculated the H^{Zn} site to be most favorable for CH_3O adsorption, 27 kJ mol^{-1} larger than for the H^{Pd} site. This result is not unexpected if we recall that oxygen tends to prefer sites with as many Zn atoms as possible and that the CH_3O moiety binds to the substrate via its O atom. Similar to atomic O species, the binding energy of CH_3O adsorbate at T^{Zn}, is 49 kJ mol^{-1} larger than at T^{Pd}. The computed C-O stretching frequency of the free CH_3O radical at 1114 cm^{-1}; decreases to 1003 cm^{-1} upon adsorption. This significant frequency red-shift can be used as an experimental indicator for the presence

of adsorbed CH_3O under reaction conditions of methanol decomposition. Among the three substrates addressed in this work, the binding energy of adsorbed CH_3O on Pd(111) is the smallest one, which results in a lower energy barrier for C-H and C-O bond breaking of CH_3O adsorbed on Pd(111) than on Cu(111) and PdZn(111); see Section 3.3.

For the (111) surfaces of the substrates Pd, Cu, and PdZn, we have discussed the energetics of various adsorbates pertinent to methanol decomposition. The general trends of the binding energy due to alloying can be summarized as follows (Table 3.2). The binding energies for O bound species (O and CH_3O) are larger on PdZn(111) than on Pd(111), whereas the strength of adsorption interactions of H and C bound species (C, CO and CH_3) is smaller on PdZn(111) than on Pd(111). The binding energies of all these adsorbates on PdZn(111) are close to the corresponding values on Cu(111), implying that the surface reactivities of PdZn(111) and Cu(111) substrates are similar [50].

3.3 Decomposition of Methoxide on (111) Surfaces of Pd, Cu and PdZn

The most stable adsorption structures of CH_3O on the three substrates were chosen as IS for both C-O and C-H bond breaking. Figs. 3.4 display the IS on Pd(111), Cu(111) and PdZn(111).

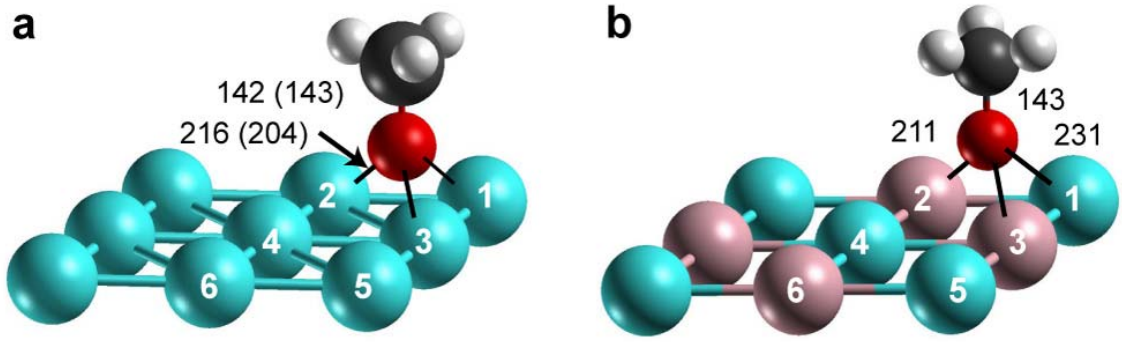

Figure 3.4. Sketches of initial state (IS) of CH_3O decomposition with selected bond distances shown (pm): a) on Pd(111) and Cu(111) (Cu values in parentheses); and b) on PdZn(111). Labeling of atomic spheres: light red – Cu or Zn, blue – Pd, dark red – O, black – C, gray - H.

3.3.1 C-O Bond Cleavage

In the IS of CH_3O decomposition, on Pd(111), the O atom binds symmetrically to three adjacent Pd atoms at a distance of 216 pm and the C-O bond (142 pm) is perpendicular to the (111) surface (see Fig. 3.4a). In the final state (FS) on Pd(111), CH_3(s) + O(s), the methyl group resides on top of atom Pd(4) (see Fig. 3.4a for the labeling of Pd atoms) and the atom O remains at the fcc site {123} made up of the Pd centers 1 - 3.

C-O bond breaking on Pd(111) is calculated to proceed as follows: At the beginning of the reaction, the oxygen atom moves toward the bridge site Pd(2)-Pd(3), accompanied by an elongation of the O-Pd(1) distance, and the C-O bond tilts. Simultaneously, the methyl group is displaced to the Pd(3)-Pd(4) bridge. With decreasing C-Pd(3) and C-Pd(4) distances, the interaction between CH_3 and the two Pd atoms is enhanced. This, in turn, weakens the C-O bond, as shown by an elongation from 142 pm in the IS to 201 pm in the TS (Table 3.3). As soon as the TS is reached, the atom O retreats to the favorable fcc site. In the TS, the methyl group is located close to the bridge site Pd(3)-Pd(4), significantly tilted (63°) with respect to

Table 3.3. Structural characteristics[a] (distances in pm) of transition states of C-O bond breaking of CH_3O on the (111) surfaces of the substrates Pd, Cu, and PdZn, as well as the corresponding activation energies E_a (kJ mol^{-1}).

Observable	C-O bond breaking		
	Pd	Cu	PdZn
C-M(3/1)[b]	247	268	486
C-M(4)	320	274	242
O-M(1)	208	204	280
O-M(2)	203	188	197
O-M(3)	207	191	197
O-M(4)	344	326	238
C-H	109	110	109
C-O	201	199	207
z(C)	238	238	241
z(O)	128	125	129
E_a	146	203	208

[a] A-B – distance between atoms A and B; z(A) – height of atom A above the "top" (111) surface plane.

[b] M(i/j) denotes atom i on Pd(111) and Cu(111) and atom j on PdZn(111); for the numbering of substrate centers, see Fig. 3.4.

the surface normal. The shortest H-Pd distance is 247 pm, compared to 335 pm in the IS. The distance C-Pd(3), 247 pm, is notably (73 pm) shorter than C-Pd(4), 320 pm, manifesting stronger bonding interaction between CH_3 and atom Pd(3). The latter center is shared by the adsorbate moieties O and CH_3. Therefore, bonding competition apparently exists [107] which pushes the methyl fragment to atom Pd(4). In the FS, the CH_3 group is situated almost on-top of Pd(4) and the O atom, at the fcc site forms three equal O-Pd bond distances of 201 pm.

The C-O scission of methoxide on Cu(111) proceeds similarly to that on Pd(111) and the shape of the TS structure resembles that on Pd(111) (Table 3.3). Recall that CH_3 favors a three-fold hollow site on Cu(111) at variance with the top site on Pd(111) (Table 3.2); thus, the dissociated methyl group moves from the bridge site in the TS to the fcc site {345} in the FS.

On PdZn(111), C-O bond breaking of CH_3O begins with an inclination of the C-O axis towards atom Pd(4). In the TS (Table 3.3, Fig. 3.5), the C-Pd(4) distance has shrunk to 242 pm, from 404 pm in the IS. The position of the CH_3 group on PdZn(111), on top of a Pd center, is different from that on Pd(111) and Cu(111), where CH_3 is located on a bridge site. In the TS, the axis of the methyl group is tilted with respect to the substrate normal. In the IS on PdZn(111), the distance O-Pd(4) is 75 pm longer than O-Pd(1), whereas in the TS, their relation is opposite: O-Pd(4) is 42 pm shorter than O-Pd(1). This shows that the atom O moves from site F^{PdZn2} in the IS to site H^{PdZn2} in the TS. The O atom moves from site H^{PdZn2} {234} in the TS to site F^{PdZn2} {123} in the FS, binding to the centers Pd(1), Zn(2) and Zn(3)

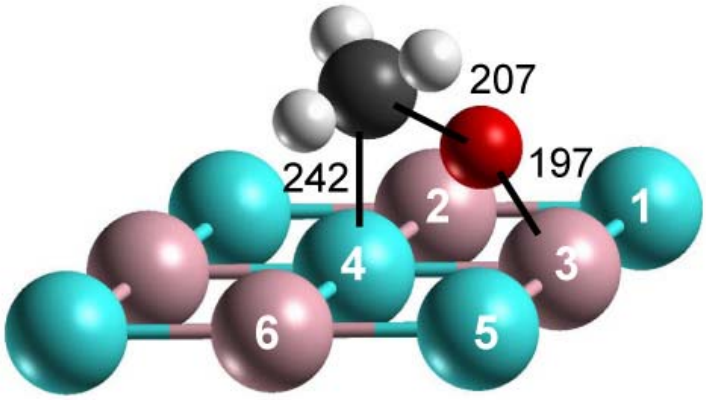

Figure 3.5. Sketches of C-O bond breaking transition state of CH_3O with selected bond distances shown (pm) on PdZn(111). Labeling of atomic spheres: light red – Cu or Zn, blue – Pd, dark red – O, black – C, gray - H.

Table 3.4. Calculated reaction energies[a] (kJ mol^{-1}) for the initial steps of the decomposition of gas-phase (g) methanol on the (111) surfaces (s) of Pd, Cu, and PdZn.

Reaction step	Pd(111)	Cu(111)	PdZn(111)
1 $CH_3OH(g) \rightarrow CH_3O(s) + H(s)$	21	-15	-12
2 $CH_3O(s) \rightarrow CH_2O(s) + H(s)$	-45	97	61
3 $CH_3O(s) \rightarrow CH_3(s) + O(s)$	5	60	60

[a] A reaction energy E_r is calculated as $E_r = \Sigma(E_T)^P - \Sigma(E_T)^R - \Sigma(BE)^P + \Sigma(BE)^R$, where $\Sigma(E_T)^P$ and $\Sigma(E_T)^R$ are sums of total energies for products and reactants in the gas phase, respectively. $\Sigma(BE)^P$ and $\Sigma(BE)^R$ are sums of calculated binding energies for isolated product and reactant species, respectively. A negative value of E_r corresponds to an exothermic process.

with O-Pd(1) = 210 pm and O-Zn = 193 pm. As on Pd(111), the methyl group occupies a position on top of a Pd center, namely Pd(4), with C-Pd(4) = 212 pm.

Finally, we comment on the energies characterizing C-O bond breaking of CH_3O moieties adsorbed on the different substrates (Tables 3.3 and 3.4). On Pd(111), the activation barrier was calculated at 146 kJ mol^{-1}, whereas the barriers on Cu(111) and PdZn(111) are 203 and 208 kJ mol^{-1}, respectively (Table 3.3, Fig. 3.6). Clearly, C-O bond breaking is easier on Pd than on Cu and on the alloy surface, although all barriers are too high to ensure facile bond breaking. The latter two energy barriers are higher due to the stronger binding of CH_3O on Cu(111) and PdZn(111) than on Pd(111). The binding energies of CH_3O (Table 3.2) and the corresponding activation energies (Table 3.3) on the three substrates reveals that the profiles of the barriers are similar (Fig. 3.6): the differences of energy barriers are close to the differences of the binding energies of the corresponding IS complexes; e.g. $BE(CH_3O/PdZn) - BE(CH_3O/Pd) = 59$ kJ mol^{-1} and the corresponding barrier difference $\Delta E_a = 62$ kJ mol^{-1}.

3.3.2 C-H Bond Breaking

The IS of C-H bond breaking of CH_3O on Pd(111) is the same as that for C-O bond cleavage (see Section 3.3.1). In the FS, the product CH_2O forms a tbt structure over the atoms Pd(2) and Pd(3); the H_a atom, released during dehydrogenation, is at the fcc site {345} (see Figs. 3.4a, 3.7a for numbering of atoms). Hydrogen abstraction from CH_3O on Pd(111) starts with tilting of the C-O bond, accompanied by an upward movement of the atom O to the top site

on Pd(2). In the course of the reaction, the H_a-Pd(3) distance decreases, manifesting a bonding interaction of these two atoms. In the TS (Fig. 3.7a), the activated C-H_a bond is elongated by 29 pm and the C-O distance becomes 9 pm shorter than in the IS. The C-O axis of the TS complex is oriented almost parallel to the Pd(111) surface.

In the TS of C-H bond cleavage on Cu(111), similarly to the TS on Pd(111) (cf. Figs. 3.7a, b), the C-O bond (131 pm) is tilted with respect to the surface, by ~14°. In the FS, the H_a atom sits on the hollow site {345}, with H_a-Cu = 174 pm and z(H_a) = 91 pm. The CH_2O(s) product species resides at the top-bridge-top site over the Cu(2) and Cu(3) atoms.

Like C-H bond scission on Pd(111), on PdZn(111) it also begins with an inclination of the CH_3O group towards atom Pd(4) (Figs. 3.7c, d); simultaneously, the O atom moves toward the position on-top of Zn(3). With the tilting of the C-O bond, the H_a-Pd(4) distance shrinks, indicating a bonding interaction between these atoms. In the TS on PdZn(111) (Table 3.5, Figs. 3.7c, d), the C-H_a distance is stretched to 170 pm. With 130 pm, the C-O distance of the

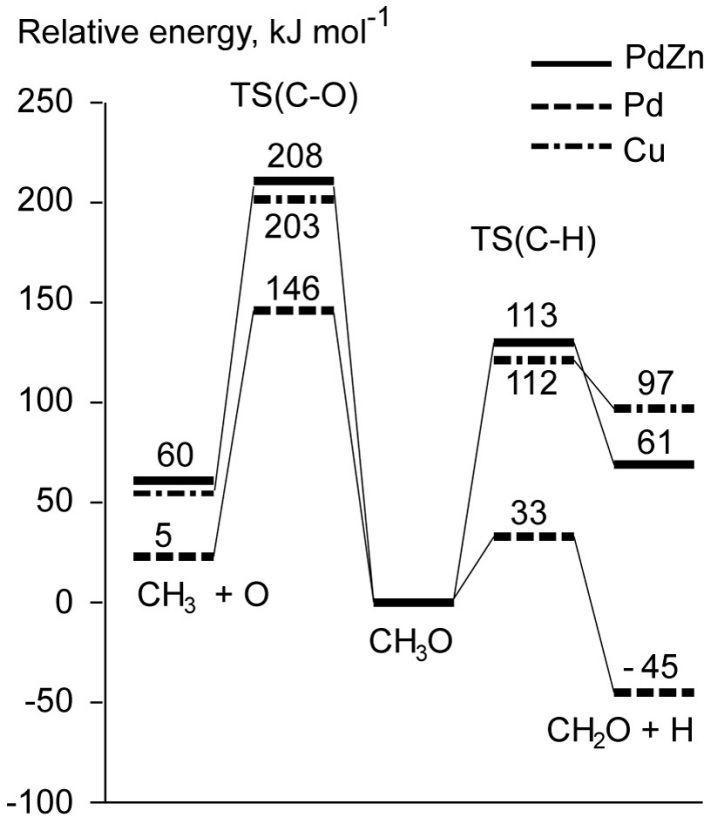

Figure 3.6. Calculated activation and reaction energies (kJ mol^{-1}) characterizing C-O and C-H bond breaking of CH_3O on PdZn(111), Pd(111) and Cu(111) substrates with respect to the energy calculated for the corresponding CH_3O adsorption complex.

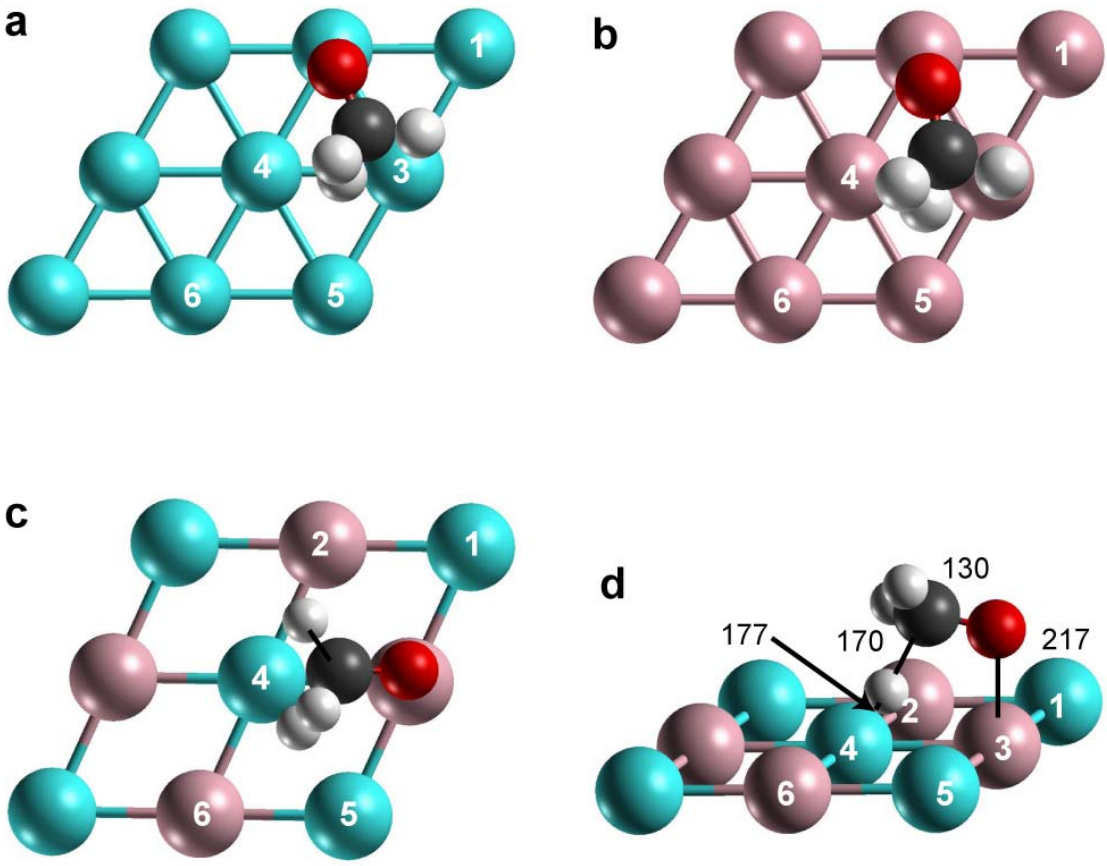

Figure 3.7. Sketches of C-H bond breaking TS structures of CH_3O with selected bond distances shown (pm): a) top view on Pd(111); b) top view on Cu(111); c) top view on PdZn(111); and d) side view on PdZn(111). Labeling of atomic spheres: light red – Cu or Zn, blue – Pd, dark red – O, black – C, gray - H.

TS becomes equal to that of adsorbed CH_2O at the tbt^{PdZn} site. Due to bonding competition at Pd(4), H_a moves towards the bridge Pd(5)-Zn(6). In the FS, H_a atom is located at the hollow site {456}. The C-O bond, 125 pm, is oriented almost parallel to the PdZn(111) surface, the height z(C) = 243 pm is 18 pm larger than z(O).

It is instructive to compare the topological characteristics of the transition states on the three substrates under investigation (Figs. 3.7 a, b, c). The C-O bond axis of the TS on Pd(111) is approximately parallel to Pd(2)-Pd(3) (Fig. 3.7a). The O-Pd(1) distance, 339 pm, is close to O-Pd(4), 322 pm; the difference between C-Pd(1) and C-Pd(4) is 41 pm. These data show that the C-O moiety of CH_2O is approximately oriented in a reflection plane along Pd(2) and Pd(3), perpendicular to the (111) surface. In the TS on Cu(111), the C-O moiety does not lie in the corresponding pseudoreflection plane through Cu(2) and Cu(3); rather, the adsorbate is tilted toward Cu(5) (Fig. 3.7b). The distances O-Cu(3) and O-Cu(4) are almost equal, 296

and 298 pm, respectively; the distances C-Cu(3) = 264 pm and C-Cu(4) = 289 pm are comparable. Thus, while the pseudoreflection plane on Pd(111) is along the short bridge Pd(2)-Pd(3), it is along the long bridge Cu(2)-Cu(5) on Cu(111). This difference can be rationalized by the adsorption behavior of the CH_3 group; recall that the methyl group favors a top site on Pd(111) whereas the hollow site is preferred on Cu(111) (Section 3.2.5). In fact, in the TS on Pd(111), the C atom sits almost on top of Pd(3), whereas on Cu(111), it is located nearly at the hollow site. On the other hand, on PdZn(111) (Fig. 3.7c), a pseudosymmetry plane is found along Zn(3)-Pd(4). The C atom is directed towards center Pd(4) and the O atom towards Zn(3), in agreement with the finding that the species CH_3 and O bind stronger to Pd and to Zn, respectively (Table 3.2).

The calculated activation energy of H abstraction from CH_3O adsorbed on the Pd(111) surface at 33 kJ mol^{-1} (Table 3.5, Fig. 3.6), is close to the value of 24 kJ mol^{-1} computed for

Table 3.5. Structural characteristics[a] (distances in pm) of transition states of C-H bond breaking of CH_3O on the (111) surfaces of the substrates Pd, Cu, and PdZn, as well as the corresponding activation energies E_a (kJ mol^{-1}).

Observable	C-H bond breaking		
	Pd	Cu	PdZn
H_a-M(3/4)[b]	177	182	177
C-M(3/4)[b]	250	264	288
O-M(1)	339	333	334
O-M(2)	208	215	355
O-M(3)	311	296	217
O-M(4)	322	298	346
C-H_a	139	152	170
C-H	111	112	111
C-O	133	131	130
z(H_a)	129	122	134
z(C)	225	240	249
z(O)	203	208	217
E_a	33	112	113

[a] A-B – distance between atoms A and B; z(A) – height of atom A above the "top" (111) surface plane.

[b] M(i/j) denotes atom i on Pd(111) and Cu(111) and atom j on PdZn(111); for the numbering of substrate centers, see Fig. 3.4. H_a refers to the hydrogen atom to be cleaved from CH_3O.

the system CH_3O/Pt(111) [108]. Such a low barrier implies that dehydrogenation of CH_3O on Pd(111) proceeds rapidly. On PdZn(111), however, we calculated a barrier of 113 kJ mol^{-1} for H abstraction. This value is more than three times larger than on Pd(111), indicating that on the flat PdZn(111) surface, hydrogen abstraction is much more difficult than on Pd(111). Our calculated barrier on Cu(111), 112 kJ mol^{-1} is close to the reported value of 137 kJ mol^{-1} [72]. This barrier height also is almost equal to that on PdZn(111), demonstrating that the surface chemistry of PdZn(111) is also kinetically similar to that of Cu(111).

Thus far, we found that the activation energies of C-H scission of CH_3O species on planar surfaces of the three substrates examined are 90–110 kJ mol^{-1} lower than the corresponding barriers of C-O bond breaking (Fig. 3.6, Tables 3.3 and 3.5). Therefore, C-H bond breaking is clearly favored over the C-O cleavage, in agreement with the experimental finding that on Pd surfaces C-H bond scission of CH_3O is the dominant reaction pathway [13,16].

3.3.3 Reaction Energy of CH_3OH Decomposition

Table 3.4 displays calculated reaction energies with respect to the initial steps of methanol decomposition on the three substrates under investigation. O-H bond cleavage of gas-phase methanol $CH_3OH(g)$ to adsorbed species $CH_3O(s)$ and H(s) (1) is exothermic on PdZn(111) and Cu(111) surfaces, but endothermic on Pd(111). This is mainly due to larger adsorption energy of CH_3O on Cu(111) and PdZn(111) than on Pd(111) (Table 3.2). Note that all these reaction energies, by absolute value, are rather small. The largest difference of reaction energies between Pd(111) and PdZn(111) as well as Cu(111) is found for the process $CH_3O(s) \rightarrow CH_2O(s) + H(s)$ (2). Owing to the larger binding energy of CH_3O on the surfaces PdZn(111) and Cu(111), dehydrogenation of CH_3O to formaldehyde on these substrates is endothermic by as much as 60–100 kJ mol^{-1}, while 45 kJ mol^{-1} are released on the Pd substrate where CH_3O is bound less strongly.

Another conceivable scenario to continue reaction 1 is C-O bond breaking, $CH_3O(s) \rightarrow CH_3(s) + O(s)$ (3), which might compete with reaction 2. On Pd(111), step 3 requires 5 kJ mol^{-1}, compared to -45 kJ mol^{-1} in step 2. Recall that the activation energy for C-H bond scission is ~110 kJ mol^{-1} lower than for C-O bond cleavage (Fig. 3.6, Tables 3.3 and 3.5). Therefore, step 2 is favored over step 3 on Pd(111), both thermodynamically and kinetically, in agreement with experimental observation [15]. On PdZn(111), C-O bond cleavage of

CH_3O leading to CH_3 (3) is predicted to absorb 60 kJ mol^{-1} of heat. This is the same value as on Cu(111), showing that on these two substrates the C-O bond breaking reaction 3 is thermodynamically notably unfavorable.

3.4 Conclusions

In this chapter we reported on a comparative periodic slab model study on the adsorption of a series of species C, H, O, CO, CH_3, CH_2O and CH_3O that are pertinent to methanol decomposition on planar Pd(111), Cu(111) and PdZn(111) surfaces. We found that the adsorption energies of these species on PdZn(111) are close to the corresponding values on Cu(111), implying that the reactivity of a bimetallic PdZn substrate is similar to that of monometallic Cu [50]. With the model that relates the position of the d-band center of the metal substrates to adsorption propensities, we were able to rationalize the calculated trend of the binding energies of adsorbed carbon atoms on different substrates, but not the trends for adsorbed oxygen atoms. Thus, due caution should be exercised when predicting adsorption trends using this model.

We also addressed two conceivable reaction steps of the initial stage of methanol decomposition, mediated by the mono- and bimetallic substrates mentioned above, and we characterized computationally both thermodynamics and kinetics of these elementary processes. Calculated activation energies showed that C-H bond cleavage is favored over C-O bond breaking in all cases studied, in line with the stronger C-O bonding. Due to the weaker interaction of CH_3O species with a Pd(111) substrate compared to PdZn(111) and Cu(111), the energy barriers for both C-H and C-O bond cleavage on Pd(111) are much lower than on the latter surfaces. Calculated energy barriers and reaction energies indicated that dehydrogenation of CH_3O to CH_2O is a very favorable process on Pd(111). In the proposed mechanism of methanol decomposition [5] formaldehyde is a necessary intermediate on both catalysts Pd and PdZn; different product distributions of methanol steam reforming on these substrates can be attributed to different reactions of formaldehyde. Hydrogen abstraction from adsorbed methoxide moieties to formaldehyde on PdZn(111) and Cu(111) was predicted to be slow because of high calculated activation barriers and endothermic reaction energies.

Thus far, we have used an idealized surface model allowing us to get insight into the complex surface structures of real catalysts. In the subsequent Chapters 4 and 5, we will

contribute to closing the “material gap” between theory and experiment by exploring how the more open PdZn(100) flat surface (Chapter 4) and PdZn(221) stepped surface (Chapter 5) change the reaction thermodynamics and barriers of CH_3O decomposition.

Chapter 4

Methoxide Decomposition on PdZn(100) Surface

A thorough understanding of the mechanism of methanol steam reforming on a Pd/ZnO catalyst is necessary to provide important guiding information for designing and producing new, more efficient steam reforming catalysts. Reactions on metal catalysts are known to depend often on the morphological structure of the active sites [80]; in Chapter 3, we addressed only sites on the ideal regular crystal (111) plane of PdZn which is characterized by the highest thermodynamical stability at 0 K. However, the (100) surface of PdZn was found to be just slightly less stable than the (111) surface and it was clearly favored over the surfaces of (001) and (110) orientations [50]. Therefore, the probability of (100) facets of PdZn catalysts to be exposed is close to that of (111) facets. In this chapter, we extend our investigation of methoxide decomposition on the more open PdZn(100) surface, where one atom occupies a ~6% larger area than on the PdZn(111) surface. As before, we start by investigating the adsorbed species H, O, CH_3, CH_2O and CH_3O involved in C-H and C-O bond breaking of methoxide on PdZn. Then, we examine the feasibility of these two reaction routes of methoxide decomposition by studying the corresponding TS structures.

4.1 Model

First, we briefly address the metal-metal distances on the (100) and (111) surfaces of the 1:1 PdZn alloy. The shortest hetero-nuclear and homo-nuclear distances on (100) are 268 and 339 pm, respectively, compared to 268 and 293 pm on the (111) surface. The next longer homo-nuclear distances are 415 pm on the (100) and 448 pm on the (111) surface. Thus, as already mentioned, the (100) surface is somewhat more open than the (111) surface and one can expect different adsorption and reactivity properties.

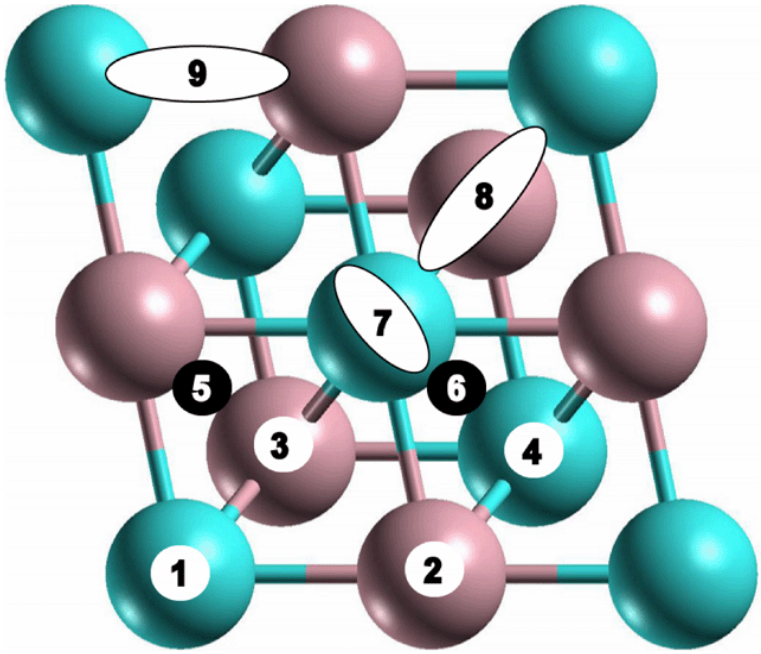

Figure 4.1. Adsorption sites studied on the PdZn(100) surface: T^{Pd} (1), T^{Zn} (2), $4H^{Pd2}$ (3), $4H^{Zn2}$ (4), $3H^{Pd2Zn}$ (5), $3H^{PdZn2}$ (6), Π (7), TBT^{Pd2} (8) and TBT^{PdZn} (9). Light red spheres – Zn, blue spheres – Pd.

One can classify the adsorption sites on the PdZn(100) surface by local coordination (Fig. 4.1): (*i*) two top sites (1 – T^{Pd} on Pd and 2 – T^{Zn} on Zn), (*ii*) two pseudo-4-fold hollow sites Pd_2Zn_2, one with a short Pd-Pd contact (3 – $4H^{Pd2}$) and one with a short Zn-Zn contact (4 – $4H^{Zn2}$), (*iii*) two 3-fold hollow sites Pd_2Zn (5 – $3H^{Pd2Zn}$) and $PdZn_2$ (6 – $3H^{PdZn2}$). According to our studies of pertinent adsorbates on the PdZn(111) surface in Chapter 3, H and C-bound species prefer sites with as many Pd atoms as possible whereas O and O-bound species tend to occupy positions dominated by Zn atoms. Therefore, dealing with the PdZn(100) surface, we only investigated H and CH_3 adsorbates on the sites T^{Pd}, $3H^{Pd2Zn}$, and $4H^{Pd2}$, whereas O and CH_3O adsorbates were studied on the sites T^{Zn}, $3H^{Pd2Zn}$, and $4H^{Zn2}$. The adsorption mode of a CH_2O molecule at a PdZn surface differs from that of the other species mentioned above. Formaldehyde interacts rather weakly with the bimetallic substrate, either through its C and O atoms forming a di-σ structure (top-bridge-top configuration, TBT) or through its C=O double bond leading to a π-bonded structure. For the CH_2O adsorbate, we examined one π adsorption complex (7 – Π) and two di-σ structures (8 – TBT^{PdZn}) with C-Zn and O-Pd contacts as well as (9 – TBT^{Pd2}) with C and O atoms attached to two different Pd atoms).

4.2 Adsorption of H, CH_3, O, CH_3O and CH_2O on PdZn(100) Surface

In this section we give an overview over the calculated structural and energetic parameters of the adsorption complexes of H, CH_3, O, CH_3O (Table 4.1) and CH_2O (Table 4.2) on

Table 4.1. Calculated distances [a] (pm) and binding energies BE (kJ mol^{-1}) of the adsorbates H, O, CH_3 and CH_3O on the surface PdZn(100) compared to the corresponding results for the surface PdZn(111)[b]

Adsorbate	Observable	Adsorption site		
		T^{Pd}	$3H^{Pd2Zn}$	$4H^{Pd2}$
H	H-Pd	161 (160)	190 (181)	188
	H-Zn		196 (206)	223
	z(H)	161 (160)	81 (96)	82
	BE	211 (214)	230 (245)	230
CH_3	C-H	110 (110)	110 (110)	108, 110
	C-Pd	216 (216)	274 (247)	255
	C-Zn		213 (250)	268
	z(C)	216 (216)	188 (189)	190
	BE	143 (145)	126 (122)	108
		T^{Zn}	$3H^{PdZn2}$	$4H^{Zn2}$
O	O-Pd			231
	O-Zn	177 (178)		198
	z(O)	177 (178)	$4H^{Zn2}$ [c]	102
	BE	296 (274)	(443)	458
CH_3O	C-O	140 (140)	145 (143)	144
	C-H	111 (111)	110 (110)	110
	O-Pd		226 (220)	249, 255
	O-Zn	188 (188)	228 (219)	224, 219
	z(C)	328 (328)	287 (290)	287
	z(O)	188 (188)	149 (148)	143
	BE	181 (161)	225 (216)	234

[a] A-B – distance between atoms A and B, z(A) – height of atom A above the "top" surface plane.

[b] Results at three-fold sites of PdZn(111) are averaged values between F^{Pd2Zn} and H^{Pd2Zn} for H and CH_3 or between F^{PdZn2} and H^{PdZn2} for O and CH_3O.

[c] The optimization of the position of adsorbed O was started at site $3H^{PdZn2}$, but resulted in an adsorption complex on site $4H^{Zn2}$.

PdZn(100), emphasizing similarities and differences with the corresponding parameters we calculated for the same adsorbates on the PdZn(111) surface (Chapter 3) and those important for discussing the reactivity in the next section.

4.2.1 Atomic Hydrogen

Like on other metals, hydrogen atoms on PdZn(111) tends to occupy adsorption sites that exhibit higher coordination. Not unexpectedly, 3-fold hollow $3H^{Pd2Zn}$ and (pseudo) 4-fold hollow $4H^{Pd2}$ (with the shortest Pd-Pd contact of 339 pm within the surface layer) are the sites calculated energetically favorable for H on PdZn(100) (Table 4.1). The adsorption energy of these two complexes, 230 kJ mol^{-1}, is 15 kJ mol^{-1} smaller than the average value on 3-fold hollow sites of the (111) surface. This is consistent with the longer H-Pd distance, 188–190 pm on the (100) surface compared to 181 pm on the (111) surface. H-Zn distances, 196 pm on the (100) surface and 206 pm on the (111) surface, do not correlate with the corresponding binding energies; thus, the H-Pd interaction dominates the adsorption of hydrogen. Indeed, H adsorption at $4H^{Pd2}$ hollow is favored by 54 kJ mol^{-1} over adsorption at the site $4H^{Zn2}$ that features a significantly longer Pd-Pd contact of 415 pm. The identical binding energy values calculated at the sites $3H^{Pd2Zn}$ and $4H^{Pd2}$ are indicative for a very flat potential energy surface (PES) of adsorbed H near the site $4H^{Pd2}$. According to a frequency analysis, site $3H^{Pd2Zn}$ is a local minimum for H atom adsorption and site $4H^{Pd2}$ is a saddle point.

4.2.2 Methyl

The adsorption of a CH_3 group on the PdZn(100) surface is very similar to that on PdZn(111), both structurally and energetically. On both surfaces, adsorption site T^{Pd} was calculated to be most favorable for CH_3 species with equal C-Pd distances, 216 pm, and essentially the same BE values of 143 and 145 kJ mol^{-1} (Table 4.1). Going from T^{Pd} to $3H^{Pd2Zn}$ and $4H^{Pd2}$ of PdZn(100), adsorbed CH_3 is destabilized by 17 kJ mol^{-1} [vs. 23 kJ mol^{-1} on PdZn(111)] and 35 kJ mol^{-1}, respectively.

4.2.3 Atomic Oxygen

On PdZn(111), the most stable adsorption position of atomic oxygen is at the 3-fold hollow site H^{PdZn2} with BE = 443 kJ mol^{-1}. When one starts optimization of oxygen adsorption at site $3H^{PdZn2}$ of PdZn(100), one ends up with an adsorption structure at site $4H^{Zn2}$, the most stable one on this surface, characterized by distances O-Zn = 198 pm and O-Pd = 231 pm as well as an interaction energy BE = 458 kJ mol^{-1} (Table 4.1). The latter value is about 160 kJ mol^{-1} larger than the adsorption energy at site T^{Zn}, which manifests, like on PdZn(111), a notably more corrugated PES than for H atoms that also tend to occupy highly coordinated sites. On Pd(100), the calculated O adsorption energy at a 4-fold hollow site (also using the PW91 functional) [91] is 64 kJ mol^{-} smaller than that on PdZn(100). This agrees with our previous conclusion that the interaction of O and O-bound species with PdZn alloy is enhanced compared to pure Pd metal.

4.2.4 Methoxide

In line with the observation that CH_3O species favor highly coordinated adsorption sites at metal substrates, the most stable calculated position of CH_3O on PdZn(100) is at site $4H^{Zn2}$ (Table 4.1), which is not present on PdZn(111). This structure at site $4H^{Zn2}$ is favored by 18 kJ mol^{-1} over the most stable adsorption structure H^{PdZn2} on PdZn(111). This difference is the main reason for the finding that CH_3O decomposition is more endothermic on PdZn(100) compared to the (111) surface (see Section 4.3). The adsorption complex of CH_3O is located slightly off site $4H^{Zn2}$ and its C-O axis is tilted by ~15° from the surface normal. The adsorbate-substrate interaction weakens the C-O bond of methoxide. The C-O stretching frequency of free CH_3O radicals is calculated at 1114 cm^{-1}; upon adsorption, it decreases to 954 cm^{-1} on PdZn(100) at $4H^{Zn2}$ (see Table B8, ν_9 of Appendix B). This value is 49 cm^{-1} smaller than the frequency of the most strongly adsorbed species on PdZn(111), consistent with the larger binding energy of CH_3O on the (100) surface.

4.2.5 Formaldehyde

We studied three adsorption structures of CH_2O on PdZn(100): two di-σ complexes denoted as TBT^{PdZn} and TBT^{Pd2} and one Π configuration (Fig. 4.1, Table 4.2). According to our

Table 4.2. Calculated binding energies BE (kJ mol^{-1}) and geometries (pm), bond distances O-M, M = Pd/ Cu, Zn and z(O) – height of carbon above the "top" (111) plane of the substrate of formaldehyde on various high symmetry adsorption sites of Pd(111), Cu(111) and PdZn(111) surfaces.

	BE	C-Pd	O-Pd/ Zn	C-O	C-H
Π	20	230	231	126	111
TBT^{Pd2}	15 (10)	239 (246)	254 (237)	127 (126)	110 (111)
TBT^{PdZn}	24 (23)	227 (225)	208 (223)	130 (130)	110 (110)

previous calculations, CH_2O binds very weakly to PdZn: the largest binding energy of CH_2O on the (111) surface, only 23 kJ mol^{-1}, was obtained for the TBT^{PdZn} configuration. A similar situation was found on PdZn(100) where practically the same binding energy, 24 kJ mol^{-1}, was calculated at the most stable site, TBT^{PdZn}, with the C-O distances identical, 130 pm, on both surfaces. The other di-σ structure, at TBT^{Pd2}, is 9 kJ mol^{-1} less stable than the complex at TBT^{PdZn}. The binding energy of the Π configuration is 20 kJ mol^{-1}, slightly less stable than the TBT^{PdZn} structure with almost similar C-Pd and O-Pd distance of ~230 pm. Because of the *weak* interaction of CH_2O with PdZn(100), no further details on the structure of the adsorption complexes are important.

4.2.6 Trends in Adsorption Properties of the (111) and (100) Surfaces

The observed trends for five different types of adsorbates considered on the two surfaces show that switching from the (111) to the (100) surface slightly increases the adsorption strength of all adsorbates except atomic H (Table 4.1). Substrate atoms of more open surfaces are expected to exhibit enhanced bonding abilities. The results of the present study corroborate this anticipation: binding energies are calculated larger on PdZn(100) than on PdZn(111). The only exception, H binds more weakly on PdZn(100), is most likely due to the very small size of the adsorbate which prevents it from forming H-Pd contacts of optimal length at hollow site on the more open PdZn(100) surface where the shortest Pd-Pd distance, 339 pm, is notably larger than on the denser surface PdZn(111), 293 pm. This structural property does not affect the binding energy at an on top site, but will do so at hollow sites. Indeed, the binding energies of H at T^{Pd} of the (100) and (111) surfaces differ only by 3

kJ mol^{-1}, but by 14 kJ mol^{-1} for corresponding 3-fold hollow sites (Table 4.1). In summary, the calculated adsorption properties of the PdZn(100) surface (with respect to stable adsorbed species) differ only slightly compared to those of the (111) surface. Next, we examine the influence of the surface morphology on the methoxide decomposition reaction and, more importantly, on the activation energies.

4.3 Transition State Structures, Activation Energies and Reaction Rate Constants for C-H and C-O Bond Breaking of Adsorbed CH_3O

As IS of both reactions of adsorbed CH_3O on PdZn(100), C-H and C-O bond breaking, we chose a structure where the adsorbate occupies the hollow site $4H^{Zn2}$, formed by the atoms Pd(1), Zn(2), Pd(3), and Zn(4) (Fig. 4.2a), with the O center located in perfect pseudo 4-fold position.

4.3.1 C-H Bond Cleavage

In the beginning of C-H bond breaking, the C-O bond tilts towards Pd(1) and, concomitantly,

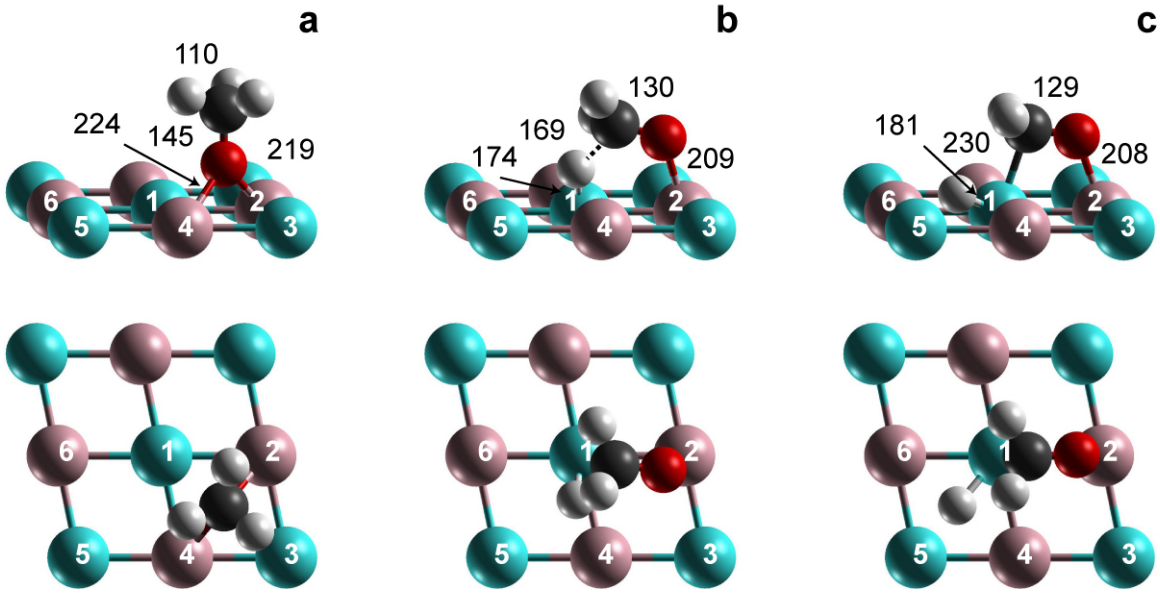

Figure 4.2. Sketches of (a) initial state, (b) transition state, and (c) final state structures involved in the C-H bond breaking of CH_3O on the PdZn(100) surface. Upper panel displays the side view and lower panel shows the top view. Selected bond distances (pm) are shown. Atomic spheres: blue – Pd, pink – Zn, red – O, black – C, light gray – H.

the O atom moves on top of Zn(2). This C-O tilting brings the H atom to be dissociated (H_a) closer to atom Pd(1), thus increasing the H_a-Pd(1) interaction which, in turn, leads to weakening and lengthening of the C-H_a bond. In the TS structure (Fig. 4.2b), the C-O bond, shrunk from 145 pm in the IS to 130 pm, is almost parallel to the substrate surface, forming an angle of ~15° with the (100) plane. The C-H_a bond is stretched from 110 pm in the IS to 169 pm in the TS, whereas the H_a-Pd contact is simultaneously shortened to 174 pm (Fig. 4.2b). These two distances are close to 170 pm (C-H_a) and 177 pm (H_a-Pd) calculated on the PdZn(111) surface. In fact, the process on PdZn(100) overall is very similar to that on the (111) surface. After the TS, H_a moves towards the atom Pd(5). In the final state (FS), atom H_a is located very close to site $4H^{Pd2}$ with H_a-Pd(1) = 181 pm and H_a-Pd(5) = 184 pm (Fig. 4.2c). The latter two distances are similar to the distance of 188 pm, formed by isolated H adsorbates with Pd atoms at site $4H^{Pd2}$ on PdZn(100); they reveal a moderate distortion caused by the nearby CH_2O adsorbate. The C-O bond of the FS structure, 129 pm, is almost parallel to the substrate plane (100), the angle with the surface is less than 10°.

The calculated activation barrier E_a of C-H bond breaking of methoxide on the PdZn(100) surface, 107 kJ mol^{-1}, is only 6 kJ mol^{-1} lower than on the (111) surface. After zero-point energy correction, which comprises up to 20% of the activation energy, the barrier decreases to 93 kJ mol^{-1} (Table 4.3). The calculated pre-exponential factor is 2×10^{12} s^{-1}. For

Table 4.3. Calculated reaction energies E_r, activation energies E_a and E_a^0 without and with corrections for zero-point energies, pre-exponential factors A^0, and reaction rate constants κ at 300 K for C-H and C-O bond breaking of CH_3O species adsorbed on PdZn(100) and PdZn(111) surfaces. [a]

Parameter	C-H bond breaking		C-O bond breaking	
	(111)	(100)	(111)	(100)
E_r, kJ mol^{-1}	61	89	60	65
E_a, kJ mol^{-1}	113	107	208	167
E_a^0, kJ mol^{-1}	93	90	198	158
A^0, s^{-1}	1×10^{13}	2×10^{12}	3×10^{12}	5×10^{12}
κ, s^{-1}	8×10^{-4}	4×10^{-4}	1×10^{-22}	2×10^{-15}

[a] Reaction energies were calculated as $E_r = \Sigma(E)^P - \Sigma(E)^R - \Sigma(BE)^P + \Sigma(BE)^R$, where $\Sigma(E)^P$ and $\Sigma(E)^R$ are sums of total energies E for all products (P) and reactants (R) in the gas phase, respectively. $\Sigma(BE)^P$ and $\Sigma(BE)^R$ are sums of calculated binding energies for isolated product and reactant species, respectively. A positive value of E_r corresponds to an endothermic process.

comparison, this quantity was estimated for the decomposition of methoxide on Ni(110) to fall in the range 10^{11}–10^{13} s^{-1} based on experimental data [109]. The pre-exponential factor for the decomposition on PdZn(111), 1×10^{13} s^{-1}, is almost five times larger than the value computed on PdZn(100). This is mainly due to two low frequencies which correspond to hindered translational motion of the adsorbate on the substrate surface, 72 cm^{-1} (ν_{13}) and 33 cm^{-1} (ν_{14}) on (111) (see Table B8 of Appendix B), which are calculated larger on the (100) surface, 126 cm^{-1} and 63 cm^{-1}, respectively (see Table B8 of Appendix B). This factor renders the rate constant of C-H bond breaking on PdZn(111), 8×10^{-4} s^{-1}, slightly larger than that on the (100) surface, even though the energy barrier is somewhat higher for the former system (Table 4.3).

The reaction energy of methoxide C-H bond breaking on the (100) surface, $E_r = 89$ kJ mol^{-1}, is 28 kJ mo^{-1} more endothermic (and thus less favorable) than on the PdZn(111) surface (Table 4.3). That increase of the endothermicity on PdZn(100) compared to PdZn(111) is a combined effect of increased binding energy of the reactant CH_3O and decreased binding energy of the product H on the (100) surface compared to the (111) surface (Table 4.1). To summarize, both kinetic and thermodynamic results indicate that C-H bond breaking of adsorbed CH_3O is somewhat less favorable on PdZn(100) than on PdZn(111).

4.3.2 C-O Bond Cleavage

At the beginning of the reaction, the C-O bond of CH_3O tilts and the methyl group moves towards Pd(1). Then, the distance between C and Pd(1) decreases and their interaction increases. At the TS (Fig. 4.3a), this distance has decreased to 236 pm from 349 pm in the IS. The marginal difference between the distance C-Pd(1) and the height z(C) = 232 pm clearly shows that the C atom is positioned almost on top of Pd(1) atom. The normal of the plane P^{H3}, formed by the three H centers, is tilted by ~33° with respect to the substrate normal. In the TS, the C-O distance increased to 190 pm, 17 pm less than on the (111) surface. The contacts O-Pd(1) and O-Pd(3) are 227 and 250 pm long, respectively, implying that the O center moved from $4H^{Zn2}$ in the IS to $3H^{PdZn2}$. In the FS, the distance C-Pd(1) is further reduced to 216 pm and the methyl group is placed almost on top of Pd(1); the plane P^{H3} is roughly parallel to the surface (Fig. 4.3b). The distances O-Pd(1) and O-Pd(3) become 245 and 217 pm, respectively, compared to 227 and 250 pm in the TS. Thus, the atom O retreats from site $3H^{PdZn2}$ Pd(1)Zn(2)Zn(4) to another 3-fold hollow site of the same type H^{PdZn2} Zn(2)Pd(3)Zn(4). The

underlying mechanism of this displacement is probably bond competition [107]. In general, also C-O bond breaking proceeds very similarly as on the (111) surface.

The calculated barrier E_a, 167 kJ mol^{-1}, is 41 kJ mol^{-1} lower than the corresponding activation energy at the (111) surface, 208 kJ mol^{-1} (Table 4.3). Zero-point energy correction reduces the barrier by 10 kJ mol^{-1}, compared to ~20 kJ mol^{-1} for C-H bond cleavage; the latter correction is larger because a high frequency C-H stretch disappears in the TS of C-H breaking. The pre-exponential factors of C-O bond breaking on the two surfaces under study are close, 3×10^{12} s^{-1} for (111) and 5×10^{12} s^{-1} for (100). Because the activation barrier of C-O scission of CH_3O on PdZn(100) is notably lower than that on the (111) surface, the calculated rate constant on (100), 2×10^{-15} s^{-1}, is 7 orders of magnitude larger than that on (111), 1×10^{-22} s^{-1}. Nevertheless, the resulting rate constant of C-O breaking on PdZn(100) is still too small to be relevant. Therefore, C-O bond cleavage of adsorbed CH_3O is an extremely slow process on both ideal surfaces of PdZn, (111) and (100). Finally, because the binding energy of CH_3O is higher on the (100) surface than on the (111) surface, the calculated reaction energy on

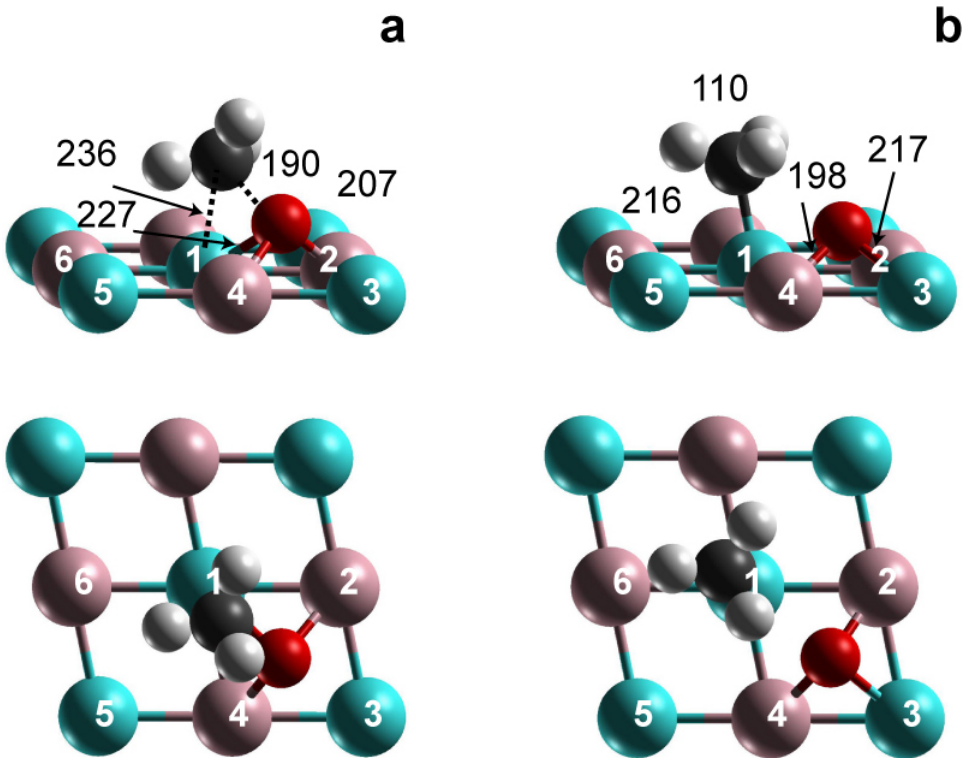

Figure 4.3. Sketches of (a) transition state and (b) final state structures involved in the C-O bond breaking of CH_3O on the PdZn(100) surface. Upper panel displays the side view and lower panel shows the top view. Selected bond distances (pm) are shown. Atomic spheres: blue – Pd, pink – Zn, red – O, black – C, light gray – H.

PdZn(100), 65 kJ mol^{-1}, is slightly larger (more endothermic) than the value computed for PdZn(111), 60 kJ mol^{-1}. However, this small difference is essentially irrelevant in the light of the severe kinetic hindrance of C-O bond breaking.

4.4 Conclusions

In this chapter, we theoretically quantified adsorption properties of regular (100) facets of the 1:1 PdZn alloy with respect to the species involved in the initial phase of methanol decomposition. We characterized pertinent adsorption complexes (H, O, CH_2O, CH_3, and CH_3O) as well as the transition state structures for both C-H and C-O bond breaking reactions of methoxide. We performed a detailed comparative analysis of these data with the results calculated for the same elementary reactions on ideal (111) facets of PdZn catalysts to clarify effects of surface orientation on the reactivity.

The binding energies of these adsorbates (apart from atomic H) were calculated somewhat larger on the (100) surface than on the (111) surface. The transition state structures for C-H and C-O bond breaking on PdZn(100) are similar to those on the (111) surface. However, thermodynamically both reactions become slightly less favorable on the (100) surface because of the calculated relative stabilization of the reactant CH_3O on PdZn(100).

The energy barrier for C-O scission is 20% smaller on the (100) than on the (111) surface. As a result, the rate constant on the (100) surface is substantially larger, but it is probably still too small to be relevant. The activation energy of C-H bond breaking is slightly smaller on the (100) surface. However, due to the larger pre-exponential factor on the PdZn(111) surface, the rate constant of C-H bond breaking turns out to be larger on this surface. From the calculated variations of energy barriers for C-H and C-O bond breaking one deduces that C-O scission is more sensitive to the surface structure than C-H bond breaking. These conclusions agree with a recent report by Libuda et. al. that on Pd model catalysts, C-H bond scission shows no preference for specific sites, whereas C-O bond scission preferentially occurs at particle edges, steps, defects or (100) sites [110]. A similar conclusion has also been drawn regarding C-H bond breaking of CH_4 compared to C-O dissociation [111]: when going from flat to stepped and kinked surfaces of Pd and Rh, the C-O dissociation barrier decreased about 3 times more than the barriers for C-H bond breaking.

So far, our results on regular (111) and (100) surfaces showed that C-H bond cleavage of CH_3O is more facile than C-O dissociation. However, the calculated activation and reaction energies indicate that the formation of formaldehyde from CH_3O via C-H breaking is still slow. In the next chapter, we will explore if the stepped PdZn(221) surface is more active in methoxide decomposition.

Chapter 5

Effects of PdZn(221) Steps on Methanol Decomposition

In the field of surface science, the study of the interaction of molecules with metals has traditionally focused on low-index surface planes. The preparation of these well-defined surfaces in ultra-high vacuum (UHV) chambers and the subsequent adsorption of molecules on them has been a remarkable success over the past decades. On the other hand, technologically relevant catalysts expose non-ideal rough surfaces and are operated under much higher pressures. These discrepancies between real-world applications of heterogeneous catalysis and basic research are called “structure and pressure gap” [112].

It is widely known that imperfections of the surface, e.g. steps, help promote the reactivity of a catalyst [113]. One way to bridge the structural gap between surface science and applied heterogeneous catalysis is to carry out theoretical studies on a well-defined stepped surface, and thus identify the effect of steps on the surface reactivity [114].

The decomposition of methoxide on a PdZn alloy is considered to be the rate-limiting step of methanol steam reforming over Pd/ZnO catalyst [9-13,18]. In the previous two chapters, we have shown that the defect-free flat (111) and (100) PdZn surfaces have low propensity to promote C-H or C-O bond breaking of methoxide. In this chapter, we report on a study where we applied the same DF periodic slab-model approach to investigate the effect of PdZn(221) surfaces that expose Pd, $(221)^{Pd}$, and Zn, $(221)^{Zn}$ steps (see Fig. 5.1) on the reactivity of these two routes of methoxide decomposition.

5.1 Models

The PdZn(111) surface has been predicted to be exposed preferentially due to the lowest calculated surface energy [50]. Thus, we selected the stepped surface PdZn(221) [4(111)×(111)] to be our model [56]; this surface features terraces of 4 atomic rows and a monatomic step, both of (111) orientation. We considered periodic slabs which consist of four stepped layers with eight atoms per layer in each unit cell (Fig. 5.1). There are two different types of stepped surfaces PdZn(221), depending on the atoms constituting the steps: one, denoted $(221)^{Pd}$, exposes Pd steps and the other, $(221)^{Zn}$, features steps built of Zn atoms; we studied both types of models (Fig. 5.1).

Stepped surfaces are assumed to undergo a notable relaxation with respect to bulk-terminated atomic positions [56]. Therefore, the top two stepped layers of PdZn(221) were allowed to relax (without an adsorbate), whereas the bottom two layers were kept frozen at the optimized truncated-bulk geometry. This relaxation of the slab models lowered the total energy by 24 kJ mol^{-1} for $(221)^{Pd}$ and 26 kJ mol^{-1} for $(221)^{Zn}$. Concomitantly, the relaxation slightly shortens the heteronuclear bonds with respect to the calculated bulk-terminated values, at most by 10 pm for the distances between the less-coordinated edge atoms and their neighbors. Due to the smaller surface energy of Zn compared to Pd, Zn atoms of a $(221)^{Pd}$ slab tend to move towards the surface, whereas Pd atoms move in the direction of the bulk; all calculated displacements were smaller than 16 pm. Homonuclear bond distances along the step (Fig. 5.1) do not undergo any essential relaxation. However, homonuclear bond distances

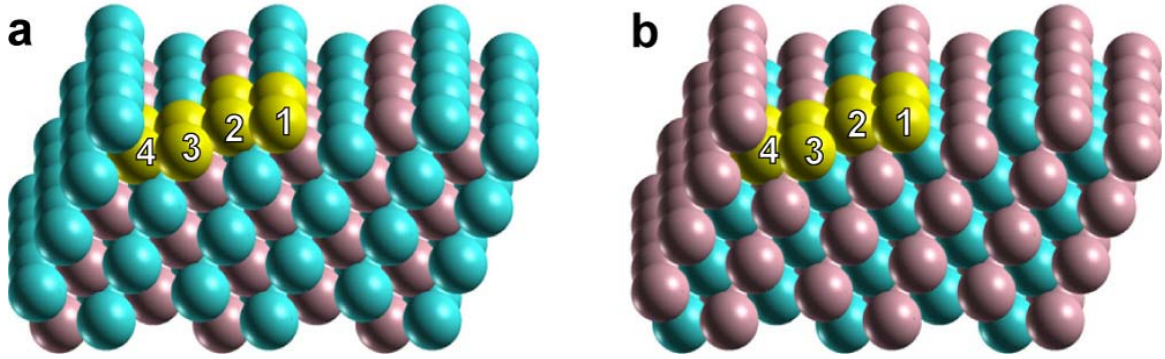

Figure 5.1. Slab models of PdZn(221) surfaces exposing (a) a step built of Pd atoms, $(221)^{Pd}$, and (b) a step built of Zn atoms, $(221)^{Zn}$. Blue spheres – Pd, pink spheres – Zn. Yellow spheres indicate atoms in the surface unit cell; numbers identify the atomic rows at the terraces.

perpendicular to the step direction, i.e. bonds between the same type of atoms, one at a step edge and the other on the neighboring terrace, vary notably. Such nearest-neighbor bonds were calculated to shrink by 16 pm on $(221)^{Pd}$ and 11 pm on $(221)^{Zn}$ surfaces, while the corresponding next-nearest bond distances were extended by 13 pm and 5 pm, respectively; for details see Table C3 of Appendix C.

The substrate atoms were fixed at their relaxed geometry positions during the subsequent geometry optimization of adsorption complexes and the location of TS structures were positioned on the relaxed side of the slab models; all degrees of freedom of the adsorbed moieties were optimized. We studied adsorption complexes of reactants and products involved in the decomposition of methoxide via C-H and C-O bond breaking: H, O, CH_3, CH_2O and CH_3O.

According to our previous computational investigations on (111) and (100) surfaces of PdZn (see Chapters 3 and 4), H and C-bound CH_3 species prefer sites with mainly Pd atoms, while O and O-bound CH_3O species tend to occupy sites dominated by Zn atoms. CH_2O molecules have been found merely weakly bound to PdZn surfaces; they favor slightly a top-bridge-top configuration (TBT^{PdZn}), where C and O atoms of the adsorbate interact with substrate Pd and Zn atoms, respectively. Therefore, on PdZn(221) surfaces, we only addressed adsorption complexes of H and CH_3 species at the sites T^{Pd} (top Pd) and H^{Pd2Zn} (pseudo-hcp 3-fold hollow site, formed by one Zn and two Pd atoms in the upper slab layer), of O and CH_3O moieties on the sites T^{Zn} (top Zn) and H^{PdZn2} (pseudo-hcp 3-fold hollow site of one Pd and two Zn atoms) and the TBT^{PdZn} structure of adsorbed CH_2O. Surface sites located directly at step edges or in their immediate vicinity are generally assumed to be more

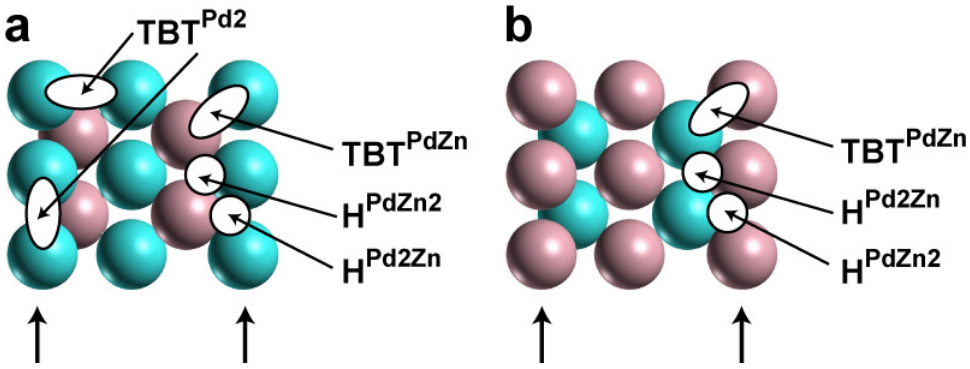

Figure 5.2. Selected adsorption sites on (a) $(221)^{Pd}$ and (b) $(221)^{Zn}$. Blue spheres – Pd, pink spheres – Zn. The arrow at the bottom of each sketch points to the row of edge atoms.

active than sites on terraces [113]; therefore, only these former sites of PdZn(221) were considered when searching for preferred configurations of the adsorption complexes (see Fig. 5.2 for explanation of pertinent adsorption sites).

Table 5.1. Selected interatomic distances (A-B, pm)[a] and binding (adsorption) energies (*BE*, kJ mol^{-1}) of adsorbates relevant to CH_3O decomposition, calculated on favored sites of PdZn(221) surfaces exposing Pd, $(221)^{Pd}$, and Zn, $(221)^{Zn}$, steps. Also shown are adsorption parameters of the most stable complexes on the flat surfaces PdZn(111) and PdZn(100).

Adsorbate	Parameter	PdZn Surface			
		$(221)^{Pd}$	$(221)^{Zn}$	(111)	(100)
H	H-Pd	176 / 176	184 / 184	183 / 183	190 / 190
	H-Zn		197	192	196
	BE	253	229	249	230
O	O-Pd	239	226	213	231
	O-Zn	191 / 191	189 / 189	193 / 193	198 / 198
	BE	407	472	449	458
CH_3	C-Pd	211	223	216	216
	BE	165	118	145	143
CH_2O	C-O	124	140	130	130
	O-Pd	293 / 230		271	283
	O-Zn	354	207 / 210	223	208
	C-Pd	317 / 371	219	225	227
	C-Zn	380			290
	BE	43	45	23	24
CH_3O [b]	O-Zn	304	203 / 203	211 / 211	219 / 224
	O-Pd	217 / 221	320 / 323	231	249 / 255
	C-O	145	144	143	145
	BE	204	262	221	234

[a] When X (X = C, O) is bound to two substrate atoms M, two values X-M are given

[b] Another CH_3O adsorption complex, on the hollow site H^{PdZn2} of the $(221)^{Pd}$ terrace, is equally stable, *BE* = 204 kJ mol^{-1}, as the complex on the step-edge; its structural characteristics are O-Zn = 209 / 209 pm, O-Pd = 255 pm, and C-O = 143 pm.

5.2 H, O, CH_3, CH_2O and CH_3O Species on PdZn(221) Surface: Adsorption Structures and Energetics Relevant to CH_3O Decomposition

Table 5.1 shows selected distances and binding energy values for the five adsorbates under scrutiny, calculated at the most favorable sites on the surfaces $(221)^{Pd}$ and $(221)^{Zn}$ of PdZn alloy; for comparison, we also provide the results for the flat PdZn surfaces (111) and (100). In the following, we briefly comment the data, emphasizing those differences brought about by the presence of the Pd and Zn steps, which are reflected in altered reaction energies compared to the flat surfaces.

5.2.1 Atomic Hydrogen

On flat PdZn surfaces, H atoms prefer higher coordination sites dominated by Pd atoms. On the $(221)^{Pd}$ surface, H was calculated to favor a bridge site on the step edge. The H-Pd distances are 7 to 14 pm shorter than on the flat surfaces, in line with the fact that adsorption energies are larger by 4 to 23 kJ mol^{-1} (Table 5.1); this can be rationalized by the enhanced bonding capability of edge Pd atoms due to their lower coordination. The preferred adsorption complex of H atom on the $(221)^{Zn}$ surface, on a 3-fold hollow Pd_2Zn site of the terrace, is destabilized by 24 kJ mol^{-1} compared to the most favorable complex on $(221)^{Pd}$; it features somewhat longer H-Pd distances.

5.2.2 Atomic Oxygen

The most stable position of adsorbed O on a $(221)^{Pd}$ surface is a hollow site formed by an edge Pd atom and two Zn atoms of the second row (see Fig. 5.1). There, despite slightly shorter O-Zn bond lengths, the interaction with the substrate is notably reduced, by 40 to 50 kJ mol^{-1}, with respect to the flat surfaces (Table 5.1). On the $(221)^{Zn}$ surface, atom O preferentially occupies a 3-fold hollow site comprising two edge Zn atoms and one Pd atom of the second row (Fig. 5.1). This moiety is most strongly bound among all adsorption complexes on PdZn considered so far, 65 kJ mol^{-1} stronger than on $(221)^{Pd}$ and ~10 to 20 kJ mol^{-1} stronger than on the flat surfaces.

5.2.3 Methyl

While H atoms favor hollow sites, CH_3 adsorbates favor sites on-top Pd. At the $(221)^{Pd}$ surface, CH_3 prefers to be located on-top of a step-edge Pd atom. There is an energy gain of ~20 kJ mol^{-1} with respect to adsorption on the (111) and (100) surfaces, accompanied by a reduced C-Pd bond length (Table 5.1). The interaction of CH_3 with the $(221)^{Zn}$ model was calculated to be the weakest among all methyl adsorption complexes studied so far (~25 kJ mol^{-1} weaker than on the flat surfaces) and it features the longest C-Pd bond.

5.2.4 Formaldehyde

The adsorption of CH_2O on flat PdZn surfaces was calculated to be very weak, less than 25 kJ mol^{-1}. On both surfaces studied, $(221)^{Pd}$ and $(221)^{Zn}$, the adsorption energies are increased by ~20 kJ mol^{-1} (Table 5.1) compared to the flat PdZn surfaces to values comparable to the interaction on the Pd(111) surface, but the binding energies on PdZn(221) are still rather small. The adsorption complex of CH_2O on $(221)^{Pd}$ has a pseudo top-bridge-top structure (TBT^{Pd2}, see Fig. 5.2) with the O atom over a step Pd atom and the C atom on top of a Pd atom at the lower terrace. On $(221)^{Zn}$, the O atom binds to two step Zn atoms with almost equal bond lengths, and the C atom attaches to a Pd atom of the upper terrace. The C-O bond is essentially in the symmetry plane that is normal to the step edge. Also, due to the shallow potential energy surfaces, structural details of the adsorption complexes of CH_2O appear to be less significant in the context of the present study (see Table 5.1 and Table C4 of Appendix C).

5.2.5 Methoxide

On the $(221)^{Pd}$ surface, CH_3O is calculated to adsorb in a bridge position, bound to two edge Pd atoms with relatively short O-Pd distances of 217 and 221 pm; the nearest O-Zn contact of 304 pm is essentially nonbonding. The C-O bond of 145 pm is tilted by 40º from the perpendicular to the (111) terraces. The calculated adsorption energy of 204 kJ mol^{-1} – the lowest one among the methoxide complexes presently discussed (Table 5.1) – reflects the fact that favorable O-Zn interactions are absent in this structure. The C-O stretching frequency is shifted down to 925 cm^{-1} compared to 1114 cm^{-1}, calculated for gas phase CH_3O. With *BE* =

Table 5.2. Reaction energies, E_r [a] (kJ mol^{-1}) calculated for C-H and C-O bond breaking of CH_3O on stepped PdZn(221) surfaces in comparison with the analogous reactions on the flat surfaces PdZn(111) and PdZn(100).

Parameter	Sites on PdZn			
	$(221)^{Pd}$	$(221)^{Zn}$	(111)	(100)
C-H	17	97	61	89
C-O	65	105	60	65

[a] The heat of reaction is calculated as $E_r = \Sigma E_P - \Sigma E_R - \Sigma BE_P + \Sigma BE_R$, where ΣE_P and ΣE_R are sums of the total energies E of products (P) and reactants (R), respectively, in the gas phase. ΣBE_P and ΣBE_R are sums of the (adsorbate-substrate) binding energies BE of isolated product and reactant species, respectively. A positive value of E_r characterizes an endothermic reaction.

204 kJ mol^{-1} (see footnote of Table 5.1), methoxide species adsorbed on the hollow sites H^{PdZn2} of $(221)^{Pd}$ terraces are as stable as the structure on the step edges just discussed. The most favorable adsorption site of CH_3O on PdZn studied so far is at a step-bridge site of the $(221)^{Zn}$ surface (Table 5.1); the calculated binding energy of 262 kJ mol^{-1} is 41 and 28 kJ mol^{-1} larger than that on the preferred sites on (111) and (100) surfaces, respectively. The complex CH_3O/PdZn$(221)^{Zn}$ exhibits the shortest CH_3O-Zn bond overall and a C-O vibration at 993 cm^{-1}.

The above comparison of adsorption geometries and energies on stepped and flat PdZn surfaces does not exhibit particularly large changes (Table 5.1). However, there is a clear trend that the Pd and Zn atoms located at steps form somewhat stronger bonds with all adsorbates under discussion than the atoms of flat PdZn surfaces; obviously due to their lower coordination numbers, atoms at step sites feature a higher unsaturated valence than atoms on terraces. The binding energies on flat surfaces are between those on the two stepped surfaces, $(221)^{Pd}$ and $(221)^{Zn}$ (Table 5.1).

Finally, we discuss the consequences of these bond strengthening effects for adsorbed CH_3O reactants in the IS as well as for the products in the FS of either bond breaking reaction, CH_2O + H (C-H) and CH_3 + O (C-O). The overall changes for stepped PdZn surfaces result in a more or less favorable reaction energetics (heat of reaction), compared to flat PdZn surfaces.

Recall (see Chapters 3 and 4) that on flat PdZn surfaces both the C-H and C-O decomposition channels were calculated to be endothermic, with heats of reaction of 61 and 89 kJ mol^{-1} (C-H), and 60 and 65 kJ mol^{-1} (C-O) on PdZn(111) and PdZn(100), respectively. On the basis of calculated reaction energies for stepped substrate models, C-H bond scission on $(221)^{Pd}$ is ~40 kJ mol^{-1} *less endothermic* than on PdZn(111) and ~70 kJ mol^{-1} less endothermic than on PdZn(100). On the other hand, the C-H bond breaking reaction on the $(221)^{Zn}$ surface is *more endothermic* than on the flat surfaces by ~40 kJ mol^{-1} on (111) and ~10 kJ mol^{-1} on (100). Neither $(221)^{Pd}$ nor $(221)^{Zn}$ step sites help to render C-O bond breaking thermodynamically more favorable (less endothermic) than on the flat (111) and (100) surfaces. In summary, of the step surface sites of PdZn(221) considered here, only the $(221)^{Pd}$ site appears to offer a favorable thermodynamics for C-H bond breaking of CH_3O; for a more detailed account of the calculated heats of reaction see Table 5.2.

5.3 Kinetics of CH_3O Decomposition on PdZn(221) Surface

As already mentioned, there are two local minima for CH_3O adsorbates on the stepped $(221)^{Pd}$

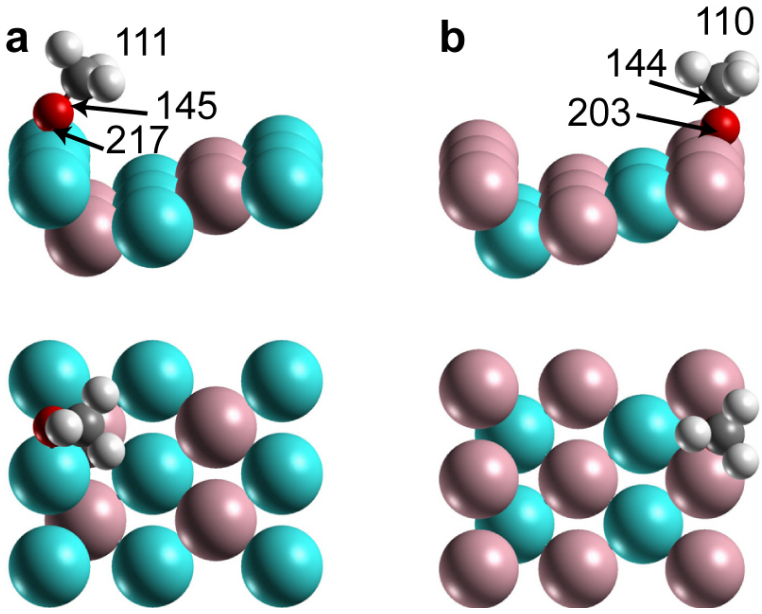

Figure 5.3. Side (upper panels) and top views (lower panels) of calculated IS involved in C-H and C-O bond breaking of CH_3O on (a) $(221)^{Pd}$ and (b) $(221)^{Zn}$. Selected bond-lengths are given in pm. Atomic spheres: blue – Pd, pink – Zn, red – O, dark gray – C, light gray – H.

surface which feature the same stability: at step-edge bridge sites and at hollow sites on terraces. As step sites are considered to be more active than sites of terraces, we chose the former structure to model the IS of methoxide decomposition on this surface (Fig. 5.3a). The choice of the IS structure on the $(221)^{Zn}$ surface is unequivocal (see above and Fig. 5.3b).

5.3.1 C-H Bond Cleavage

On the $(221)^{Pd}$ surface, we located two TS structures for C-H bond cleavage that differ in the position of the dissociated hydrogen atom (H_a). In the first structure (referred to as TS^{terr}), H_a ends up on a terrace site, whereas in the second structure (referred to as TS^{edge}), H_a is finally positioned on a bridge site at the Pd step edge. The TS of C-H cleavage on the $(221)^{Zn}$ surface is characterized by a bridge position of the atom O on the Zn step edge. In the following, we will outline the profiles of C-H bond breaking of CH_3O and characterize the TS structures (Figs. 5.4 to 5.6). The corresponding calculated kinetic parameters are collected in Table 5.3.

TS with H_a on the terrace of $(221)^{Pd}$

The reaction via TS^{terr} to FS (Fig. 5.4), in which H_a is located on terrace, begins with the C-O bond tilting of CH_3O towards the terrace. After sufficient progress, this motion eventually allows a H_a-Pd interaction with a concomitant weakening of the C-H_a bonding. In the TS^{terr}, the nearest H_a-Pd contact reaches 169 pm, whereas the C-H_a length increases from 111 pm to

Table 5.3. Kinetic parameters[a] calculated for C-H bond breaking of CH_3O on stepped PdZn(221) surfaces in comparison with the analogous reactions on the flat surfaces PdZn(111) and PdZn(100).

Parameter	Sites on PdZn				
	$(221)^{Pd}$terrace	$(221)^{Pd}$edge	$(221)^{Zn}$	(111)	(100)
E_a	49	53	108	93	90
A^0	3×10^{13}	2×10^{13}	6×10^{12}	1×10^{13}	2×10^{12}
κ	7×10^{4}	1×10^{4}	1×10^{-6}	8×10^{-4}	4×10^{-4}

[a] Activation energies E_a (kJ mol^{-1}) corrected for zero-points, pre-exponential factors A^0 (s^{-1}), and reaction rate constants κ (s^{-1}) at 300 K.

165 pm. These distances are somewhat shorter than on flat (111) surface, H_a-Pd = 177 pm and C-H_a = 170 pm (see Table 3.5). In the TS, the C-O bond, 130 pm, is almost perpendicular to the step orientation. The O atom is basically at a step-edge bridge site, with two O-Pd distances of 233 and 236 pm. The atom H_a sits on the bridge site exactly between two terrace Pd atoms at distances of 183 pm. The calculated zero-energy corrected activation barrier for this reaction path, 49 kJ mol^{-1}, is more than 40 kJ mol^{-1} *lower* than the corresponding barriers on the (111) and (100) surfaces. As a consequence, the reaction rate constant at 300 K, 7×10^4 s^{-1}, is 10^8 times larger than on the flat surfaces (Table 5.2). Such a significant rate constant indicates that C-H bond breaking of adsorbed methoxide on stepped $(221)^{Pd}$ surface is feasible, at variance with the low activity of terrace sites studied previously.

TS with H_a on the step-edge of $(221)^{Pd}$

Similarly to the above reaction, this profile (via TS^{edge}) also starts with tilting of the C-O bond but in a different direction – almost parallel to the step. In the TS^{edge}, the C-O axis forms an

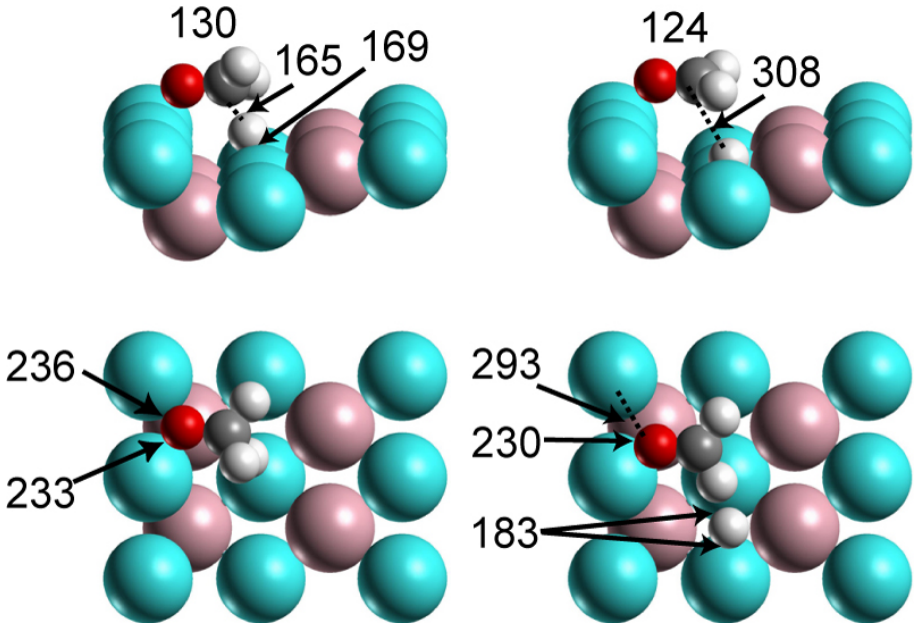

Figure 5.4. Side (upper panels) and top views (lower panels) of calculated TS (left) and FS (right) structures involved in C-H bond breaking of CH_3O on $(221)^{Pd}$ surface with dissociated H_a on the $(221)^{Pd}$ terrace. Selected bond-lengths are given in pm. Atomic spheres: blue – Pd, pink – Zn, red – O, dark gray – C, light gray – H.

angle of ~60º with the step (Fig. 5.5). The O atom is in a distorted edge-bridge position with O-Pd contacts of 232 and 266 pm. The C-O bond in TS^{edge} is almost as long as for the former route and in the TS on the PdZn(111) surface. The H_a atom is displaced towards an edge bridge site; H_a-Pd distances are 168 and 271 pm. The C-H_a bond in TS^{edge}, 172 pm, is 7 pm longer than that in TS^{terr}. After the TS^{edge} has been reached, the C-O bond is redirected to the lower terrace. In the FS, the C-O axis is almost perpendicular to the step edge (Fig. 5.5) and the O-Pd distances are stretched to 239 and 273 pm. H_a moves to the edge-bridge site and forms nearly equal H_a-Pd contacts of 178 and 174 pm. The calculated activation barrier for this path, 53 kJ mol^{-1} (Table 5.2), is again much lower than the barriers calculated on flat PdZn surfaces, and it is only slightly higher than the barrier for the pathway via TS^{terr}. Concomitantly, the rate constant at 300K, ~10^4 s^{-1}, is only several times smaller than for the first path, but dramatically higher than on the flat planes (Table 5.2). The reasons for lowering the activation barrier for C-H bond breaking on the $(221)^{Pd}$ surface compared to the flat surfaces will be discussed in Section 5.4.

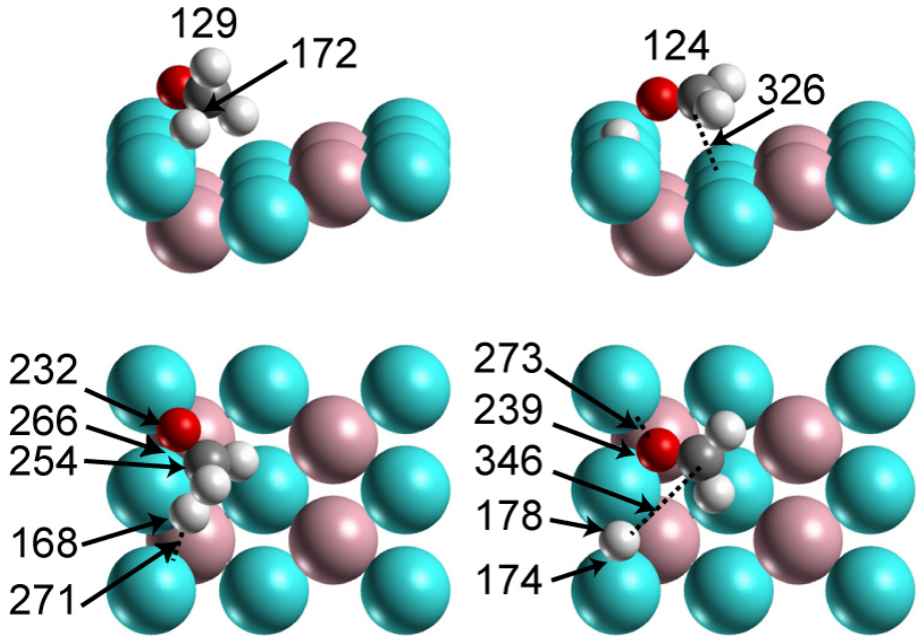

Figure 5.5. Side (upper panels) and top views (lower panels) of calculated TS (left) and FS (right) structures involved in C-H bond breaking of CH_3O on $(221)^{Pd}$ surface with dissociated H_a on the $(221)^{Pd}$ step. Selected bond-lengths are given in pm. Atomic spheres: blue – Pd, pink – Zn, red – O, dark gray – C, light gray – H.

TS on $(221)^{Zn}$

Not unexpectedly, the C-H bond breaking reaction on the $(221)^{Zn}$ surface at a Zn bridge (Fig. 5.6) features C-O bond tilting towards a terrace Pd atom. As this is a (111) terrace, the reaction proceeds similarly to that on the PdZn(111) surface, except that the oxygen center, instead of moving to a top Zn location, remains essentially at the Zn bridge site due to the strong O-Zn interaction here. Along the reaction path, the distance H_a-Pd decreases, manifesting a bonding interaction of these two atoms. In the TS, the activated C-H_a bond is stretched to 152 pm and the H_a-Pd contact extends to 173 pm; the O-Zn distances are 218 and 223 pm. In the FS, H_a moves to the Pd_2Zn site with H_a-Pd distances at 177 and 182 pm and H_a-Zn distance at 191 pm, while the O-Zn bonds are 210 and 212 pm. The present reaction profile is characterized by a large barrier of 108 kJ mol^{-1}, resulting in a negligible reaction rate (Table 5.2). The main reason for the higher barrier on $(221)^{Zn}$ is the enhanced interaction of the reactant CH_3O with the substrate. Therefore, this reaction route is not expected to play a significant role in the overall reaction mechanism of methoxide decomposition.

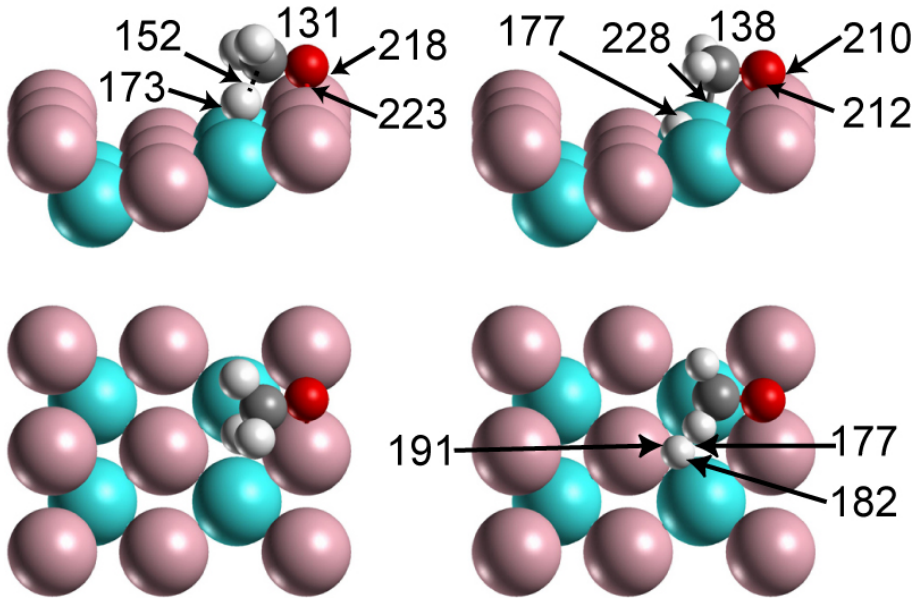

Figure 5.6. Side (upper panels) and top views (lower panels) of calculated TS (left) and FS (right) structures involved in C-H bond breaking of CH_3O on $(221)^{Zn}$ surface. Selected bond-lengths are given in pm. Atomic spheres: blue – Pd, pink – Zn, red – O, dark gray – C, light gray – H.

Table 5.4. Kinetic parameters[a] calculated for C-O bond breaking of CH_3O on stepped PdZn(221) surfaces in comparison with the analogous reactions on the flat surfaces PdZn(111) and PdZn(100).

Parameter	Sites on PdZn			
	$(221)^{Pd}$	$(221)^{Zn}$	(111)	(100)
E_a	199	220	198	158
A^0	8×10^{12}	4×10^{12}	1×10^{12}	2×10^{12}
κ	$\sim10^{-22}$	$\sim10^{-26}$	$\sim10^{-22}$	$\sim10^{-15}$

[a] Heats of reaction E_r (kJ mol^{-1}), activation energies E_a (kJ mol^{-1}) corrected for zero-points, pre-exponential factors A^0 (s^{-1}), and reaction rate constants κ (s^{-1}) at 300 K.

5.3.2 C-O Bond Cleavage

To reiterate, on flat PdZn surfaces methoxide decomposition via C-O bond cleavage was calculated notably less favorable than C-H bond breaking. As shown in Section 5.2, the C-O bond breaking process on PdZn(221) sites is even further disfavored thermodynamically with respect to the corresponding reaction on the planar (111) and (100) surfaces (Table 5.2). To examine whether the presence of steps on PdZn catalysts facilitates kinetically the breaking of the C-O bond, we located TS structures on the $(221)^{Pd}$ and $(221)^{Zn}$ surfaces and we quantified the activation barriers in Table 5.4.

TS with CH_3 on step-edge of $(221)^{Pd}$

In the TS, the leaving O atom approaches a Zn atom below the Pd step. Tilting the C-O bond initiates the reaction. Eventually the CH_3 group moves towards the top site on a step-edge Pd while the O atom is displaced to a Zn atom at the bottom of the step (Fig. 5.7). Compared to that in the IS, the O-Zn contact is shortened by 75 pm in the TS, whereas the C-O distance is stretched by ~60 pm to 206 pm, almost equals to that calculated on the (111) surface (see Table 3.3). In the FS, the O atom reaches the hollow site formed by one bottom Zn atom and two edge Pd atoms; see selected distances in Figs. 5.3a and 5.7. The calculated activation energy is 199 kJ mol^{-1} (Table 5.4). This barrier is almost equal to that on the (111) surface which yielded a very low rate constant and similar structural motifs of the transformation. Recall that the corresponding barrier on the (100) surface is ~40 kJ mol^{-1} lower. C-O bond

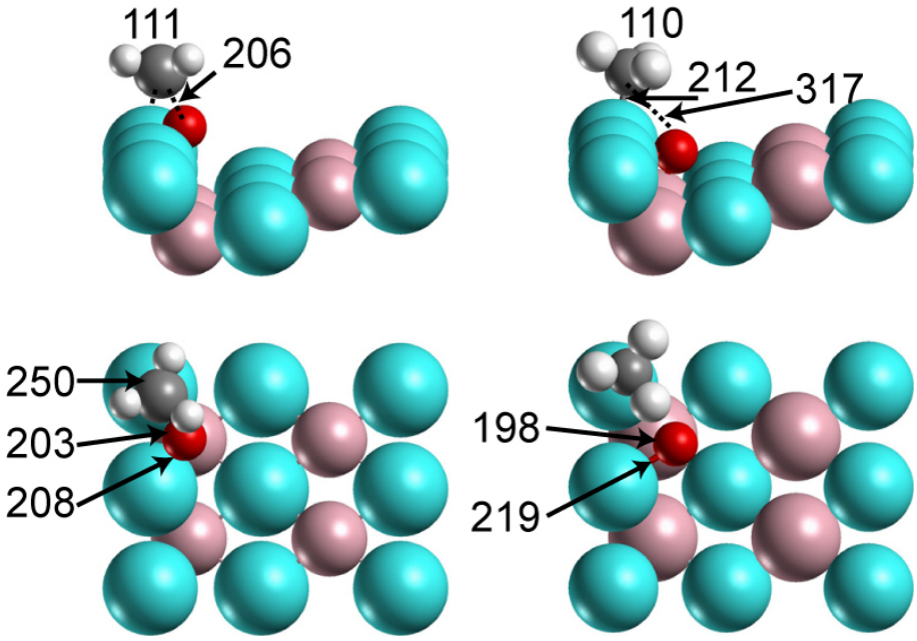

Figure 5.7. Side (upper panels) and top views (lower panels) of calculated TS (left) and FS (right) structures involved in the lowest-barrier route of C-O bond breaking of CH_3O on the PdZn surface $(221)^{Pd}$. Selected bond-lengths are given in pm. Atomic spheres: blue – Pd, pink – Zn, red – O, dark gray – C, light gray – H.

breaking was calculated somewhat more endothermic because the bonding of O to the $(221)^{Pd}$ substrate is weaker than on the (111) and (100) surfaces (Table 5.2).

5.4 Analysis of Alterations of the Barrier Height

The calculated activation energies for C-H bond splitting of methoxide on the (111) and (100) surfaces of PdZn are rather close to each other and reflect the low reactivity of these substrates (Table 5.3). In view of this similarity, we have chosen the (111) surface as reference for our attempt to rationalize why the activation energy for C-H scission on the $(221)^{Pd}$ surface is more than 40 kJ mol^{-1} smaller than on the (111) surface, while the activation energy of C-O scission is not lowered.

In general, the activation barrier of a reaction over various kinds of substrates may change because the (total) energies of the reactant(s) or the TS complex vary. In case of a decomposition reaction AB → A + B, the second contribution can be approximated in terms of the interaction energies of the product species A and B with the substrate, taken in the

geometry of the TS complex. A similar TS analysis has been performed for instance in Ref. 115 for nitric oxide dissociation. In the following we will explore this situation in more detail.

Relative to the activation energy calculated for PdZn(111), the reaction barrier of C-H scission on $(221)^{Pd}$ is 44 kJ mol^{-1} lower via TS^{terr} and 40 kJ mol^{-1} lower via TS^{edge} (Table 5.3). As measured by the adsorption energy, on the $(221)^{Pd}$ surface of PdZn, the energy of the reactant CH_3O is raised 17 kJ mol^{-1} above the energy on the PdZn(111) surface (Table 5.1). In other words, the activation energy is lowered by 17 kJ mol^{-1} because the reactant interacts weaker with the $(221)^{Pd}$ surface than with the (111) surface. The product fragment CH_2O, fixed in the TS^{terr} and TS^{edge} geometries, interacts 32 and 51 kJ mol^{-1} more strongly with the substrate than in the TS structure on the (111) substrate. The corresponding values for H species imply weaker interaction energies by 8 and 15 kJ mol^{-1}. Accordingly, one expects a total lowering of the activation barrier by 24 kJ mol^{-1} (TS^{terr}) or 36 kJ mol^{-1} (TS^{edge}) due to the changes in the interactions of the products CH_2O and H with the substrate. In the gas phase, the TS fragments, fixed in their TS structure of the corresponding adsorption complex, interact 7 kJ mol^{-1} stronger (TS^{terr}) and 9 kJ mol^{-1} weaker (TS^{edge}) than in the (111) surface TS. Together with the absorbate-substrate interaction and the IS contribution of 17 kJ mol^{-1}, one estimates a total lowering of the barrier height on $(221)^{Pd}$ over that on the (111) surface by 48 kJ mol^{-1} (TS^{terr}) or 44 kJ mol^{-1} (TS^{edge}). These approximate values are indeed quite close to the results calculated for TS^{terr}, 44 mol^{-1}, and TS^{edge}, 40 mol^{-1} (Table 5.3). Phrased differently, the enhanced (total) stabilization of the products contributes about twice as much to the lowering of the activation barrier than the weaker interaction of the reactants

A similar analysis of C-O bond scission on the $(221)^{Pd}$ surface in comparison with the barrier on the surface PdZn(111) assigns the largest unfavorable contribution to the O atom, e.g. -78 kJ mol^{-1} in the TS. This change reflects the weaker O-substrate interaction at $(221)^{Pd}$ surface compared to (111) surface. In the TS, the other product species, CH_3, contributes 18 kJ mol^{-1} to a lower relative barrier height, so that the combined product effect is an *increase* of the $(221)^{Pd}$ barrier relative to that of the (111) substrate by (78–18) kJ mol^{-1} = 60 kJ mol^{-1}. The gas phase correction of this estimate is very small: the TS structure is 1 kJ mol^{-1} higher in energy than the (111) surface TS. In combination with the favorable initial state effect, 17 kJ mol^{-1} (see above), and absorbate-substrate interaction, one estimates the activation barrier on $(221)^{Pd}$ 44 kJ mol^{-1} higher than on PdZn(111). The discrepancy between estimated and calculated change of the barrier height may be traced back to bond competition [107]. Indeed,

the bond distance of O in TS to the shared Pd atom, 203 pm (Fig. 5.7), is notably shorter than the value 238 pm calculated for the TS on (111) surface.

5.5 Conclusions

In this chapter we described slab-model DF investigations on the decomposition of methoxide at PdZn(221) surfaces featuring Pd or Zn steps. The most favorable adsorption complexes involve step-edge atoms, consistent with the higher reactivity of low-coordinated atoms forming a step. The binding energies on stepped $(221)^{Pd}$ and $(221)^{Zn}$ substrate models exhibit an obvious trend: species preferring Pd-dominated sites feature the strongest binding on $(221)^{Pd}$, while for adsorbates favoring Zn-dominated sites the adsorption interaction is the strongest on $(221)^{Zn}$ slab.

Compared to the flat PdZn surfaces discussed in Chapters 3 and 4, the activation energies for C-H and C-O bond cleavage on the $(221)^{Zn}$ surface do not decrease, even though methoxide interacts stronger with the substrate at the Zn step edge. On the other hand, the reaction barrier for C-H bond breaking on the $(221)^{Pd}$ surface is greatly reduced, to ~50 kJ mol^{-1} from ~90 kJ mol^{-1} on flat surfaces. This crucial activation barrier is reduced for two synergetic reasons: the reactant CH_3O interacts weaker with the catalyst while the product CH_2O binds stronger to the substrate. Concomitantly, the calculated reaction rate constant for C-H cleavage is increased by a factor of 10^8, reaching ~10^4–10^5 s^{-1} at 300 K.

Finally, we would like to mention that our calculated C-H bond breaking activation barriers on PdZn(111), PdZn(100), PdZn(221) and Cu(111) surfaces are in fair agreement (to be taken with great care) to the reported apparent activation barrier of 95 kJ mol^{-1} on Pd/ZnO catalyst using a power law expression [116] and those on various commercial Cu/ZnO based catalysts, which range from 74 to 122 kJ mol^{-1}, using various power-law and Langmuir-Hinselwood rate expression [18]. Usually the experimental values reflect other factors such as diffusion, mass transfer, etc. and therefore they depend strongly on the temperature and pressure in which they have been determined [117].This agreement between calculated and experimental values for activation barriers can be take to imply that methoxide C-H bond breaking is the rate determining step of methanol steam reforming on Cu and PdZn alloy catalysts is likely correct. From our calculations on different surfaces on PdZn catalysts (remember that in Chapter 3 it was shown that the reactivity of PdZn alloy is similar to Cu), it

can be deduced that the wide range of reported apparent activation barriers for different Cu-based catalysts is an indication of the degree of defects present on various commercial catalysts. This once again illustrates the structural complexity of “real” catalysts used in the industrial scale.

Chapter 6

Dehydrogenation of Formaldehyde on Pd(111), Cu(111) and PdZn(111)

Fuel cells currently used in vehicles are very sensitive to poisons, especially to carbon monoxide, which even at low concentration (ppm) has a detrimental effect on the performance of a fuel cell [19]. Recent experiments showed that dehydrogenation of formaldehyde and methanol over monometallic Pd and PdZn leads to similar products. On Pd, carbon monoxide and hydrogen are formed and, on PdZn alloy, methyl formate, hydrogen and a small amount of carbon monoxide (< 5%) [5]. Likewise, under experimental conditions of steam reforming, replacing methanol with formaldehyde yields mainly carbon dioxide and hydrogen on PdZn alloy catalyst, just as for methanol reforming [5]. Recent MSR experiments revealed [20] that the water gas shift reaction (Fig. 1.1, reaction 8) and its reverse (Fig. 1.1, reaction -8) are negligibly slow on PdZn alloy catalysts to convert carbon dioxide to carbon monoxide and vice versa. Therefore, the observed production of carbon monoxide (< 5%) has been assigned to the direct decomposition of methanol, occurring in parallel to MSR reaction [20].

In Chapters 3 to 5, we have examined surfaces of various catalysts to understand their reactivity and to ascertain C-H bond breaking as the rate determining step of MSR. In Chapter 5, we found that the $(221)^{Pd}$ surface features the lowest activation barrier for C-H bond breaking on PdZn catalyst; nevertheless, the regular (111) surface has also provided useful insight into the differences between methoxide C-H and C-O bond cleavage reactions on substrates. In this chapter, we will consider the (111) surfaces of Pd, Cu and PdZn alloy to study formaldehyde dehydrogenation (Fig. 1.1, reactions 4 and 5), to elucidate similarities and differences in the reaction mechanisms on these three substrates. This study will give some indications helpful for preparing a better catalyst with low carbon monoxide

output by providing insights, why carbon monoxide is commonly not produced (or produced only in a very small amount) during methanol dehydrogenation on the PdZn and Cu based catalysts.

In the following, we will employ the same computational models and procedures as in Chapter 3. We will begin with a discussion of how the intermediate formyl (HCO) adsorbs on the three substrates. Then we will proceed to study formaldehyde dehydrogenation, first to formyl (Fig. 1.1, reaction 4) and further on to carbon monoxide (reaction 5).

6.1 Adsorption of Formyl

Table 6.1 shows pertinent structural parameters and binding energies of formyl on the (111) surfaces of Pd, Cu and PdZn. In cluster model calculations at the BP level, hollow sites were found to be favored on Pd(111) with a binding energy of 340 kJ mol^{-1} [97], while GGA-PW91 periodic slab model calculations by the same group reported a binding energy of 237 kJ mol^{-1} [99].The difference in binding energy between slab model and cluster model calculations has been attributed to cluster size effects [99]. Our calculated binding energy of 210 kJ mol^{-1} at the fcc site agrees better with the results of the previous periodic slab model calculation. The discrepancy of the energies from the two periodic slab model calculations most likely is due to the fact that as always we used a 4-layer model compared to the 3-layer model of the previous study [99].

Inspection of Table 6.1 reveals that formyl does not exhibit a strong site preference on the Pd(111) surface. It binds to the surface in a η^1(C) configuration; the distance r(O-Pd) = 288 pm at the fcc site implies a minimum interaction between O and Pd atoms. For the top-bridge-top (tbt) configuration which is similar to the fcc site, we started from a η^2(C,O) configuration, but after geometry optimization obtained an η^1(C) bridge configuration with very similar characteristics as in the top configuration: r(C-Pd) = 196 pm, r(O-Pd) = 289 pm (Table 6.1). The top site was determined to be slightly more preferred over the other two sites studied, BE = 214 kJ mol^{-1}. The different site preference compared to the previous slab model study [99] is most likely related to the very flat nature of the potential energy surface of formyl on Pd(111); binding energy differences are less than 15 kJ mol^{-1}. A similar situation has been reported on the Pt(111) surface where both the top configuration (BE =

228 kJ mol^{-1}) [108] and the fcc configuration (BE = 237 kJ mol^{-1}) [99] have been claimed as the most stable adsorption complexes in separate studies, employing the same slab thickness (3 layers) and the same exchange-correlation functional PW91. The well-known case of CO/Pt(111) comes to mind, where DFT model results, CO at η^3 position, appear to misrepresent the experimental situation, CO at top site [118,119], where small effects make a difference to the predicted structure.

Similar to Pd(111), we found that formyl shows essentially no preference for binding sites on the Cu(111) surface (Table 6.1); the binding energy of ~125 kJ mol^{-1} at all sites studied. Earlier cluster model calculations had identified the bridge site as most favored on Cu(111), with binding energy of 140 kJ mol^{-1}, while hollow sites were characterized by a binding energy of ~110 kJ mol^{-1} [120]. However, this preference of the bridge site is likely a cluster artifact, similar to the case on the Pd(111) surface. In fact, just as in the present study, recent calculations also based on periodic slab models [72] had furnished essentially degenerate η^2(C,O) tbt and η^1(C) hollow configurations, with binding energies of ~110 kJ mol^{-1}. According to the present work, the fcc site is slightly more favorable on Cu(111), in contrast to Pd(111). This difference is due to the different nature of formyl interactions with

Table 6.1. Calculated characteristics[a] of adsorption complexes of HCO on the (111) surfaces of Pd, Cu and PdZn.

	Pd			Cu			PdZn			
	top	tbt[b]	fcc	top	tbt[b]	fcc	top^{Pd}	tbt	fcc^{Pd2Zn}	fcc^{PdZn2}
C-O	120	119	123	121	120	122	121	125	126	123
C-M[c]	199	196, 261	211	201	203, 229	215	210[d]	205[d]	222, 222[d]	206[d]
O-M[c]	288	289	286	274	274	280	301[d]	225[e]	218[e]	276, 276[e]
Z(C)	198	176	157	200	173	156	210	188	164	192
BE	214	200	210	124	121	127	158	167	153	160

[a] Binding energy BE, bond distances C-O, C-M, O-M (M is a substrate metal atom), and height z(C) of C from top crystal plane. Energies in kJ mol^{-1}, distances in pm.

[b] Initial starting geometry is η^2(C,O), which after optimization becomes η^1(C).

[c] When X (X = C, O) is bound to two substrate atoms M, two values X-M are given.

[d] M = Pd

[e] M = Zn

Cu (s metal) and Pd (d metal), similar to the case of methyl adsorption (see Section 3.2.5). In fact, it has been shown [94] that the 2σ molecular orbital of CH_3 interacts with a transition metal substrate (M) and that this 2σ-d(M) bonding results in the preference of on-top sites, whereas 2σ-s(M) favors adsorption complexes at hollow sites.

From Chapter 3 we recall that on PdZn alloy the adsorbed species bound via a carbon atom prefer Pd sites, whereas oxygen-bound species prefer Zn sites. Formyl adsorption configurations on the (111) surfaces of Pd and Cu, leads one to hypothesize that formyl binds to the PdZn alloy surface mainly through the C atom in the η^1(C) configuration. This is indeed the case at the top^{Pd} and fcc^{PdZn2} sites. For the latter structure, we started the geometry optimization with a structure where O was bound to two Zn atoms. However, the optimized geometry exhibits a η^1(C) configuration; the O-Zn bond distance is 276 pm (Table 6.1). At the fcc^{Pd2Zn} site, the anticipated structure with C bound to two Pd atoms and O bound to a Zn atom was confirmed during optimization, but this adsorption complex is the least stable one. As judged by the bonding contacts, the C-Pd interaction (222 pm) here is weaker than in the formyl adsorption complexes studied where r(C-Pd) = ~210 pm. In contrast to the other two substrates, the tbt site on PdZn(111) features the highest binding energy, 167 kJ mol^{-1}, in the η^2(C, O) configuration (r(C-Pd) = 205 pm, r(O-Zn) = 225 pm).

In summary, the potential energy surface of formyl on all three substrates under scrutiny is rather flat, with binding energies varying less than 15 kJ mol^{-1} across all sites studied. Therefore, under reaction conditions one expects formyl to be very mobile on the surfaces. Of the three substrates, formyl binds the least strongly on Cu(111), ~125 kJ mol^{-1}, and the strongest on Pd(111), ~210 kJ mol^{-1}. The binding energy of formyl on PdZn(111) , ~160 kJ mol^{-1}, is calculated intermediate between those on Pd(111) and Cu(111), like for all other adsorbates considered in the previous chapters.

6.2 Dehydrogenation of Formaldehyde

As formaldehyde is weakly adsorbed and formyl showed essentially no preference for a particular adsorption site, we carried out a normal mode analysis of the adsorption structures of formaldehyde and formyl that were chosen as IS of dehydrogenation, thus ensuring that the initial states were at least *local* minima.

6.2.1 C-H Bond Breaking of Formaldehyde

The most stable adsorption configuration of formaldehyde (tbt) on the three substrates was chosen as IS for the dehydrogenation reaction. In the IS on Pd(111) (Fig. 6.1), the oxygen atom of CH_2O binds to the Pd atom at a distance of 211 pm, while carbon binds to the Pd with a distance of 215 pm. The C-O bond, 131 pm, is almost parallel to the (111) surface. In the FS, CHO + H_a on Pd(111), the formyl resides on top of a Pd atom [this is the most stable configuration of formyl on Pd(111)], and the hydrogen atom is located at a fcc site.

On the way to the TS of C-H bond breaking on Pd(111), the C-H_a bond (with H above C) rotates around the C-O axis and is stretched by moving the H_a atom towards a bridge site. The formyl moiety remains at the tbt site, with the C-Pd distance shortened and the O-Pd bond elongated and weakened. This, in turn, strengthens to some extent the C-O bond which shortens from 131 pm in the IS to 129 pm in the TS (Fig. 6.1). In the TS, the formyl moiety is located close to the tbt site. The shortest H-Pd distance is 183 pm. The distance C-Pd, 199 pm, is 16 pm shorter than in the IS. The C-H_a bond distance increased from 111 pm in the IS to 139 pm in the TS. Past the TS, the atom H_a retreats to the favorable fcc site. In the FS, formyl is situated near the on-top site of Pd with r(C-Pd) = 197 pm.

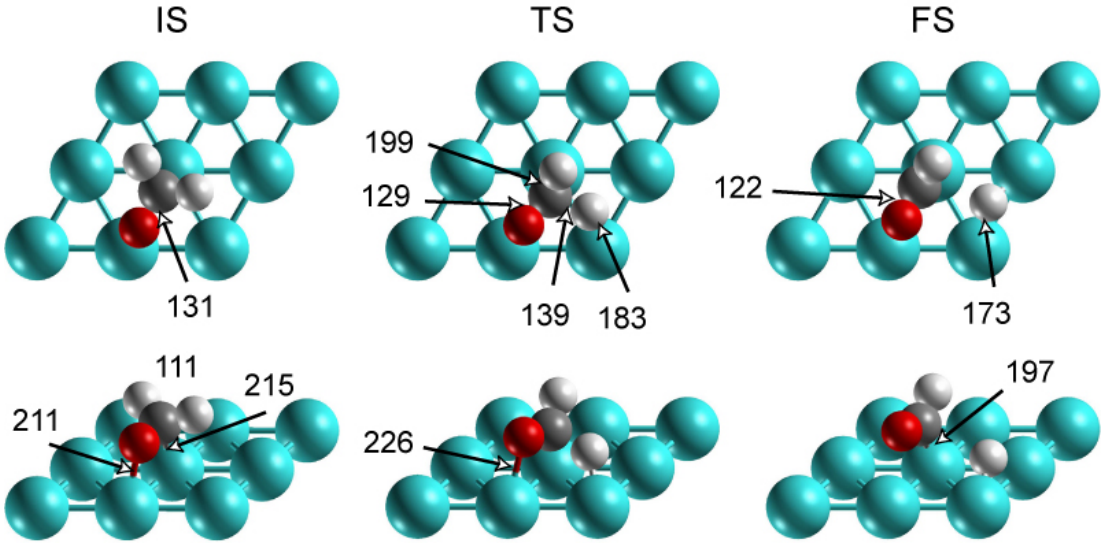

Figure 6.1. Top (above) and side views (below) of calculated IS, TS and FS structures of C-H bond breaking of formaldehyde on Pd(111). Selected bond lengths in pm. Atom labeling: blue – Pd, red – O, dark gray – C, gray – H.

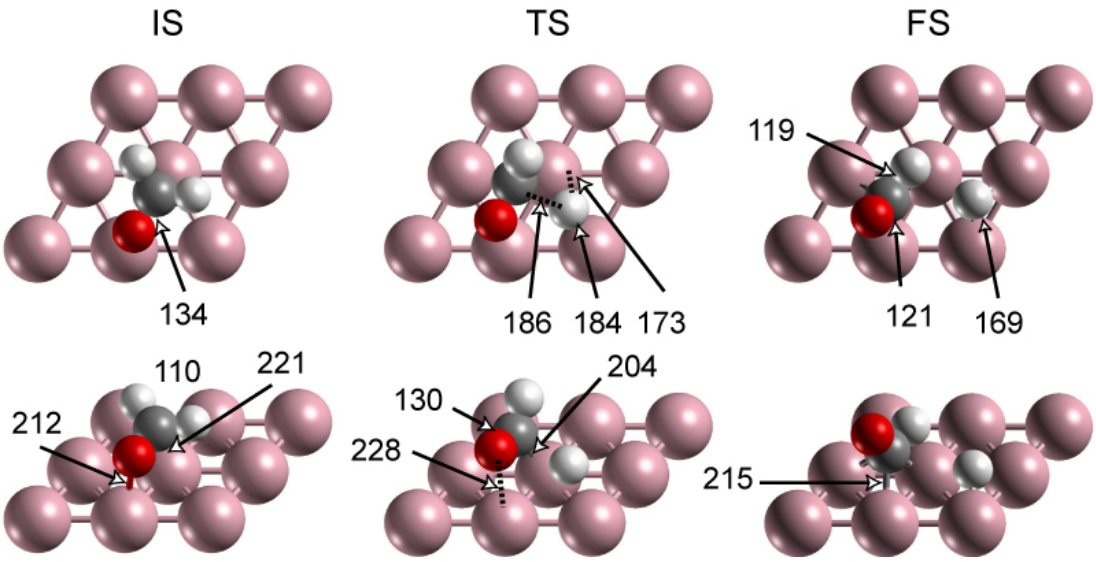

Figure 6.2. Top (above) and side views (below) of calculated IS, TS and FS structures of C-H bond breaking of formaldehyde on Cu(111). Selected bond lengths in pm. Atom labeling: pink – Cu, red – O, dark gray – C, gray – H.

The dehydrogenation of formaldehyde on Cu(111) occurs in a similar way and the shape of the TS structure resembles that on Pd(111), except that on Cu it is a late transition state with a significantly larger value of r(C-H_a) = 186 pm (Fig. 6.2). Other structural characteristics are quite similar: r(C-O) = 130 pm, r(C-Cu) = 204 pm, and r(H-Cu) = 184 pm. Another slight difference is that the formyl moiety favors the three-fold hollow site on

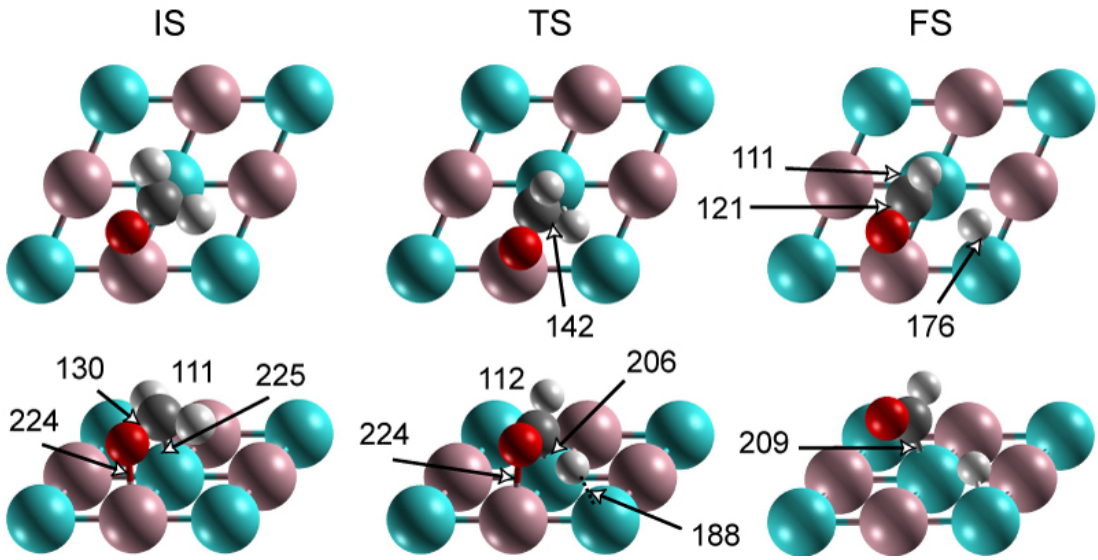

Figure 6.3. Top (above) and side views (below) of calculated IS, TS and FS structures of C-H bond breaking of formaldehyde on PdZn(111). Selected bond-lengths in pm. Atom labeling: blue – Pd, pink – Zn, red – O, dark gray – C, gray – H.

Cu(111), in contrast to the top site on Pd(111) (Fig. 6.1). Thus, the resulting formyl molecule moves from the tbt site in the TS to the hollow site in the FS.

The IS of formaldehyde dehydrogenation on PdZn(111) alloy is a top-bridge-top configuration with r(O-Zn) = 224 pm and r(C-Pd) = 225 pm. The C-H_a bond breaking process is rather similar to those on the (111) surfaces of Pd and Cu. The TS structure resembles that on Pd(111) with a C-H_a distance of 142 pm while r(C-Pd) = 206 pm and r(O-Zn) = 224 pm. In the FS, the formyl moiety is located at a top Pd site and the dissociated hydrogen atom is close to the fcc^{Pd2Zn} site (Fig. 6.3).

6.2.2 C-H Bond Breaking of Formyl

Because the potential energy surface of formyl is rather flat on all three substrates, we chose the top adsorption configuration on all three substrates as the IS for our comparative study of formyl dehydrogenation. This may lower the estimated activation energies on Cu(111) and PdZn (111) as the initial state is not the most stable site. However, we do not expect the differences to be large due to the flat character of the various potential energy surfaces. Moreover, this strategy allows a comparative study of analogous reaction paths across for the three substrates. In the FS, carbon monoxide resides at a fcc site on Pd(111) and Cu(111) and on top of a Pd atom at PdZn(111) as these are the most stable sites for CO on

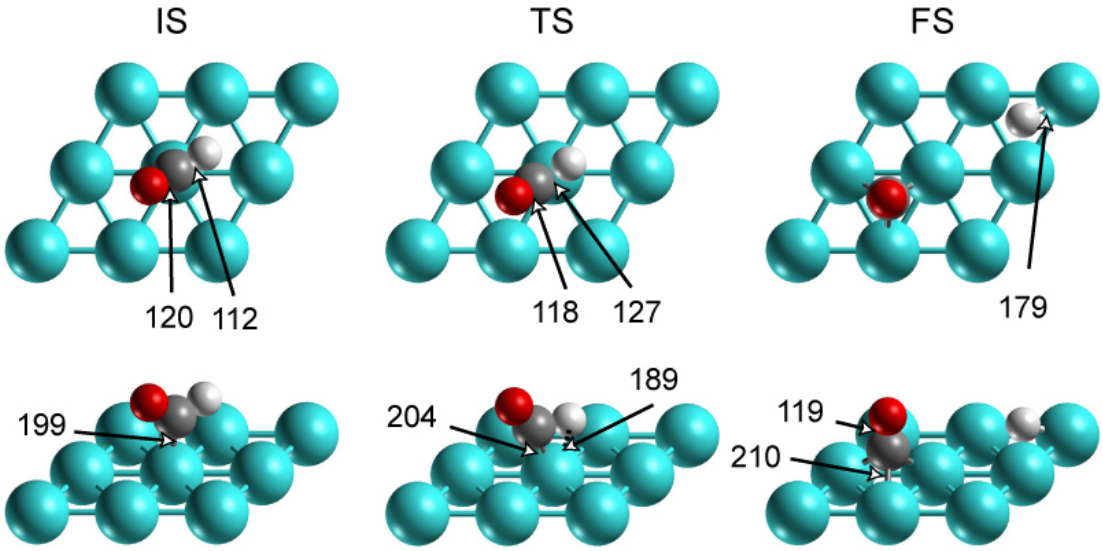

Figure 6.4. Top (above) and side views (below) of calculated IS, TS and FS structures of C-H bond breaking of formyl on Pd(111). Lay-out as in Figure 6.1.

these substrates (Section 3.2.4). In all three final states, the dissociated H atom resides at a fcc site remote from the carbon monoxide.

Hydrogen abstraction from formyl on Pd(111) starts with the IS moiety sliding from the top site to a fcc site. In the course of the reaction, the distance H-Pd decreases, manifesting a bonding interaction of these two atoms. In the TS (Fig. 6.4), the activated C-H bond, 127 pm, is elongated by 15 pm, the C-O bond distance is 118 pm and the C-Pd bond distance is 204 pm. In fact, CO and H "share" one Pd atom. Therefore, bonding competition exists [107] which pushes the H fragment away to another fcc site with r(H-Pd) = 179 pm. In the FS, the product CO resides in the fcc site with the C-O axis perpendicular to the surface, r(C-Pd) = 210 pm and r(C-O) = 119 pm.

Formyl dehydrogenation on Cu(111) is similar to that at Pd(111) (Fig. 6.5). In the TS, the C-H bond (137 pm) is activated by one Cu atom. The H atom is near a hcp site with r(H-Cu) = 181 pm and r(C-Cu) = 204 pm. In the FS, the atom H is located at a fcc site, with r(H-Cu) = 172 pm, while the CO moiety resides at another fcc site with r(C-Cu) = 207 pm and r(C-O) = 118 pm.

In contrast to Pd(111) and Cu(111), C-H bond scission of formyl on PdZn(111) begins with an inclination of the formyl moiety, with the H pointing towards another Pd atom, at a somewhat larger distance from the original adsorption site (Fig. 6.6). That H-Pd distance shrinks to 211 pm in the TS (Fig. 6.6), indicating the beginning of a bonding interaction. In

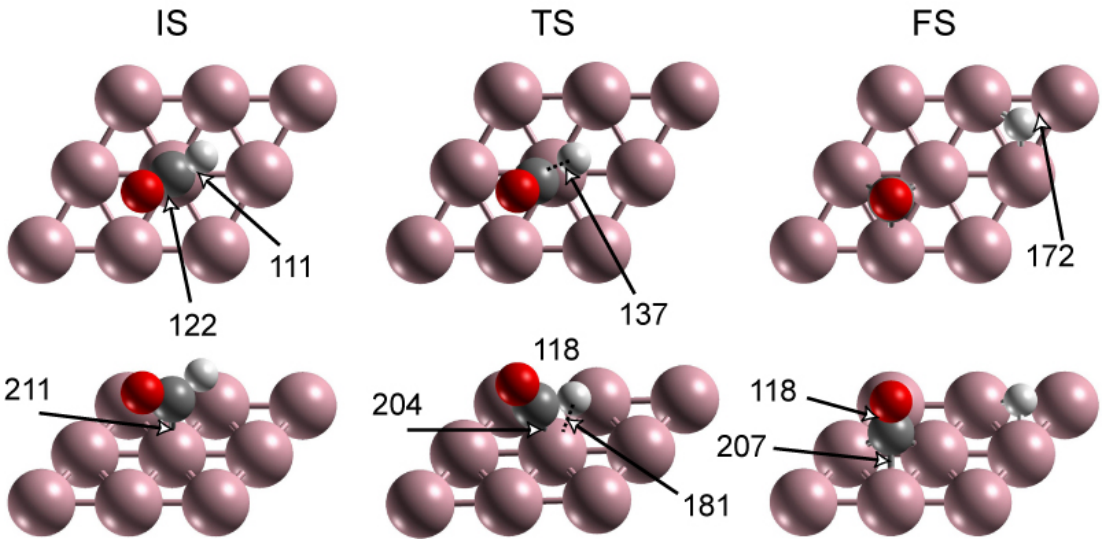

Figure 6.5. Top (above) and side views (below) of calculated IS, TS and FS structures of C-H bond breaking of formyl on Cu(111). Lay-out as in Figure 6.2.

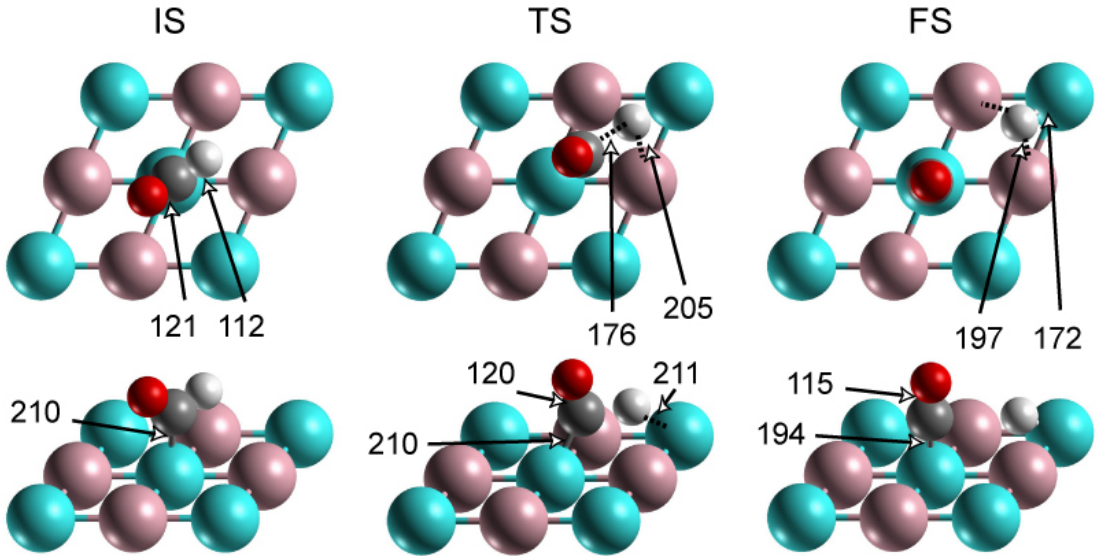

Figure 6.6. Top (above) and side views (below) of calculated IS, TS and FS structures of C-H bond breaking of formyl on PdZn(111). Lay-out as in Figure 6.3.

the TS on PdZn(111), the C-H distance is stretched rather far, to 176 pm, while the CO moiety is almost at a top site with r(C-O) = 120 pm and r(C-Pd) = 210 pm. Once the C-H bond is broken, the H atom moves to a fcc^{Pd2Zn} hollow site with r(H-Pd) = 172 pm and r(H-Zn) = 197 pm in the FS. CO stays at the top Pd site with the C-O axis perpendicular to the surface with r(C-Pd) = 194 pm and r(C-O) = 115 pm.

In comparison, the TS structures of hydrogen abstraction on the three substrates are rather similar, mainly due to the similar adsorption mode of the IS (recall that formaldehyde prefers tbt configuration on all three substrates). The products, formyl practically shows no preferences for an adsorption site and hydrogen atom always preferring hollow sites.

6.3 Reaction and Activation Energies of Formaldehyde Dehydrogenation

Table 6.2 and Fig. 6.7 display the kinetic and thermodynamic data calculated for formaldehyde dehydrogenation on Pd(111) and Cu(111) metals and on PdZn(111) alloy. Formaldehyde in the gas phase plus a clean substrate was chosen as energy reference in Fig. 6.7. Accounting for zero-point energies is expected to reduce the activation barrier of a bond breaking reaction because in the transition state one vibrational mode of the initial state has vanished. We calculated zero-point corrections to lower the activation energies by up to 19 kJ mol^{-1} (Table 6.2), mainly because a stiff C-H vibrational mode of the IS, ~2800 cm^{-1}, is lacking in the TS.

H abstraction from formaldehyde on the Pd(111) surface is calculated exothermic by 56 kJ mol^{-1}, in perfect agreement with the previously reported PW91 value of 55 kJ mol^{-1} [99]. However, on the Cu(111) surface, the analogous reaction is endothermic by 36 kJ mol^{-1} (previously reported at 54 kJ mol^{-1} [72]). Note that desorption of formaldehyde (BE = 11 kJ mol^{-1}) from this surface is energetically less demanding than H abstraction. Over the PdZn(111) surface, hydrogen abstraction from formaldehyde is essentially thermoneutral (-4 kJ mol^{-1}).

Table 6.2. Activation energy[a] E_a and reaction energy E_r[b] of formaldehyde dehydrogenation on the (111) surfaces of Pd, Cu and PdZn. Energies in , kJ mol^{-1}.

	E_a			E_r		
	Pd	Cu	PdZn	Pd	Cu	PdZn
$CH_2O \rightarrow CHO + H$	38 (22)	80 (63)	78 (64)	-56 (-65)	36 (25)	-4 (-18)
$CHO \rightarrow CO + H$	60 (41)	31 (16)	44 (25)	-132 (-141)	-86 (-93)	-71 (-80)

[a] Values in parentheses corrected for zero point energy.

[b] The heat of reaction is calculated as $E_r = \Sigma E_P - \Sigma E_R - \Sigma BE_P + \Sigma BE_R$, where ΣE_P and ΣE_R are sums of the total energies E of products (P) and reactants (R), respectively, in the gas phase. ΣBE_P and ΣBE_R are sums of the (adsorbate-substrate) binding energies BE of isolated product and reactant species, respectively. A positive value of E_r characterizes an endothermic reaction.

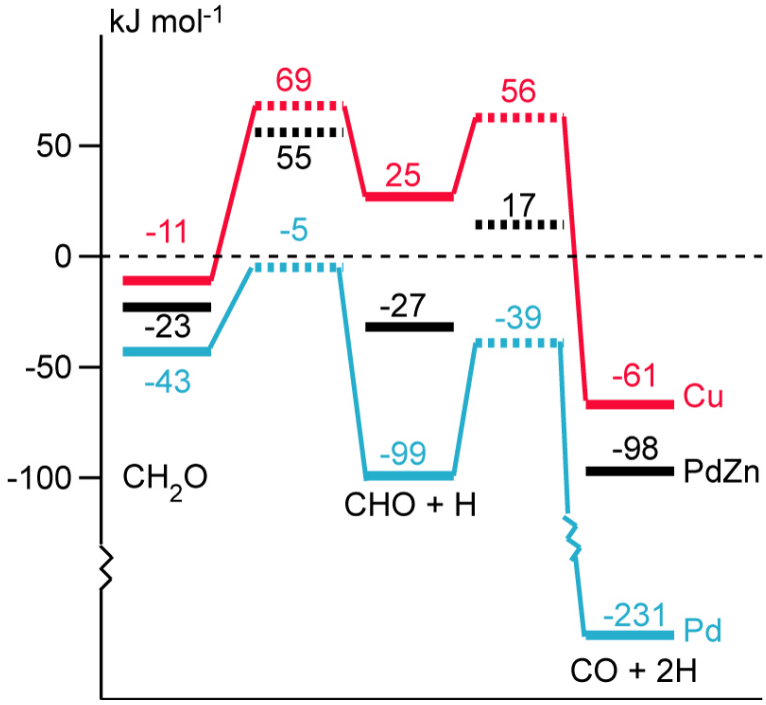

Figure 6.7. Calculated energetics (kJ mol^{-1}) of formaldehyde dehydrogenation on (111) surfaces of Pd, Cu and PdZn. Formaldehyde in the gas phase and a clean substrate are chosen as energy reference. Dashed lines mark transition states, without zero point energy corrections.

The activation energy for H abstraction from formaldehyde on Pd(111) was calculated at 38 kJ mol^{-1} (Table 6.2, Fig. 6.7), compared to ~10 kJ mol^{-1} calculated for Pt(111) [108]. As H abstraction from formaldehyde on Cu(111) is more endothermic than formaldehyde desorption, the former process would not need to be considered. Nevertheless, we have computed the activation barrier of formaldehyde dehydrogenation on Cu(111) for comparison with the analogous process on PdZn and for gaining insight into an elementary step of methanol synthesis on Cu(111). The calculated activation barrier of formaldehyde dehydrogenation on Cu(111), 80 kJ mol^{-1}, is essentially the same as that on PdZn(111), 78 kJ mol^{-1}. On the PdZn(111) surface, the activation barrier is about twice as high as on Pd(111), 38 kJ mol^{-1}, indicating that hydrogen abstraction is much slower on PdZn(111) than on Pd(111). With zero-point energy correction, the activation energy on Pd(111) is reduced to 22 kJ mol^{-1}, while on PdZn(111) it remains substantial, 64 kJ mol^{-1}. Note that activation energy, even after zero-energy correction, is higher than the binding energy of formaldehyde on PdZn(111). In other words, formaldehyde is kinetically inclined to desorb from the PdZn(111) surface rather than to undergo dehydrogenation.

According to our calculations, formyl dehydrogenation is exothermic on all three substrates under study. The reaction energy on Pd(111) is calculated at -132 kJ mol^{-1} compared to a DF value of -100 kJ mol^{-1} previously reported [99]. On Cu(111), the reaction is exothermic, -86 kJ mol^{-1}, to be compared with the published theoretical value of -67 kJ mol^{-1} [72]. Recall that these older results for Pd(111) and Cu(111) had been obtained for 3-layer substrate models [72,99] whereas in the present study 4-layer models were used throughout. On the PdZn(111) surface, the reaction energy of -71 kJ mol^{-1} is close to that computed on Cu(111), -86 kJ mol^{-1}.

We calculated rather low activation energies of formyl dehydrogenation on Pd(111), Cu(111), and PdZn(111), namely 60, 31, and 44 kJ mol^{-1}, respectively. These can be compared to values obtained with cluster models of Pd(111), ranging from 18 to 90 kJ mol^{-1} for different transition states [97], and to a value of 17 kJ mol^{-1} from a slab model study on Cu(111) [72]. The activation energies calculated in the present work become even more favorable after a zero-point energy correction, reflecting the strongly exothermic character of formyl dehydrogenation. Therefore, on the surfaces studied, our calculated results predict formyl to be unstable with respect to its dehydrogenation to carbon monoxide and hydrogen. This is in accord with the absence of experimental data in the literature on adsorbed formyl on these surfaces as it would be difficult to detect such an unstable species.

Our calculations showed that dehydrogenation of formaldehyde on Pd(111) is both thermodynamically and kinetically favorable, in agreement with the experimental observation that methoxide decomposes to carbon monoxide on Pd(111) surface [9]. On the Cu(111) surface, dehydrogenation of formaldehyde to formyl is kinetically unfavorable compared to the desorption of formaldehyde. This is in line with experimental evidence that methoxide partially decomposes to formaldehyde, but not to carbon monoxide [9]. However, the overall formaldehyde dehydrogenation reaction is computed to be exothermic on all three substrates and hence it is possible to obtain CO under thermal equilibrium conditions.

During methanol dehydrogenation on Pd/ZnO (PdZn alloy) catalysts, a small amount of carbon monoxide is produced (<5%) [20]. This small amount of CO is expected as our calculations for PdZn(111) have shown that the overall formaldehyde dehydrogenation reaction is exothermic. (When advancing this argument and those to follow in this paragraph, we implicitly assume that our results for the catalyst model PdZn(111) also hold for the real catalyst used in the experiment.) However, the formation of CO may be due to other reasons

because our calculations on the PdZn(111) surface also indicate that formaldehyde dehydrogenation is kinetically unfavorable (E_a = 78 kJ mol^{-1}) compared to formaldehyde desorption (BE = 23 kJ mol^{-1}). First note that, according to our calculations, formaldehyde decomposes to CO on metallic Pd sites. Indeed, Pd particles may be present on the "real" catalyst, i.e. some Pd may not have been converted to PdZn alloy [121]. Thus, care must be taken to ensure that alloying is completed during catalyst preparation to prevent formaldehyde dehydrogenation. Second, the "real" catalyst exhibits defect sites, e.g. steps or edges, at which formaldehyde may decompose. In Section 5.3.1, we found that, compared to PdZn(111) terraces, steps of PdZn(221) exposing Pd atoms stabilize formaldehyde, and, at the same time, lower the barrier for C-H bond breaking of methoxide. Therefore, with increased binding energy and the expected lower activation barrier for H-abstraction from formaldehyde, formaldehyde decomposition may become kinetically comparable or even favorable. This second alternative for CO production on PdZn catalysts merits further computational studies, which are beyond the scope of this thesis.

The above two situations are in agreement with the experimental observation that a high selectivity to CO_2 is achieved with 5–37.5% Pd loading of a ZnO support used for oxidative methanol steam reforming (MSR with oxygen) and a high selectivity to CO is observed if the Pd loading is outside this range [121]. One can expect that at high Pd loading, not all metallic Pd will be converted to PdZn alloy. Also, at low Pd loading, the PdZn alloy crystallite size is small (~20 nm) and hence catalysts may contain more defect sites (e.g. steps or edges) which may speed up formaldehyde dehydrogenation. Because carbon monoxide is an undesirable side product, it is important to optimize the Pd loading on the ZnO catalyst to ensure that formaldehyde dehydrogenation reaction is suppressed on the Pd/ZnO catalyst for methanol steam reforming.

Finally, we would like to briefly discuss implications of our results for the initial steps of methanol synthesis. A mixture of carbon monoxide (5%), carbon dioxide (5%), and hydrogen (90%) is a common feed stock for methanol synthesis in industry [122]. Recently, Iwasa et al. [123] reported that hydrogenation of carbon monoxide over Pd/ZnO (PdZn alloy) and Pd catalysts does not produce methanol – in contrast to the hydrogenation of carbon dioxide on Pd/ZnO and Cu/ZnO catalysts. Note that, on all three substrates studied, the hydrogenation of carbon monoxide to formyl is endothermic (> 70 kJ mol^{-1}) and associated with a high activation energy of at least 100 kJ mol^{-1} (Fig. 6.7). Even when formyl is formed on the surface of the catalyst, dehydrogenation is calculated kinetically and thermodynamically more

favorable than further hydrogenation of formyl to formaldehyde. These computational results agree with experimental observations that methanol is not formed on the Pd and Pd/ZnO catalysts during CO hydrogenation [123]. In this context, experimental findings come to mind where, methanol synthesis – as a reverse MSR reaction – has been found to occur on Cu [122] and PdZn [123] catalysts via hydrogenation of CO_2.

6.4 Conclusions

In this chapter, we presented a comparative periodic slab model study on formyl adsorption on planar Pd(111), Cu(111) and PdZn(111) surfaces. Formyl binds the least strongly at the Cu(111) surface (BE = ~125 kJ mol^{-1}) and strongest at Pd(111) (BE = ~210 kJ mol^{-1}). The binding energy of formyl on PdZn(111), as found in this work for all other adsorbates studied, is intermediate between those on Pd and Cu, ~160 kJ mol^{-1}. All three potential energy surfaces of formyl adsorption were judged to be rather flat, with binding energies at the various sites varying less than 15 kJ mol^{-1}; this implies easy diffusion of formyl on the (111) surfaces of Pd, Cu, and PdZn..

We characterized computationally both the thermodynamics and the kinetics of formaldehyde and formyl dehydrogenation on these surfaces. Calculated activation energies show that dehydrogenation of formaldehyde is favorable on Pd(111), but unfavorable on the (111) surfaces of Cu and PdZn alloy. We rationalized the experimentally observed formation of carbon monoxide on PdZn alloy by formaldehyde dehydrogenation at monometallic Pd sites. Optimization of Pd loading on ZnO catalyst appears to be required to ensure that during methanol steam reforming on the Pd/ZnO catalyst the amount of carbon monoxide produced is minimized.

We also discussed implications of our results on carbon monoxide hydrogenation to methanol. The initial step of this reaction is both kinetically and thermodynamically unfavorable on the three substrates studied, in agreement with experimental evidences that methanol is not formed on Pd and Pd/ZnO catalysts during hydrogenation of CO [123].

Chapter 7

Thermodynamic Study of H_2O and Related Species on PdZn(111) and Cu(111) Surfaces

To understand the full reaction mechanism of MSR, in particular, one needs to establish how H_2O modifies the surface composition of the catalyst, as H_2O or related species adsorbed on the surface may change the outcome of the methanol reaction on Cu and PdZn based catalysts. Therefore, it is necessary to clarify whether, under MSR reaction conditions, H_2O adsorbs and remains intact or decomposes to surface hydroxyl or atomic oxygen on the catalyst surface. There is no experimental evidence of H_2O dissociation on the clean Pd(111) and Pt(111) surfaces, whereas controversial reports have been published regarding H_2O adsorption on the clean Cu(111) surface. In a recent review article [27], H_2O was claimed to dissociate on the clean Cu(111) surface [28], whereas in another study [29] dissociation was not observed. The observed dissociation of H_2O on the clean Cu(111) surface [28] may likely have been caused by oxygen impurities [30]. DF calculations predict H_2O dissociation on defect-free Cu(111) to be energy-neutral (-1 kJ mol^{-1}), but endothermic (68 kJ mol^{-1}) on the ideal Pt(111) surface [33]. In the presence of surface oxygen, H_2O dissociation to surface bound hydroxyl was calculated to be more favorable thermodynamically, with reaction energies of -47 kJ mol^{-1} and 42 kJ mol^{-1} on Cu(111) and Pt(111), respectively [33].

Strictly speaking, results of electronic structure theory alone are valid only at zero temperature and zero pressure conditions. Therefore, care is necessary when invoking them in typical high-pressure applications, such as catalysis. In this chapter, we would like to use the data from DF calculations to calculate appropriate thermodynamic potentials, such as the Gibbs free energy of adsorption, which can be minimized as a function of various

environmental variables. In this way the predictive power of *ab initio* techniques can be extended to more realistic temperature and pressure ranges. For the Cu(111) and PdZn(111) surfaces, we will screen a number of possibly relevant surface structures that can be expected in contact with the gas phase H_2O (containing trace amounts of H_2 and O_2) and we shall evaluate which of them turns out to be most stable under a range of temperature and partial pressures conditions.

We note in passing that such a transition from a micro- to a mesocopic system description is rigorously applicable only to systems in equilibrium or in a metastable state, which is considered to be rapidly achieved at moderate to high temperatures, relevant to the following discussion. For a chemical reaction, e.g. CO oxidation [124], a so-called "constrained equilibrium" is assumed. That is, adsorption-desorption processes are much faster than the chemical reaction between the adsorbed species [124]. Thus the species on the surface are considered to be close to equilibrium with the reactants in the gas phase.

Explicit consideration of the surrounding gas phase in terms of "*ab initio* atomistic thermodynamics", i.e. using approaches similar to those applied in molecular statistical theory [125], but adapted to adsorption problems, helps to bridge the "pressure gap" between the "actual" experimental conditions and DF studies. Previously, such an approach has been successfully applied to other surface systems, e.g. for the study of the surface composition of α-Al_2O_3(0001) in contact with O_2 and H_2 environments [126], of the RuO_2(110) surface in contact with O_2, CO and H_2O [127-130]; of ZnO surfaces [131] as well as of Ag(111) [132,133] and PdO [134-136] in equilibrium with O_2 atmosphere.

Here, we model surface reactions that could possibly occur on surfaces exposed to steam. In the following sections, we will first present the theoretical background of atomistic thermodynamics, followed by a discussion of possible model surface reactions occurring on the catalysts under study. Thereafter, we will discuss adsorption complexes of various H_2O-related species on two regular surfaces, Cu(111) and PdZn(111) and analyze the expected surface compositions in the course of reaction with the help of surface energy plots and kinetic modeling. We have chosen these surfaces because metallic Cu and PdZn alloys are known as MSR catalysts, and we would like to know how H_2O is involved in the MSR reaction on these catalysts. In the following, we will mainly focus on regular defect-free surfaces and we will comment on the effect of surface defects at the end of Subsection

7.4.5. The electronic structure methods and models used in this chapter are the same as those in Chapter 3.

7.1. Background: *Ab Initio* Thermodynamics

The following exposition of "ab initio" thermodynamics as applied to adsorption problems follows the presentation first given by Reuter and Scheffler [124].

The equation for a generalized chemical reaction can be written as

$$\sum_i N_i X_i = 0 \tag{7.1}$$

where X_i represent the chemical species and N_i are the corresponding stoichiometric coefficients. The values of N_i are positive if X_i is a product and negative if it is a reactant. To determine the thermodynamics of a reaction at constant temperature T and constant pressure p, the quantity of interest is the Gibbs free energy of reaction, ΔG_r,

$$\Delta G_r\left(T, p_1, p_2, ...\right) = \sum_i N_i \mu_i\left(T, p_i\right) \tag{7.2}$$

Here, p_i is the partial pressure of species X_i and μ_i is the corresponding chemical potential, which is defined as

$$\mu_i = \frac{\partial G}{\partial N_i} \tag{7.3}$$

Before we go any further, we note that for an adsorption reaction, where one of the reactants and products is an infinite surface, these definitions have to be slightly adapted. Whereas for an adsorbate gas-phase species X_i, the chemical potential μ_i is the partial Gibbs free energy of a single molecule, for surfaces and surface complexes we cannot speak in terms of a number of particles; instead we will always refer to the Gibbs free energy G per unit cell. For example, in the reactions R1–R9 below, the surface enters with the stoichiometric coefficient one, implying one unit cell reacts with one or, for some reactions, with a half of an adsorbate molecule. Hence, instead of $\mu_i N_i$ terms, for the clean surface and the

corresponding surface complex, we will simply use the corresponding G potentials per unit cell in Eq. (7.2).

For systems where gas phase species and species adsorbed on a surface are in thermal equilibrium, the surface energy γ is of interest, defined as:

$$\gamma = \gamma^{clean} + \Delta G_r \left(T, p_1, p_2, ...\right) / A \tag{7.4}$$

Here, A is the area of the surface unit cell, γ^{clean} is the surface energy of the clean surface, defined as

$$\gamma^{clean} = [G_{slab} - G_{bulk}] / A \tag{7.5}$$

and ΔG_r is the Gibbs free energy change of an adsorption reaction, e.g., reactions R1 to R9 below.

7.1.1 From the Total Energy to the Gibbs Free Energy

The Gibbs free energy G is related to the Helmholtz free energy F [125] by

$$G(T, p) = F(T) + pV \tag{7.6}$$

Pressure p and volume V are meaningful system parameters for gas-phase species only. For surfaces, volume and pressure are not defined and G is equal to F. For gas-phase species, pV contributions will be introduced into a surface energy calculation via Eqs. (7.4) and (7.21) (see below) where tabulated values of chemical potentials are invoked for species in the gas phase. When several gas phase species are present in the system, the corresponding values of partial pressure p_i are to be used in place of p.

For a clean surface and for a surface with an adsorbed complex, the DF electronic energy E^{el} (per unit cell) at 0 K and F are independent of p (see below for the defination of F^{vib}) and related as follows:

$$F(T) = E^{el}(0) + F^{vib}(T) \tag{7.7}$$

where

$$F^{vib}(T) = E^{vib}(T) - TS^{vib}(T) \tag{7.8}$$

comprises all terms related to the vibrational modes of the system, namely the energy contribution E^{vib} (including the ZPE) and the corresponding entropy contribution S^{vib}.

To calculate the contributions to F due to vibrational motion, we employ the same formulas of statistical thermodynamics as applied for gas-phase molecules [125]. However, we shall take into account only the adsorbate-related vibrational degrees of freedom; vibrations that belong to the substrate are assumed to remain unchanged during the surface reaction. The molecular partition function of a harmonic oscillator with frequency ω is [125]:

$$q_{vib} = \prod_i \frac{e^{-\beta\hbar\omega_i/2}}{1-e^{-\beta\hbar\omega_i}} \tag{7.9}$$

where $\beta = 1/\mathrm{k}T$. Then the vibrational energy [125] is given as follows

$$E^{vib}(T) = -\frac{\partial}{\partial\beta}\ln q_{vib} \tag{7.10}$$

Substituting Eq. (7.9) into Eq. (7.10), we have

$$E^{vib}(T) = -\sum_i \frac{\partial}{\partial\beta}\ln\left(\frac{e^{-\beta\hbar\omega_i/2}}{1-e^{-\beta\hbar\omega_i}}\right) = \sum_i\left(\frac{1}{2}\hbar\omega_i + \frac{\hbar\omega_i e^{-\beta\hbar\omega_i}}{1-e^{-\beta\hbar\omega_i}}\right) \tag{7.11}$$

The entropy [125] is defined as

$$S^{vib}(T) = k\left(\ln q_{vib} + \beta E^{vib}\right) \tag{7.12}$$

Substituting Eq. (7.9) into Eq. (7.12), we have

$$S^{vib}(T) = -k\sum_i \ln\left(1-e^{-\beta\hbar\omega_i}\right) + k\beta\sum_i\left(\frac{\hbar\omega_i e^{-\beta\hbar\omega_i}}{1-e^{-\beta\hbar\omega_i}}\right) \tag{7.13}$$

and using the relationship $F^{vib} = E^{vib} - TS^{vib}$, i.e. (7.11) – $T \times$ (7.13), we obtain

$$F^{vib}(T) = \sum_i \left\{ \frac{1}{2}\hbar\omega_i + kT \ln\left(1 - e^{-\beta\hbar\omega_i}\right) \right\} \tag{7.14}$$

7.1.2 Temperature and Pressure Dependence of the Gibbs Free Energy

In this subsection we will provide expressions for chemical potentials of gas-phase species entering Eq. (7.2) and we will relate them to our calculated quantum chemical energies. We will show how to express the temperature and pressure dependence of μ_i in a form that is convenient for invoking tabulated values from standard thermodynamic tables.

As pressure and temperature are the "natural" variables of the Gibbs free energy, one has

$$dG = \left(\frac{\partial G}{\partial T}\right)_p dT + \left(\frac{\partial G}{\partial P}\right)_T dp = -SdT + Vdp \tag{7.15}$$

where the Maxwell relations [137] for the entropy S and the volume V have been used. For a species in the gas phase at constant temperature, we invoke the ideal gas law and we obtain:

$$\int_{p^\circ}^{p} dG = \int_{p^\circ}^{p} \frac{NkT}{p} dp \tag{7.16}$$

Therefore, for a finite change in pressure from p^o to p at constant temperature, we have

$$G(T, p) - G\left(T, p^0\right) = NkT \ln\left(p / p^0\right) \tag{7.17}$$

Although p^o can in principle stand for any pressure, here and in the following p^o shall denote the standard pressure (1 bar).

The temperature dependence at constant pressure p^o can be written as

$$G\left(T, p^0\right) = G\left(0,0\right) + \Delta G\left(\Delta T, p^0\right) \tag{7.18}$$

The translational and rotational contributions for a molecule at 0 K are zero, see Appendix E. Therefore, substitution of Eqs. (7.6) and (7.7) for G(0,0) yields

$$G\left(T, p^0\right) = Ne^{el} + Nf^{vib}(0) + \Delta G\left(\Delta T, p^0\right) \tag{7.19}$$

With Eq. (7.17) we obtain

$$G(T, p) = Ne^{el} + Nf^{vib}(0) + \Delta G\left(\Delta T, p^0\right) + NkT \ln\left(p / p^0\right) \tag{7.20}$$

Using the definition of a chemical potential, Eq. (7.3), we can differentiate Eq. (7.20) with respect to the number of particles N to give

$$\mu(T, p) = e^{el} + f^{vib}(0) + \mu\left(\Delta T, p^0\right) + kT \ln\left(p / p^0\right) \tag{7.21}$$

Here, e^{el} is the electronic energy of a gas phase species (computed with the DF method), and $f^{vib}(0)$ is its zero-point vibrational energy. The third and forth terms comprise the energy and entropy contributions of the translational and rotational degrees of freedom. If more than one gas phase species are present in the mixture, one has to use partial pressure p_i in place of p. For convenience, we introduce the following quantity for a gas-phase species X_i:

$$\tilde{\mu}_i(T, p_i) = \mu_i\left(\Delta T, p^0\right) + kT \ln\left(p_i / p^0\right) \tag{7.22}$$

The temperature dependence of the chemical potential at standard pressure, $\mu_i\left(\Delta T, p^0\right)$, is available in tabulated form [138]. The pressure dependence of $\tilde{\mu}_i(T, p_i)$ is given explicitly via Eq. (7.22); this quantity will become a variable of the surface energy plots to be discussed below.

Equivalently, p_i and $p°$ can be replaced by the concentrations c_i and $c°$, respectively. Eq. (7.22) then reads

$$\tilde{\mu}_i(T, c_i) = \mu_i\left(\Delta T, c^0\right) + kT \ln\left(c_i / c^0\right) \tag{7.23}$$

Thus, in analogy to gas-phase species, for adsorbed species one can write

$$\tilde{G}_i(T,\theta_i) = G_i\left(\Delta T,\theta^0\right) + kT\ln\left(\theta_i/\theta^0\right) \tag{7.24}$$

where θ_i is the surface coverage of adsorbate A_i, and θ^0 is the standard coverage, which is irrelevant in the present context. Returning to the derivations of Subsection 7.1.1, we would like to emphasize that the Gibbs free energy derived there refers to $G_i\left(\Delta T,\theta^0\right)$ and does not include the last term of Eq. (7.24). Thus, we have deliberately separated out the two terms of Eqs. (7.22) and (7.24), which implies the concept of a standard state that will be used later on when constructing surface energy plots.

7.1.3 Total Gibbs Free Energy of an Adsorption System

In the preceding subsections we have shown how to express individual terms in Eq. (7.2) and related them to the corresponding quantum-chemical electronic energies. Now, more specifically, we discuss an adsorption reaction described by the equation

$$\sum_i N_i X_i + clean\ surface = adsorption\ complex \tag{7.25}$$

Eq. (7.2) rewrites as

$$\begin{aligned}\Delta G_r\left(T,p_1,p_2,...\right) = {} & E_{ac}^{el} + F_{ac}^{vib}(T) - E_{clean}^{el} + kT\ln\left(\theta_{ac}/\theta_*\right) \\ & - \sum_i N_i\left[e_i^{el} + f_i^{vib}(0,0) + \tilde{\mu}_i(T,p_i)\right]\end{aligned} \tag{7.26}$$

where E_{ac}^{el} and E_{clean}^{el} are DF electronic energies of the adsorption complex and the clean surface, respectively, and i runs over the gas-phase species, N_i are the stoichiometric coefficients, e.g. for reaction R7 below these coefficients are 1 for H_2O and ½ for O_2, and θ_{ac}, θ_* are the surface coverage of the adsorbed species and free sites, respectively. For easy reference later, let us introduce the term $\eta = kT\ln\left(\theta_{ac}/\theta_*\right)$.

Substituting Eq. (7.26) into Eq. (7.8), we can rearrange the surface free energy as

$$\begin{aligned}\gamma(T,p_1,p_2,...) &= \gamma^{clean} + \left(E_{ac}^{el} + F_{ac}^{vib}(T) - E_{clean}^{el} + \eta - \sum_i N_i[e_i^{el} + f_i^{vib}(0,0) + \tilde{\mu}_i(T,p_i)] \right) / A \\ &= \left(E_{clean}^{el} - E_{bulk}^{el} \right) / A + \left(E_{ac}^{el} + F_{ac}^{vib}(T) - E_{clean}^{el} + \eta - \sum_i N_i[e_i^{el} + f_i^{vib}(0,0) + \tilde{\mu}_i(T,p_i)] \right) / A \\ &= \left(E_{ac}^{el} + F_{ac}^{vib}(T) - E_{bulk}^{el} + \eta - \sum_i N_i[e_i^{el} + f_i^{vib}(0,0) + \tilde{\mu}_i(T,p_i)] \right) / A \end{aligned} \tag{7.27}$$

Next, we set

$$\begin{aligned}\gamma'(T,p_1,p_2,...) &= \gamma(T,p_1,p_2,...) - \eta / A \\ &= \gamma^{clean} + \left[\Delta G_r\left(T,p_1,p_2,...\right) - \eta \right] / A \end{aligned} \tag{7.28}$$

All terms comprised in γ' can be obtained from *ab initio* calculations as described above. From Eq. (7.27), we have

$$\gamma'(T,p_1,p_2,...) = \left(E_{ac}^{el} + F_{ac}^{vib}(T) - E_{bulk}^{el} - \sum_i N_i[e_i^{el} + f_i^{vib}(0,0) + \tilde{\mu}_i(T,p_i)] \right) / A \tag{7.29}$$

Here, γ' is expressed as a function of $\tilde{\mu}_i(T,p_i)$. At equilibrium, $\Delta G_r\left(T,p_1,p_2,...\right) = 0$ and γ' becomes

$$\gamma'(T,p_1,p_2,...) = \gamma^{clean} - \eta / A \tag{7.30}$$

This uncovers the physical meaning of a function γ', which is related to η and hence related to the ratio θ_A / θ_*, on which basis we judge whether a reaction is favorable, as we will now explain. When comparing γ' of two independent reactions (a) and (b) that involve adsorbates A and B, respectively, on the same substrate, let us imagine the following situation

$$\gamma'(a) > \gamma'(b) \tag{7.31}$$

The following chain of inequalities will lead us to a quantitive comparison of these two equilibria in terms of the effective equilibrium coverages, θ_A and θ_B

$$-\eta_A > -\eta_B \Rightarrow \eta_A < \eta_B \Rightarrow kT\ln(\theta_A/\theta_*) < kT\ln(\theta_B/\theta_*) \Rightarrow \theta_A < \theta_B \quad (7.32)$$

where we have used the monotonous character of the logarithm. It follows that reaction (b) is more favorable than (a). This model applies only to individual uncoupled reactions, e.g. reactions R1–R9 discussed in Section 7.2 below, where we assume that no further reactions take place in parallel. One should not try to derive the adsorbate surface coverages from γ' plots as the rest of the coupled reactions are not considered and hence such a model does not represent the true situation on the surface under experimental conditions. Instead, the above formalism can be used for qualitative arguments, e.g., whether a given reaction is expected to occur on a surface with any significant yield, or to judge which adsorption reaction of a given set taken independent of other reactions should result in the highest coverage of the adsorbed product species. To deduce adsorbate surface coverages of all relevant species involved in coupled reactions, we will use kinetic modeling as discussed below in Section 7.4.4.

7.2 Application of Surface Thermodynamics

The goal of this section is to identify water-related species that under MSR conditions (500 K, p_{H2O} = 1 atm) are most likely to be present on the surfaces PdZn(111) and Cu(111). This information will contribute to modeling the elementary reaction steps during catalytic MSR, especially reactions (6) and (8) (Fig 1.1) which occur in the presence of water.

In the work to be discussed in the following, we have considered only a sub-system of all possible adsorption reactions. We have left out methanol and carbon containing intermediates of methanol dehydrogenation to simplify our models. However, methanol is implicitly involved in the reaction network by considering H_2 gas. Under dry conditions, methanol would be partially dehydrogenated to formaldehyde and hydrogen [5,9] on Cu and PdZn based catalysts. The subsequent reactions between water related species with formaldehyde are beyond the scope of this thesis.

Specifically, we would like to study the following surface reactions, using the substrate PdZn(111) as an example:

R1.	½ H_2(g) + PdZn(s)	↔	H/PdZn(s)
R2.	½ O_2(g) + PdZn(s)	↔	O/PdZn(s)
R3.	H_2O(g) + PdZn(s)	↔	H_2O/PdZn(s)
R4.	H_2O(g) + PdZn(s)	↔	(H + OH)/PdZn(s)
R5.	H_2O(g) + PdZn(s)	↔	½ H_2(g) + OH/PdZn(s)
R6.	H_2O(g) + PdZn(s)	↔	H_2(g) + O/PdZn(s)
R7.	H_2O(g) + ½ O_2(g) + PdZn(s)	↔	(2 OH)/PdZn(s)
R8.	½ H_2(g) + ½ O_2(g) + PdZn(s)	↔	OH/PdZn(s)
R9.	H_2(g) + ½ O_2(g) + PdZn(s)	↔	H_2O/PdZn(s)

As mentioned above, in MSR, methanol acts as a source of H_2. Thus, we consider H_2 dissociation (R1) and associative desorption of H_2 reaction (-R1). We included O_2 dissociation (R2) and associative desorption of O_2 reaction (-R2) as oxygen may be introduced into the system (see below). Of course, we need to consider H_2O adsorption (R3) and various dissociation reactions (R4, R5 and R6) to probe H_2O related species. Because we considered O_2 to be in the system, adsorbed O atoms can dissociate H_2O (R7) and H_2. Reactions R8 and R9 represent end results.

We take the partial pressure p_{H2} of hydrogen as a parameter of our surface energy study because H_2 is a product of methanol dehydrogenation to formaldehyde as well as of H_2O decomposition; see Fig. 1.1 for reaction scheme. Therefore, it is appropriate to study the partial pressure of hydrogen from the onset of the MSR reaction (p_{H2} = 0 atm) to partial decomposition of methanol to formaldehyde and molecular hydrogen in the absence of H_2O (p_{H2} = 1 atm) [5,9]. Also, O_2 can be introduced into the system if H_2O (or methanol, but we have left out methanol in our analysis here) had been exposed to air. For instance, using Henry's Law and assuming air at 1 atm and 298 K, the solubility of O_2 in H_2O is estimated at ~ 3.2 x 10^{-4} mol (O_2)/kg (H_2O) [139] or ~5.8 x 10^{-6} mol (O_2) / mol (H_2O). Hence, invoking the ideal gas equation, vaporizing this water sample will give ~10^{-6} atm O_2 for every 1 atm of H_2O. Another source of O_2 is water that has been decomposed at the surface of the metal catalyst (reaction R6), followed by recombination and desorption (reverse of

reaction R2). Therefore, in our present study, it seems reasonable to assume that the partial pressure of oxygen ranges from 0 atm to 10^{-6} atm; the latter value represents O_2 dissolved in water.

In this thermodynamics study of surface reactions, we will apply Eq. (7.27) to the scheme of (coupled) reactions R1 to R9 at 500 K, the MSR reaction temperature. For the vibrational corrections, we tabulated all pertinent information in Appendix E: the calculated vibrational frequencies of the most stable structures of the adsorption complexes of H, O, OH, and H_2O as well as of the gas phase species H_2, O_2 and H_2O and the corresponding F^{vib} contributions. Likewise, we tabulated the calculated values of $\tilde{\mu}_i$ for H_2, O_2 and H_2O at 500 K, assuming a pressure range from 10^{-15} to 1 atm (Appendix F). We will use the chemical potentials at 500 K and 10^{-15} atm to represent the lower concentration limit (0 atm) for H_2 and O_2. {Note that ultra high vacuum (UHV) conditions corresponds to a total pressure ~10^{-14} atm [31].} From Appendix F, we then have $\tilde{\mu}_i$ = -2.48 eV for H_2 and $\tilde{\mu}_i$ = -2.10 eV for O_2. To study the effect of high partial pressure of O_2 and H_2 on our system, we used $\tilde{\mu}_i$ = -0.61 eV (500 K, 1 atm) for H_2 and $\tilde{\mu}_i$ = -1.59 eV (500 K, 10^{-6} atm) for O_2 (Appendix F). For Eqs. R5, R6 and R7, we fixed $\tilde{\mu}_{H_2O}$ at -0.90 eV (1 atm, 500 K) when investigating the dependence on H_2 and O_2.

7.3 Adsorption Studies of H_2O Related Species

Before going into surface energy plots, we will discuss the calculated binding energies of H, O, OH and H_2O on the surfaces PdZn(111) and Cu(111). As binding energies vary with the surface site, we used the total energy of the most stable adsorption complex in the surface energy plots.

7.3.1 Dissociative Adsorption of H_2 and O_2

Our calculated atomization energies of molecular H_2 (439 kJ mol^{-1}) and molecular O_2 (594 kJ mol^{-1}) in the gas phase agree satisfactorily with other reported values obtained with the same functional (PW91) [140]: 439 kJ mol^{-1} and 598 kJ mol^{-1}, respectively. The optimized

bond distances, 74 pm for H_2 and 124 pm for O_2 were also in good agreement with experiment: 74 pm and 121 pm, respectively [141].

Table 3.2 summarizes the binding energy of atomic H and atomic O on various high symmetry sites on PdZn(111) and Cu(111) surfaces (see Chapter 3). Here, we have presented the binding energies with respect to molecular hydrogen and oxygen, Table 7.1. Table 7.1 shows that on the surfaces PdZn(111) and Cu(111) H_2 dissociation is weakly exothermic (~20 kJ mol^{-1}/H atom) and O_2 dissociation is strongly exothermic (~160 kJ mol^{-1}/ O atom).

7.3.2 OH Adsorption

On PdZn(111), OH prefers hollow sites with high Zn atoms coordination (see Table 7.1). This is in agreement with our finding in Chapters 3, 4 and 5, that adsorbates binding through an O atom to a PdZn alloy surface prefer high Zn coordination. Similar to atomic oxygen and methoxide, the highest binding energy of OH on PdZn(111) is slightly lower (by ~15 kJ mol^{-1}) than the binding energy, 309 kJ mol^{-1}, on Cu(111) (see Section 3.2). The binding energy at the fcc site on Cu(111) is comparable to the previously reported value of 275 kJ

Table 7.1. Binding energy BE (kJ mol^{-1}) of atomic H, atomic O, OH and H_2O at various sites of the surfaces PdZn(111)[a] and Cu(111)[b]. The BEs are calculated with respect to gas-phase H_2 and O_2, i.e. BE = ½ E_{X2} + E_{sub} – $E_{X/sub}$, where X = H, O.

		T^{Pd}	T^{Zn}	B^{Pd2}	B^{Zn2}	F^{Pd2Zn}	F^{PdZn2}	H^{Pd2Zn}	H^{PdZn2}
H	PdZn	-5	-73	23	-49	22	5	29	-11
	Cu	-36		6		18		18	
O	PdZn	-50	-14	44	145	94	156	103	144
	Cu	-3		125		168		158	
OH	PdZn	224	228	228	290	257	294	268	285
	Cu	232		294		309		308	
H_2O	PdZn	20	23	13	15	14	13	12	15
	Cu	23		17		17		16	

[a] See Fig. 3.1 for the designations of the adsorption sites on the PdZn(111) surface.

[b] For Cu, T^{Pd}, B^{Pd2}, F^{Pd2Zn}, and H^{Pd2Zn} correspond to the top, bridge, fcc and hcp sites, respectively.

mol^{-1} [33]. The difference reflects different slab models used in the two calculations (3 layers vs. 4 layers here). Note the interaction between the H atom of OH and Pd atoms on the PdZn(111) surface. At a T^{Pd} site, the OH radical is tilted at an angle of 58° to the surface normal to allow an efficient interaction between the H atom with the same Pd atom as the O atom. This configuration permits the OH radical to bind to a top site T^{Pd} (224 kJ mol^{-1}) almost as strongly as to a T^{Zn} site (228 kJ mol^{-1}). This is in contrast to the case of O adsorption where the binding energy difference is ~ 36 kJ mol^{-1} between these two sites, i.e. O/PdZn, T^{Pd} - -50 kJ mol^{-1} and T^{Zn} - -14 kJ mol^{-1}.

7.3.3 H_2O Adsorption

The geometry optimization was conducted with the molecular plane of H_2O parallel to the surface. This configuration was observed during IRAS experiment on the surfaces Ru(0001) and Pt(111) [142], and confirmed by DF calculations [143,144]. As on the Ru and Pt surfaces, H_2O prefers to adsorb at the top site of PdZn alloy and Cu (see Table 7.1). However, H_2O is weakly adsorbed on the PdZn and Cu surfaces with binding energies of up to 23 kJ mol^{-1}. These results agree with a previously reported value of 18 kJ mol^{-1} for Cu(111) [33]. Note that the difference in binding energies between the T^{Pd} and T^{Zn} sites on PdZn alloy is less than in the case of OH adsorption. This is most likely due to an additional H-Pd interaction in the latter case.

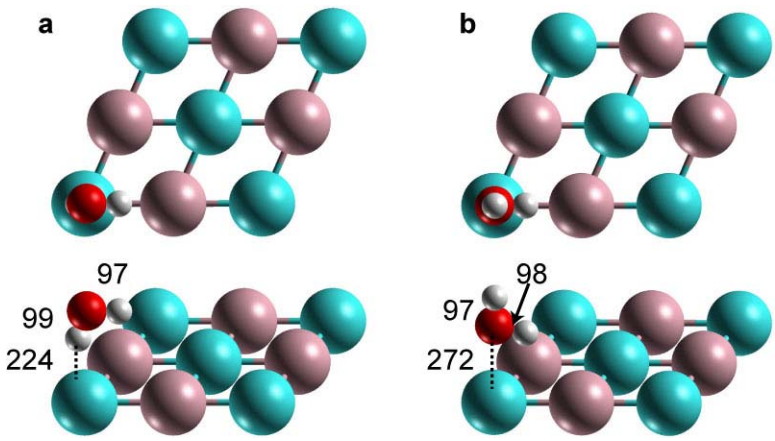

Figure 7.1. Top (upper panels) and side views (lower panels) of (a) H-down and (b) H-up configurations of H_2O at a T^{Pd} site of PdZn(111). Selected bond-lengths are given in pm. Atomic spheres: blue – Pd, pink – Zn, red – O, light gray – H.

To gain a better understanding of the H-Pd and H-Zn interactions in the case of H_2O adsorption, we also studied the H_2O configurations H-up and H-down at the top site (see Fig. 7.1). These two configurations are important for a high surface coverage regime (i.e. 2/3) as they form part of the reported 2-D ice-like structure on metal surfaces [145,146]. Our calculations indeed showed that the binding energy of the H-up configuration was more stable at the T^{Zn} site, 12 kJ mol^{-1}, compared to 6 kJ mol^{-1} on the T^{Pd} site. On the other hand, the H-down configuration was more stable at the T^{Pd} site, 12 kJ mol^{-1}, compared to 9 kJ mol^{-1} on the T^{Zn} site. Yet, the most favorable configurations are still those with the molecular plane of H_2O parallel to the surface. The potential energy surface for adsorbed H_2O molecule is rather flat with binding energy differences of ~10 kJ mol^{-1} across all configurations (molecular plane parallel to the surface), in contrast to the Ru(0001) surface, where binding energy differences beyond 20 kJ mol^{-1} have been calculated between the top site and other high-symmetry sites [143]. Note that such a weak binding calculated for H_2O here has to be considered outside the range where DF-GGA energy functionals are reliable; this is mainly due to the fact that contemporary exchange-correlation potentials do not account for dispersive interactions [147]. Furthermore, adsorption energies of molecular species on *d*-metals, computed with the exchange-correlation functional PW91 used in this work, are in general somewhat higher than the corresponding experimental values [148]. Therefore, the binding energy of H_2O calculated here should be considered as an estimate.

7.4 Surface Free Energy Curves of the Reactions on PdZn(111) and Cu(111)

The surface energies of clean PdZn(111) and Cu(111) surfaces have previously been calculated at 73 meV $Å^{-2}$ and 84 meV $Å^{-2}$, respectively [50]. Here, we would like to study the most likely H_2O related species under steam reforming conditions on the surfaces PdZn(111) and Cu(111) by comparing the free energies of adsorbed complexes with the corresponding surface energy of the clean surfaces as a function of the partial pressure, or equivalently, the chemical potential of an adsorbed gas.

7.4.1 H/Cu(111) as Example

As an illustration, we will demonstrate for the system H/Cu(111) how the surface energy is evaluated. We consider reaction R1,

$$\tfrac{1}{2}\,H_2(g) + Cu(s) \quad \equiv \quad H/Cu(s) \tag{7.33}$$

and write Eq. (7.30) for this system as

$$\begin{aligned}\gamma'(T, p_{H2}) - \gamma^{cl} = \Big[& E_{H/Cu(111)} + F^{vib}_{H/Cu(111)}(T) - E^{Cu}_{bulk} \\ & -0.5\left(E_{H2} + F^{vib}_{H2}(0,0) + \tilde{\mu}_{H2}(T, p_{H2})\right)\Big] / A\end{aligned} \tag{7.34}$$

where A is the surface area of one side of the slab. The surface energy γ^{cl} of one side of a clean Cu(111) slab is used to correct for the energy of the surface exposed at the "bottom" of the slab model. The surface energy of this system at p_{H2} = 1 atm and 500 K is evaluated by inserting all values as obtained from Appendixes A, E, F, and G into Eq. (7.34),

$$\begin{aligned}\gamma'(500\text{ K, }1\text{ atm}) = \Big[& -59.350*1000 + 148 - (16*(-3.730)*1000) \\ & - 0.5*\big((-6.788*1000) + (-0.610*1000) + 190\big)\Big] \\ & / 22.8\text{ meVÅ}^{-2} - 84\text{ meVÅ}^{-2} \\ = & \ 95\text{ meVÅ}^{-2}\end{aligned} \tag{7.35}$$

In Eq. (7.30), the only variable is $\tilde{\mu}_{H2}$, which is a function of temperature and pressure (see Eq. (7.22)). Therefore, the surface energy plot can be obtained with γ as a function of $\tilde{\mu}_{H2}$.

7.4.2 Dependence on the Partial Pressure of Hydrogen

On the PdZn(111) surface, the surface energy corresponding to dissociative H_2 adsorption is 83 meV Å^{-2} (Eq. R1) at T = 500 K and P_{H2} = 1 atm, higher than the clean surface energy of 73 meV Å^{-2}. Hence, thermodynamically, dissociative H_2 adsorption is unfavorable on the PdZn (111); see Fig. 7.2. In contrast, dissociative adsorption of O_2 (Eq. R2, Fig. 7.4) readily occurs on PdZn(111), also at low pressure. At 500 K and p_{H2O} = 1 atm, the calculated surface energy for Eq. R3 is 98 meV Å^{-2}. Therefore, H_2O adsorption at the surface is thermodynamically unfavorable under these conditions. Beside an oxygen covered surface,

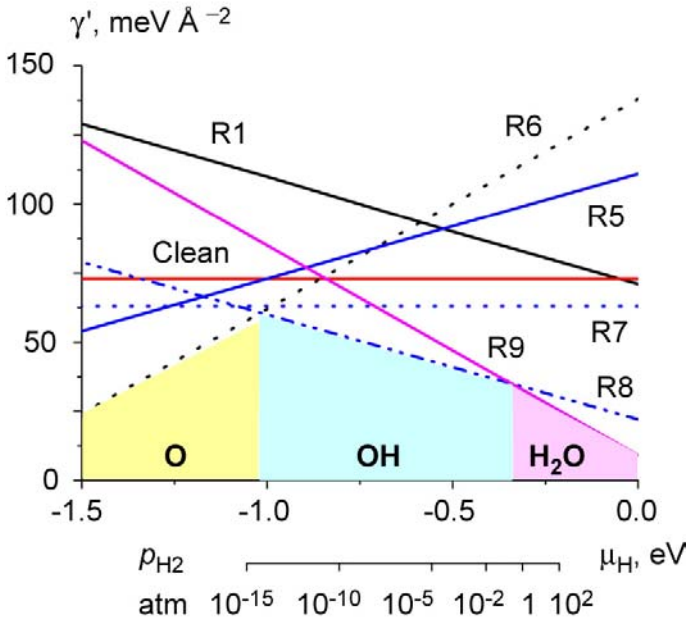

Figure 7.2. Surface energy γ′ vs. chemical potential $\tilde{\mu}_H$, on the PdZn(111) surface. The p_{H2} scale shown corresponds to $\tilde{\mu}_H$ at T = 500 K. Rn, n = of the surface reaction, see Section 7.2. $p_{O2} = 10^{-6}$ atm for R7, R8 and R9. Colored areas represent the most favorable species for a given range of the chemical potential (or the pressure).

we also find that the surface with adsorbed OH is stable for a certain range of p_{H2} and p_{O2} values (Fig. 7.2). On the Cu(111) surface, similar trends were observed (Fig. 7.3). Now, we will discuss these surface energy plots in more detail.

From Fig. 7.2, dissociative adsorption of H_2 at 500 K and p_{H2} = 1 atm is unfavorable with respect to the clean surface (Eq. R1). This agrees with experimental findings: under MSR conditions (500 K and p_{H2} ~1 atm), H_2 desorbs from the surface. Recall that in the initial phase of an MSR reaction, p_{H2} = ~0 atm. From Fig. 7.2 follows that for $p_{H2} < 10^{-15}$ atm and p_{H2O} = 1 atm an oxygen-covered surface resulting from H_2O dissociation (Eq. R6) is the most favorable outcome. With increasing values of p_{H2}, at $p_{H2} > 10^{-15}$ atm, coverage of the surface by hydroxyl groups becomes more favorable due to hydrogenation of surface oxygen (Eq. R8). At even larger values of p_{H2}, beyond 0.1 atm, surface hydroxyl groups are converted to H_2O (Eq. R9), which desorbs from the surface (Eq. -R3), because the surface energy of adsorbed H_2O is always higher than that of the clean surface. Note also that H_2O dissociation in the presence of surface oxygen (Eq. R7) is always favorable compared to the clean surface, but other reactions mentioned above, R6, R8 and R9, are less favorable in various pressure intervals.

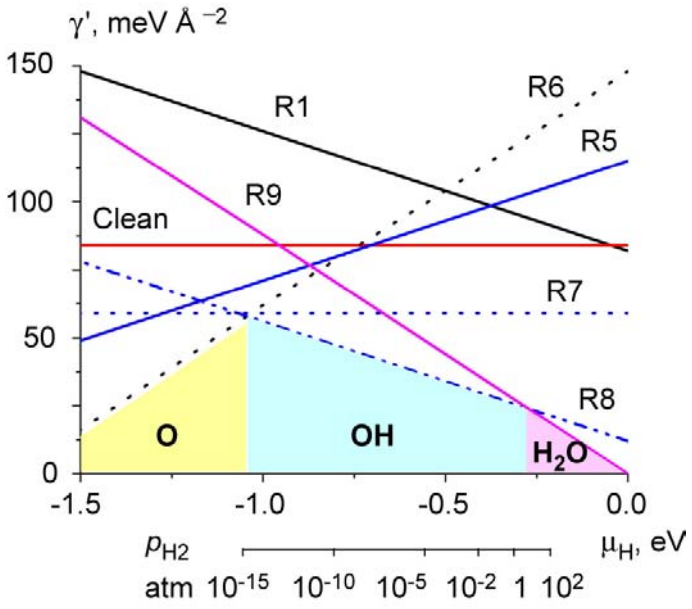

Figure 7.3. Surface energy γ' vs. chemical potential $\tilde{\mu}_H$ on the Cu(111) surface. The p_{H2} scale shown corresponds to $\tilde{\mu}_H$ at T = 500 K. Rn, n = number of the surface reaction, see Section 7.2. $p_{O2} = 10^{-6}$ atm for R7, R8 and R9. Colored areas represent the most favorable species for a given range of the chemical potential (or the pressure).

On the surface Cu(111) (Fig. 7.3), the surface energy curves exhibit trends similar to those on PdZn(111). This is reminiscent of the similarity calculated for the adsorption properties and the reactivity of Cu and PdZn; see Chapters 3 and 6. The differences in the phase transitions are mainly due to differences in the clean surface energy and the adsorbate binding energies. Again, dissociative adsorption of H_2 is unfavorable on this surface at T = 500 K and p_{H2} = 1 atm. On Cu(111), surface OH is more favorable than H_2O for $p_{H2} < 2$ atm, whereas on PdZn(111), surface OH becomes unfavorable compared to H_2O when $p_{H2} >$ 0.1 atm. This finding of stable surface OH species is reminiscent of recent results of diffuse reflectance infra-red Fourier transform spectroscopy (DRIFTS) [149]. On Cu/Zn/Zr-based catalysts, OH species have been detected on the surface when the catalyst had been exposed either to (i) H_2 or (ii) CH_3OH and H_2O [149]. Also, a recent kinetic study reported that the rate of the MSR reaction over $Cu/ZnO/Al_2O_3$ catalysts depends on p_{H2} and is independent of p_{H2O} [18].

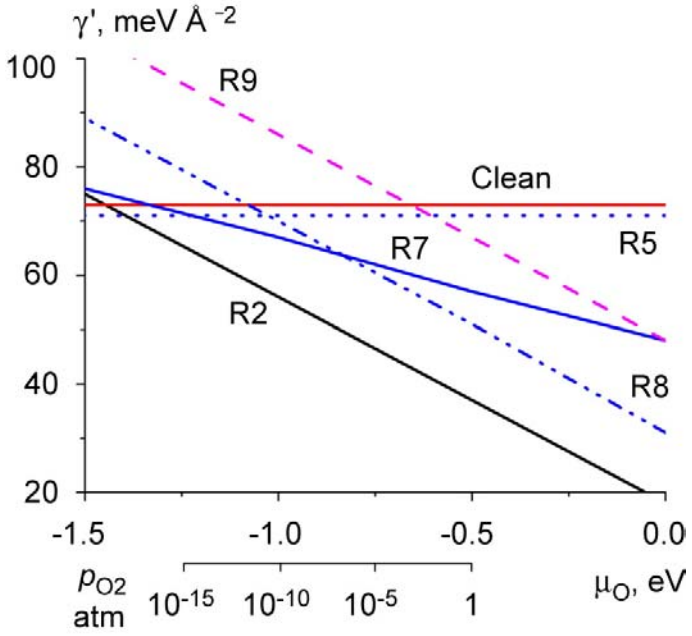

Figure 7.4. Surface energy γ' vs. chemical potential $\tilde{\mu}_O$, on the surface PdZn(111). The p_{O2} scale shown corresponds to $\tilde{\mu}_O$ at T = 500 K. Rn, n = number of the surface reaction, see Section 7.2. $p_{H2} = 10^{-15}$ atm for R8 and R9.

7.4.3 Dependence on the Partial Pressure of Oxygen

Dissociative adsorption of O_2 on PdZn(111) is highly exothermic (-312 kJ mol^{-1}) compared to H_2 (-58 kJ mol^{-1}); see Table 7.1. Therefore, as already mentioned, at 500 K the phase O/PdZn(111) (R2) from O_2 dissociation is more favorable than the clean surface even at low values of p_{O2}, ~10^{-15} atm (Fig. 7.4) and is independent of H_2O pressure. However, as seen in Fig. 7.2, surface oxygen becomes thermodynamically unfavorable compared to surface hydroxyl for $p_{H2} > 10^{-15}$ atm (Eq. R8) and eventually is converted to H_2O at $p_{H2} > 0.1$ atm (Eq. R9). Similar trends are observed on Cu(111) (Fig. 7.3).

In summary, as contribution to unraveling the reaction network of MSR, we traced how H_2O-derived species modify the structures surfaces of PdZn(111) and Cu(111). For the initial phase of MSR, i.e. before the decomposition of methanol starts (P_{H2} = ~0 atm), we predict a oxygen-covered surface to be stable, either through decomposition of water (R6) or from oxygen dissolved in the reactant water (Eq. R2). Subsequently, this surface oxygen may help to abstract H from H_2O into the OH phase (Eq. R7) because we calculated the reaction $H_2O + O \rightarrow 2OH$ to be more exothermic on PdZn(111) surface, -38 kJ mol^{-1}, than the essentially energy-neutral reaction $H_2O \rightarrow OH + H$, 10 kJ mol^{-1} (6 kJ mol^{-1}). This

statement also holds for (Cu(111) where the reaction energy of $H_2O + O \rightarrow 2OH$ was calculated at -58 kJ mol^{-1}. As the MSR reaction proceeds, the partial pressure p_{H2} increases and surface OH becomes stable in the range of 10^{-15} atm < p_{H2} < 0.1 atm; for Cu(111), the upper end of that rage extends to 2 atm. With further increasing values of p_{H2}, surface hydroxyl becomes unstable with respect to H_2O (R9), which desorbs from the surface (reverse of R3).

7.4.4 From the Surface Free Energy to the Surface Coverage

Next we are interested in the relationship between the surface free energy and surface coverages of adsorbed species. The latter term enters the Gibbs free energy; see Eq. (7.24). We will establish this relation for reaction of H_2O with a surface by exploring the elementary steps of the model reaction

$$H_2O + * \rightarrow H_2 + O* \tag{7.33}$$

where * represents empty surface sites. We will use microkinetic modeling similar to that employed in Ref. [150]. Microkinetic modeling begins with postulating a reaction mechanism. Once the reaction mechanism is postulated, the parameters that are of no interest to the specific study, such as activation energies, reaction energies, vibrational frequencies of adsorbed molecules, pre-exponential factors for reactions, etc., are substituted with either calculated data or results of experimental kinetic studies, whereas those parameters that are of interest, such as surface coverage, are obtained from fitting the model to experimental data obtained from laboratory reactor systems.

The elementary steps of Eq. (7.33) are written as follows:

a. $H_2O + * \leftrightarrow H_2O*$

b. $H_2O* + * \leftrightarrow H* + OH*$

c. $OH* + * \leftrightarrow H* + O*$

d. $2H* \leftrightarrow H_2 + 2*$

Table 7.2. Tabulation of calculated K_i, i = a, b, c, d at T= 500 K, for reactions (a) to (d) on PdZn(111) and Cu(111) surfaces.

	K_a	K_b	K_c	K_d
PdZn(111)	$2.41\text{x}10^{-7}$	$0.78\text{x}10^{-2}$	$2.21\text{x}10^{-6}$	$1.97\text{x}10^{5}$
Cu(111)	$1.49\text{x}10^{-5}$	$7.93\text{x}10^{-1}$	$1.22\text{x}10^{-7}$	$1.14\text{x}10^{5}$

where * represents empty adsorption sites and A*, A = H, O, OH, H_2O, represent adsorbed species. While the reaction set above is a part of the net MSR process, we have to assume as a first approximation that reactions (a)-(d) all achieve quasi-equilibrium on the timescale shorter than that of MSR. Whether this assumption is reasonable may be arguable, and we will address this shortly, but at least for adsorption reactions (a) and (d) with the barriers of about 0 and 70 kJ mol^{-1} [33], respectively, the equilibrium with the gas phase should be achieved faster than the time scale on which most surface reactions occur.

By assuming reactions (a)-(d) to be quasi-equilibrated, we imply that, along with the slowly increasing partial pressure of H_2 as MSR proceeds, the equilibria on the surface also get shifted, but for a given fixed p_{H2} and total pressure, "equilibrium" concentrations of the species on the surface can be derived. Thus, we are talking about a constrained equilibrium, a concept already introduced at the beginning of this chapter. The equilibrium constants [150] for elementary reactions (a), (b), (c), and (d) can then be written as

$$\text{(a)}\quad K_a = \exp(\frac{-\Delta G_a^0}{RT}) = \exp(\frac{-A\Delta\gamma_a}{RT} + \ln\frac{p^0}{p_{H2O}}) = \frac{\theta_{H2O}p^0}{\theta_* p_{H2O}} \tag{7.34}$$

$$\text{(b)}\quad K_b = \exp(\frac{-\Delta G_b^0}{RT}) = \frac{\theta_{OH}\theta_H}{\theta_{H2O}\theta_*} \tag{7.35}$$

$$\text{(c)}\quad K_c = \exp(\frac{-\Delta G_c^0}{RT}) = \frac{\theta_O\theta_H}{\theta_{OH}\theta_*} \tag{7.36}$$

$$\text{(d)}\quad K_d = \exp(\frac{-\Delta G_d^0}{RT}) = \exp(\frac{-A\Delta\gamma_d}{RT} + \ln\frac{p_{H2}}{p^0}) = \frac{\theta_*^2 p_{H2}}{\theta_H^2 p^0} \tag{7.37}$$

where θ_A, A = *, H, O, OH, H_2O, represents the respective surface coverages of A, and K_i, i = a, b, c, d, are the corresponding equilibrium constants. Next, we express θ_A in terms of θ_*:

$$\text{(a)}\ \theta_{H2O} = \frac{p_{H2O}}{p^0} K_a \theta_* \tag{7.38}$$

$$\text{(b)}\ \begin{aligned} \theta_{OH} &= \frac{\theta_{H2O}}{\theta_H} K_b \theta_* = \left(\frac{p_{H2O}}{p^0} K_a \theta_*\right)\left(\sqrt{\frac{p_{H2}}{K_d p^0}}\theta_*\right)^{-1} K_b \theta_* \\ &= p_{H2O}(p_{H2} p^0)^{-0.5} K_a K_b K_d^{0.5} \theta_* \end{aligned} \tag{7.39}$$

$$\text{(c)}\ \theta_O = \frac{\theta_{OH}}{\theta_H} K_c \theta_* = p_{H2O} K_a K_b K_c K_d \theta_* / p_{H2} \tag{7.40}$$

$$\text{(d)}\ \theta_H = \sqrt{\frac{p_{H2}}{K_d p^0}}\theta_* \tag{7.41}$$

By substituting Eqs. (7.38) – (7.41) in the conservation law

$$\theta_* + \theta_H + \theta_O + \theta_{OH} + \theta_{H2O} = 1 \tag{7.42}$$

one can solve for individual coverages θ_A, A = H, O, OH, H_2O, and * at any given pair of pressure values p_{H2O} and p_{H2}.

Fig. 7.5 shows the relationship between the adsorbates surface coverages and p_{H2} under T = 500 K, and p_{H2O} = 1 atm (black curves) as well as 0.01 atm (red curves) on the surfaces PdZn(111) and Cu(111). On the PdZn(111) surface, at p_{H2O} = 1 atm (black curves), the surface is dominated by surface O when p_{H2} is less than 10^{-9} atm. When p_{H2} is above 10^{-9}, most surface sites are empty. The trends observed here are similar to those seen in Fig. 7.2. In Fig. 7.2, we have predicted that the formation of adsorbed H_2O* by reaction R9 is more favorable at high p_{H2} than the formation of adsorbed O* and OH* and that H_2O is subsequently desorbed from the surface, because of $\eta < 0$ for Eq. R3 at $p_{H2O} \sim 1$ atm rendering H_2O adsorption unfavorable.

Not surprisingly, on the Cu(111) surface, our microkinetic model predicts a similar behavior as for PdZn(111), but an additional surface phase of dominating adsorbates is

anticipated. In particular, at p_{H2} less than 10^{-8} atm, O* dominates the surface; at higher values of p_{H2} until 10^{-4} atm, OH* dominates the surface, and for even higher values of p_{H2}, the surface sites are mostly free.

The dependence on p_{H2O} is also shown in Fig. 7.5. At lower values of p_{H2O} (p_{H2O} = 0.01 atm, red lines), the transitions between the surface compositions shift to lower values of p_{H2}. In fact on PdZn(111), the surface will be essentially free already when p_{H2} is above 10^{-9} atm

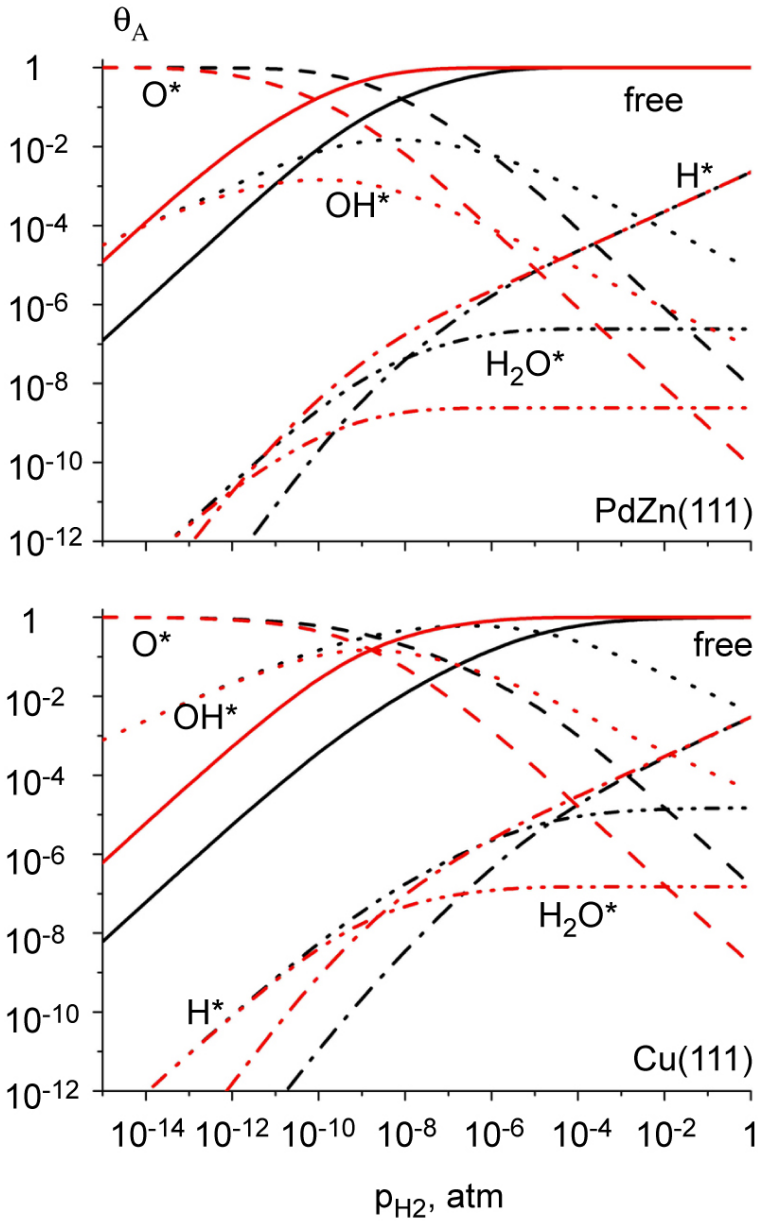

Figure 7.5. Coverage θ_A as a function of p_{H2} for the adsorbates A = *, H, O, OH, H_2O due to the reaction $H_2O \rightarrow H_2 + O^*$ on PdZn(111) and Cu(111) at 500 K. Red curves – p_{H2O} = 0.01 atm, black curves – p_{H2O} = 1 atm. Labeling of lines: dash – O*, dot – OH*, solid – free, dash dot – H*, and dash dot dot – H_2O.

and on Cu(111), the free sites will begin to dominate when p_{H2} is above 10^{-8} atm. Another difference is the decreased maximum coverages of H_2O and OH because there are less H_2O molecules available for adsorption and hence dissociation.

This analysis suggests that at the beginning of a MSR process (at low values of p_{H2}) the surface is mainly covered by O*, whereas later, when the reaction has reached a steady state where the production of H_2 is constant ($p_{H2} \sim 1$ atm), the surface is essentially adsorbate-free. (Recall that any carbon related species are being disregarded in this model as potential adsorbates.) From this modeling, one expects that MSR undergoes a very different reaction path during the induction period before reaching a steady state.

Pfeifer et al. [20] reported that higher selectivity for CO over CO_2 was observed during the initial high conversion phase of MSR, indirectly corroborating our hypothesis that the initial high O* surface coverage might be responsible for the higher activity and possibly a different mechanism that leads to high selectivity for CO. Note, however, that at the initial phase of reaction, due to higher catalytic activity, the net rate of H_2 production is high and hence one would expect that the situation where O* dominates the surface does not last long, leaving an essentially adsorbate-free surface for reaction at steady state.

Next, we would like to ask ourselves, what if the equilibrium assumptions for reactions (b) and (c) are not quite appropriate? Can we go a step further and consider a model which includes non-equilibrated reactions? In the following, instead of equilibrium conditions we treated the reaction set (a) – (e) under steady state conditions, which are normally achieved in a flow reactor rather than at chemical equilibrium. Here, as previously, we assume that reactions (a) and (d) are sufficiently fast to reach equilibrium, as postulated in the model above, as well as reaction (e) below

e. $2OH^* \leftrightarrow H_2O^* + O^*$

Our assumption of step (e) being fast is justified by recent DFT calculations on Cu(111) surface where reaction (e) was calculated to be exothermic by 10 kJ mol^{-1} with an activation energy of 23 kJ mol^{-1} [33]. In the quasi-equilibrium treatment above, this reaction was redundant to be in equilibrium because (e) = (c) – (b); hence, assuming (c) and (b) to be in (quasi-)equilibrium automatically leads to (e) being in equilibrium. The equilibrium constant K_e is thus expressed as

$$K_e = \frac{K_c}{K_b} \tag{7.43}$$

Reaction (e) then gives the relationship

$$\text{(e)}\ \ K_e = \exp(\frac{-\Delta G_e^0}{RT}) = \frac{\theta_O \theta_{H2O}}{\theta_{OH}^2} \tag{7.44}$$

which can be rearranged to

$$\text{(e)}\ \theta_{OH} = \sqrt{\frac{\theta_O \theta_{H2o}}{K_e}} = \sqrt{\frac{K_a p_{H2O} \theta_O \theta_*}{K_e p^0}} \tag{7.45}$$

Under the steady state assumption, the coverages of O* and OH* would be constant, i.e. the rate of OH* and O* formation is equal to the respective rates of OH* and O* removal. Using the mass balance of reactions (b), (c) and (e), we obtain for OH*

$$r_b - 2r_e - r_c = 0 \tag{7.46}$$

and for O*

$$r_e + r_c = 0 \tag{7.47}$$

Hence, Eqs. (7.46) and (7.47) give

$$r_b + r_c = 0 \tag{7.48}$$

where r_b and r_c are

$$r_b = k_b \theta_{H2O} \theta_* - (k_b / K_b) \theta_{OH} \theta_H \tag{7.49}$$

$$r_c = k_c \theta_{OH} \theta_* - (k_c / K_c) \theta_O \theta_H \tag{7.50}$$

Substituting Eqs. (7.49) and (7.50) into (7.48) leads to

$$k_b \theta_{H2O} \theta_* - (k_b / K_b) \theta_{OH} \theta_H + k_c \theta_{OH} \theta_* - (k_c / K_c) \theta_O \theta_H = 0 \tag{7.51}$$

Together with Eqs (7.38), (7.41) and (7.45), we have

$$k_b K_a (p_{H2O}/p^0)\theta_*^2 - (k_b/K_b)\sqrt{(K_a p_{H2O}\theta_O\theta_*/K_e p^0)}\sqrt{(p_{H2}/K_d p^0)}\theta_* + k_c\sqrt{(K_a p_{H2O}\theta_O\theta_*/K_e p^0)}\theta_* - (k_c/K_c)\theta_O\sqrt{(p_{H2}/K_d p^0)}\theta_* = 0 \quad (7.52)$$

Now, we divide all terms by $-\theta_*^2$ and rearrange, to get

$$-k_b K_a (p_{H2O}/p^0) + [(k_b/K_b)\sqrt{(K_a p_{H2O}/K_e p^0)}\sqrt{(p_{H2}/K_d p^0)} - k_c\sqrt{(K_a p_{H2O}/K_e p^0)}]\left(\frac{\theta_O}{\theta_*}\right)^{1/2} + (k_c/K_c)\sqrt{(p_{H2}/K_d p^0)}\frac{\theta_O}{\theta_*} = 0 \quad (7.53)$$

To solve Eq. (7.53) we let

$$x = (\theta_O/\theta_*)^{1/2} \quad (7.54)$$

Substituting Eq. (7.54) into Eq. (7.53), one obtains a quadratic equation for *x*:

$$Ax^2 + Bx + C = 0 \quad (7.55)$$

with

$$A = (k_c/K_c)\sqrt{(p_{H2}/K_d p^o)} \quad (7.56)$$

$$B = [(k_b/K_b)\sqrt{(K_a p_{H2O}/K_e p^0)}\sqrt{(p_{H2}/K_d p^o)} - k_c\sqrt{(K_a p_{H2O}/K_e p^0)}] \quad (7.57)$$

$$C = -k_b K_a (p_{H2O}/p^0) \quad (7.58)$$

In fact, *x* can be solved for analytically to give

$$x = \sqrt{p_{H2O} K_a K_b K_c K_d / p_{H2}} \quad (7.59)$$

Note that k_b and k_c cancel out in the process of solution. Substituting Eq. (7.59) into Eqs. (7.45) and (7.54) results in the previously obtained Eqs. (7.39) and (7.40), respectively. Therefore, under the assumption of a steady state, we obtained the same set of solutions as for equilibrium conditions. An equilibrium state for reaction (e) is in turn equivalent to r_e = 0. Substituting r_e = 0 into Eqs. (7.47) and (7.48) leads to r_b = 0 and r_c = 0. Thus, if reaction (e) is in equilibrium, and concentrations of OH* and O* are set to be steady, reactions (b)

Table 7.3. Binding energy BE (kJ mol^{-1}) per adsorbate for atomic H, atomic O, OH and H_2O at various coverages on a four-layer slab model of (2x3) PdZn(111.)[a]

Coverage	1/6	1/3	1/2	2/3	5/6	1
H	29	28	24	9	0	-3
O	143	126	97	55	22	1
OH	293	292	288	269	250	230
H_2O	20	44	41	49	45	32

[a] BE values are calculated with respect to gas-phase H_2 and O_2, i.e. BE = ½ E_{X2} + E_{sub} – $E_{X/sub}$, where X = H, O. Only binding energies of the most stable structures are considered.

and (c) have to be in equilibrium too, leading us back to the same case where we assumed that reactions (a) to (d) were all in equilibrium.

The above results have to be taken with due caution as they are based on a thermodynamic analysis and a kinetic modeling where the effects of carbon containing co-reactants have been ignored. Let us compared our results with those reported for methanol synthesis on Cu(111) surface, at T = 500 K and a total pressure of ~2 atm [122]. In that microkinetic study, the model parameters had been obtained from experimental gas-phase thermodynamics (e.g. vibrational frequencies of adsorbates and gas phase reaction energies) and surface science studies (e.g. activation energies and pre-exponential constants), and the surface coverage of the adsorbates was calculated by fitting the overall rate equation to experimental data. Just like in the present work, reactions (a), (d) and (e) had been assumed to be fast to reach equilibrium, while reactions (b), (c) and other surface reactions involving C-species were considered to be slow. Although the effects of carbon containing co-reactants are absent from our model, we would like to compare the results of our modeling with the microkinetic study [122]. The reported gas composition of the reaction mixture for methanol synthesis at total pressure of ~2 atm, H_2:CO_2:CO:H_2O:CH_3OH = 89.49:4.49:5.49:0.51:0.02 [122], should be similar to the final composition of MSR except for the higher partial pressure values of H_2 and CO in the methanol synthesis reaction due to the different initial composition of the reactants, i.e. in a methanol synthesis reaction only H_2, CO and CO_2 are initially present whereas H_2O and CH_3OH are initially present, for MSR. The microkinetic modeling study [122] predicted that empty sites were the most abundant ones (surface coverage ~0.9), while the surface coverage of the adsorbates H, O,

OH, and H_2O were ~0.1, ~10^{-6}, ~10^{-3} and ~10^{-5}, respectively. Our calculations using an equilibrium model above with p_{H2} = 1.79 atm, p_{H2O} = 0.01 atm and T = 500 K give $\theta_* = 9.96\times10^{-1}$, $\theta_H = 3.95\times10^{-3}$, $\theta_O = 9.11\times10^{-10}$, $\theta_{OH} = 2.97\times10^{-5}$, $\theta_{H2O} = 1.49\times10^{-7}$.

Our results are in fair agreement with those obtained in the previous microkinetic study [122]. In general, both models predict that the metal surface is essentially free from adsorbates. We note that our predicted surface coverages of adsorbates are lower by 10^{-2} compared to those predicted by the microkinetic modeling of methanol synthesis. In our kinetic modeling, we have assumed that all elementary reactions are in equilibrium, which may not be the case under actual reaction conditions.

Recall that we obtained all our adsorbates binding energies from models with assumed surface coverage of 1/4. In fact, the binding energies of the adsorbates may vary at high surface coverage which may also affect the model. Hence, the implicit assumption of constant binding energies may also present a limitation of our model which we will discuss in more detail below in the following section.

7.4.5 Factors that Alter the Surface Energy Plots and Kinetics Modeling

Thus far, we have discussed the surface energy plots calculated for a fixed surface coverage of 1/4. Here, we would like to explore how the surface coverage affects the surface free energy plots. First, we take Eq. (7.30) and rearrange some of the terms using reaction R1 on PdZn(111) as an example.

$$\begin{aligned}\gamma'(T,p_{H2}) &= (E_{H/PdZn} + F^{vib}_{H/PdZn}(T) - E^{PdZn}_{bulk} \\ &\quad - \sum_i N_{H2}[e_{H2} + f^{vib}_{H2}(0,0) + \tilde{\mu}_{H2}(T,p_{H2})])/A \\ &= ([E_{H/PdZn} - \sum_i N_{H2}e^{el}_{H2} - E^{PdZn}_{bulk} - 2A^*\gamma^{cl}] + 2A^*\gamma^{cl} \\ &\quad + F^{vib}_{H/PdZn}(T) - \sum_i N_{H2}[f^{vib}_{H2}(0,0) + \tilde{\mu}_{H2}(T,p_{H2})])/A \\ &= (BE_{H/PdZn} + 2A^*\gamma^{cl} + F^{vib}_{H/PdZn}(T) - \sum_i N_{H2}[f^{vib}_{H2}(0,0) + \tilde{\mu}_{H2}(T,p_{H2})])/A\end{aligned} \tag{7.60}$$

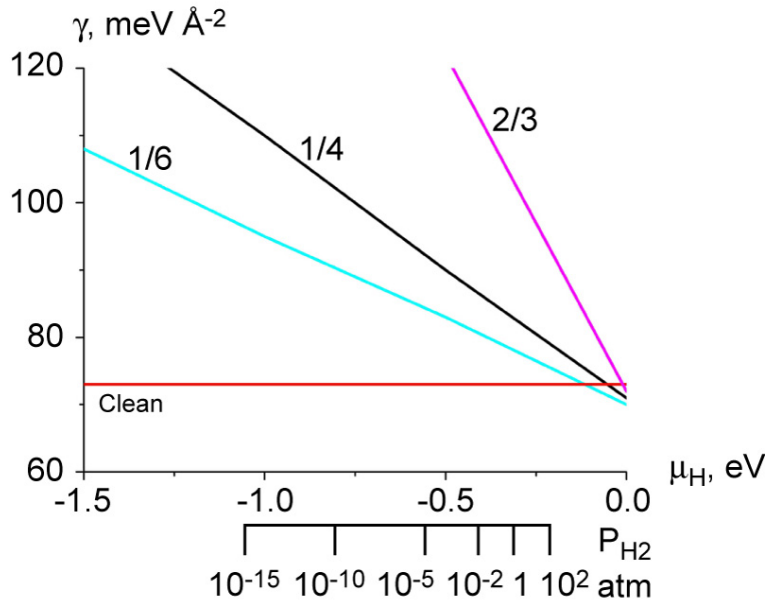

Figure 7.6. Surface energy γ' of R1 (at coverage of 1/6, 1/4 and 2/3) vs. chemical potential $\tilde{\mu}_H$, on the PdZn(111) surface. The p_{H2} scale shown corresponds to $\tilde{\mu}_H$ at T = 500 K.

Here, $BE_{H/PdZn}$ is the binding energy of H on the PdZn(111) surface. With this rearrangement, we can easily identify two key parameters that depend on the surface coverage: (i) the ratio N_{H2}/A, because at high surface coverage, there are more H occupying the same unit area, A, and vice versa, and (ii) $BE_{H/PdZn}$ because at higher coverages adsorbates may undergo lateral interactions which can be attractive or repulsive. In Table 7.3, we show the relationship between surface coverage and binding energy for H, O, OH and H_2O adsorption on PdZn(111) surface. For the species H, O and OH, the binding energy decreases with increased surface coverage and thus manifests repulsive interaction among these adsorbates. In contrast, H_2O exhibits an enhanced binding energy when the coverage is increased to 2/3, due to the formation of a two-dimensional ice like structure [143–146] where H-bonding among H_2O is maximized.

For the H/PdZn(111) system, we illustrate the effect of surface coverage on surface energy plots in Fig. 7.6. One can see that at a lower coverage (1/6), the slope of the curve decreases, which results in a lower surface energy at partial pressures below 10^2 atm compared to the 1/4 coverage. It is also intuitive that at infinitely small coverage, the surface energy curve should approach that of a clean surface. In contrast, for a higher surface coverage (2/3, see Fig. 7.6), the slope of the curve becomes steeper, resulting in a higher

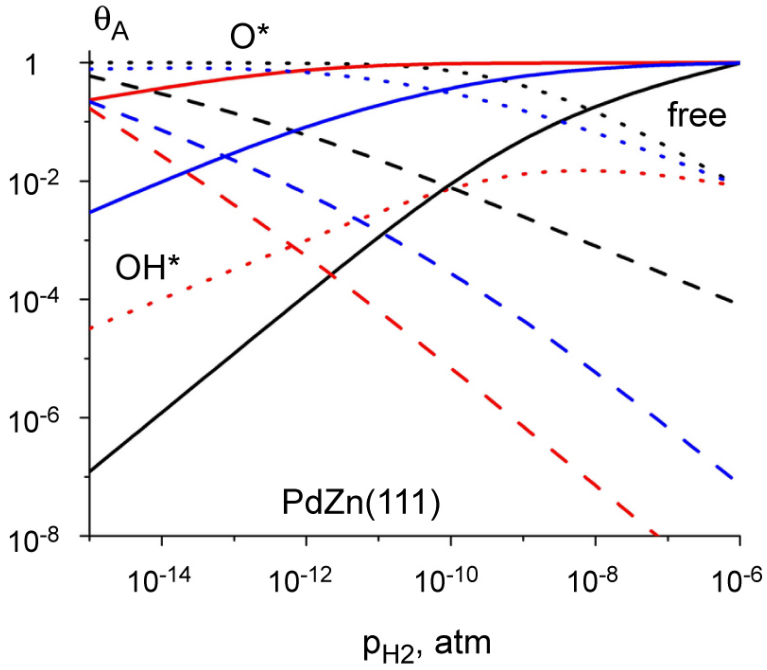

Figure 7.7. Coverage θ_A, A = *, O, OH, as a function of p_{H2} for the reaction $H_2O \rightarrow H_2$ + O* on PdZn(111) at 500 K. Black – original curve as in Fig. 7.5, blue – reaction (c) OH* + * ↔ H* + O* more endothermic by 50 kJ mol^{-1}, red – reaction (b) H_2O* + * ↔ H* + OH* more endothermic by 20 kJ mol^{-1} as well as reaction (c) more endothermic by 50 kJ mol^{-1}. Labeling of lines, dash – O*, dot – OH*, solid – free.

surface energy compared to the 1/4 coverage. This is in agreement with chemical intuition that at lower pressure, the surface coverage of adsorbate would be lower.

Next, we discuss that, as shown in Table 7.3, the binding energies of adsorbates depend on the surface coverage. With the exception of H_2O, binding energies decrease with higher coverage of all adsorbates considered, H, O and OH. These lower binding energies will affect the reaction energies and hence the Gibbs free energies used in our kinetic modeling. This is not a problem for our predictions at high p_{H2}, where the surface is essentially free of adsorbates. However, our results for low values of p_{H2} will be affected where O* and OH* are predicted to occupy more than 1/4 of the surface, because the Gibbs free energies employed for the kinetic modeling are no longer valid.

The decreased binding energies of O and OH render reactions (b) and (c) more endothermic and hence change their Gibbs free energies accordingly. This is illustrated in Fig. 7.7 for PdZn(111) surface by setting ΔE of reaction (c) 50 kJ mol^{-1} higher at the range of $p_{H2} = 10^{-15}$ to 10^{-9} where full O* coverage is predicted (see Fig. 7.7, blue lines). We note that, compared to Fig. 7.5, the effect of a reduced O binding energy is a reduced O* coverage and an increased OH* coverage. One might have anticipated these changes

because reaction (c) is now suppressed and therefore OH* is accumulated on the surface. Another difference is that the surface becomes essentially adsorbate-free already at p_{H2} greater than 10^{-10} atm, instead of 10^{-9} atm previously. Next, we explore the additional effect of a reduced OH binding energy by assuming ΔE of reaction (b) to be 20 kJ mol^{-1} higher (see Fig. 7.7, red lines). As a result, the transition point to an adsorbate-free surface moves to $p_{H2} = 10^{-14}$ atm.

Finally, we turn to the role of surface defects, such as steps, in the formation of adsorbed hydroxyl groups. Based on surface energy calculations, the (111) surface has been identified a the most stable one for PdZn alloy; the surface energy was calculated at 73 meV Å^{-2}. For other surfaces, the calculated values were larger, e.g. 77 meV Å^{-2} for (100) and 98 meV Å^{-2} for (110) [50]. For the stepped surface PdZn(221) we had calculated binding energies of adsorbates to be within ~30 kJ mol^{-1} of the corresponding values for the compact surfaces (111) and (100) (see Chapter 5). Slightly different surface energies of clean surfaces and adsorbates binding energies do not qualitatively change the conclusions drawn from surface energy curves, as was illustrated by the comparison of PdZn(111) and Cu(111) surfaces (Fig. 7.2 and 7.3). Therefore, we expect relatively similar thermodynamic results for the crystalline surfaces (100), (110) and (221) of PdZn and Cu. However, defect sites may feature lower activation barriers (see Chapter 5). Thus, if the non-uniform activation barrier for H_2O dissociation is lower at these sites, one expects a higher surface coverage for OH under non-equilibrium conditions than predicted by this thermodynamic study. The H_2O dissociation barrier on the stepped surfaces of PdZn and Cu merits further computational studies, which are beyond the scope of this thesis.

7.5 Conclusions

We have studied the adsorption of H, O, OH and H_2O on the surfaces PdZn(111) and Cu(111). On these surfaces, we found dissociative adsorption of H_2 and O_2 to be exothermic and H_2O to be weakly adsorbed. We employed thermodynamic arguments to determine the most likely H_2O related species on PdZn(111) and Cu(111) under steam reforming conditions. H_2O adsorption is not favorable on the surfaces at 500 K and p_{H2O} = 1 atm due to the low H_2O binding energy. Atomic hydrogen adsorption is also not favorable at 500 K and p_{H2} = 1 atm, consistent with the experimental observation that H_2 is desorbed

from the catalyst surface under MSR conditions. In contrast, the phase O/PdZn(111) is stable at low values of p_{O2} (10^{-15} atm) and 500 K, due to the high exothermic dissociative adsorption energy (-312 kJ mol^{-1}). Invoking arguments based on thermodynamic principles, we concluded that on PdZn(111) (Cu(111)) a stable oxygen covered surface is favorable at low values of p_{H2}, less than 10^{-15} atm. This oxygen phase is subsequently transformed to an OH phase before an H_2O phase forms at p_{H2} greater than 0.1 atm (2 atm for Cu). The H_2O formed then desorbs from the surface under MSR conditions, as manifested by $\eta < 0$ for Eq. R3 at $p_{H2O} \sim 1$ atm and T = 500 K, rendering H_2O adsorption unfavorable.

Our modeling of coupled equilibria on the surfaces PdZn(111) and Cu(111) is in qualitative agreement with the thermodynamics study of individual equilibria. From the analysis of the coupled equilibria, we found that, when p_{H2} is less than 10^{-9} atm (10^{-8} atm for Cu), O* is the dominating species on PdZn(111) and Cu(111) (coverage of ~1). Both surfaces are essentially adsorbate-free when p_{H2} is greater than 10^{-8} atm. At p_{H2} greater than 10^{-8} atm, the O phase is transformed to a OH phase with surface coverage of $\sim 10^{-3}$ (10^{-1} for Cu); at p_{H2} greater than 10^{-4} atm, the OH* surface coverage is reduced to $\sim 10^{-5}$ ($\sim 10^{-3}$ for Cu).

Finally, we are not able to rule out surface O and OH as possible intermediate species involved in H-abstraction reactions studied in earlier chapters; this topic merits further computational study. Nevertheless, our earlier findings regarding methoxide and formaldehyde decomposition on clean surfaces are still relevant, because when the MSR reaction reaches a steady state, i.e. at $p_{H2} = \sim 1$ atm, one expects most of the surface sites to be free and this is the regime where the experimental reaction rates have been measured [151]. Besides, our calculated activation energies for methoxide C-H bond cleavage agree well with those reported in experimental works (see Section 5.4). As long as this reaction step is the rate determining, the role of OH in these reactions can be assumed to be minor. However, the main change in the products formation due to H_2O in the system is the formation of CO_2. One expects surface OH (being the dominating O containing adsorbate on the surface) to serve as oxygen source of the latter reaction involving carbon containing methanol derivatives.

Chapter 8

Summary

Methanol steam reforming to H_2 and CO_2, catalyzed by Pd/ZnO, is a potential hydrogen source for fuel cells, in particular in pollution-free vehicles. Thus, strong efforts are currently made to achieve an efficient in situ conversion of methanol to hydrogen. The commonly used catalyst for this reaction, Cu/ZnO, is not stable at elevated temperatures because of metal sintering. The novel Pd/ZnO catalysts featuring enhanced thermal stability have been suggested as favorable alternative; their catalytic activity has been assigned to the PdZn alloy component. Methanol steam reforming is believed to begin with the formation of adsorbed methoxide species, CH_3O, which decompose further. Two reaction pathways are possible for the decomposition: (*i*) C-H bond breaking that leads to the formation of a formaldehyde, CH_2O, intermediate, and (*ii*) C-O bond scission which results in stable adsorbed methyl, CH_3, species. A detailed understanding of these two decomposition process on Pd/ZnO catalyst is necessary to rationalize the activity and selectivity of this catalyst, for which C-H bond breaking of methoxide is considered to be the rate-determining step of methanol steam reforming.

Fuel cells currently used in vehicles are very sensitive to poisons, especially to carbon monoxide, which even at low levels (ppm) has a detrimental effect on the performance of fuel cell. Methanol dehydrogenation reaction has been reported to be responsible for the production of carbon monoxide on Pd/ZnO catalyst. Therefore, it is of key importance to understand in detail methanol dehydrogenation to provide guiding principles for designing and producing new, more efficient steam reforming catalysts that do not promote formaldehyde decomposition resulting in the formation of undesirable carbon monoxide.

On Cu/ZnO and Pd/ZnO catalysts, H_2 and CO_2 are the major products of methanol steam reforming, in contrast to metallic Pd catalyst, on which H_2 and CO are mainly formed. These differences in the reaction mechanism are assigned to the reaction of formaldehyde with water related species on Cu/ZnO and Pd/ZnO catalysts. However, the type of H_2O related species on Cu based catalysts has not yet been established convincingly due to conflicting experimental reports. For Pd/ZnO catalysts, it has not been studied at all. Therefore, it is important to define the type of H_2O related species present on the surface of Pd/ZnO catalysts during methanol steam reforming reactions.

To address the problems just outlined, we performed density functional calculations using the plane-wave program, Vienna *ab initio* simulation package VASP. We chose the GGA exchange-correlation functional PW91. The interaction between atomic cores and electrons was described by the projector augmented wave (PAW) method. For integrations over the Brillouin zone, we combined (5×5×1) Monkhorst-Pack grids with a generalized Gaussian smearing technique. We adopted an energy cut-off of 400 eV throughout. All atomic coordinates of the adsorbates were optimized until the force acting on each atom became less than 0.1 eV/nm. For adsorption and reaction studies, the substrates were represented by four-layer slabs consisting of four atoms per layer for the (111) and (100) surfaces and eight atoms per layer for the (221) surface; these models enabled us to consider surface coverages as low as 1/4 for the (111) and (100) surfaces and 1/8 for the (221) surface. A vacuum spacing of ~1 nm was adopted to separate the periodically repeated slabs. Adsorbates were positioned on one side of each slab.

First, we dealt with methoxide decomposition on the compact (111) surfaces of Pd, Cu and PdZn. To this end, we carried out a comparative periodic slab model study on the adsorption of a series of species C, H, O, CO, CH_3, CH_2O and CH_3O that are pertinent to methanol decomposition on Pd(111), Cu(111) and PdZn(111). We found that the adsorption energies of these species on PdZn(111) are close to the corresponding values on Cu(111), implying that the reactivity of a bimetallic PdZn substrate is similar to that of monometallic Cu.

We addressed two conceivable reaction steps of the initial stage of methoxide decomposition, mediated by the mono- and bimetallic substrates mentioned above, and we characterized computationally both thermodynamics and kinetic parameters of these elementary processes. Calculated activation energies showed that C-H bond cleavage is

favored over C-O bond breaking in all cases studied, in line with the stronger C-O bonding. Due to the weaker interaction of CH_3O species with a Pd(111) substrate compared to PdZn(111) and Cu(111), the energy barriers for both C-H and C-O bond cleavage on Pd(111) are much lower than on the other substrates. Calculated energy barriers and reaction energies indicated that dehydrogenation of CH_3O to CH_2O is a very favorable process on Pd(111). However, hydrogen abstraction from adsorbed methoxide moieties to formaldehyde on PdZn(111) and Cu(111) was predicted to be slow because of high activation barriers and endothermic reaction conditions.

To understand how the surface morphology affects the surface reactions, we quantified the adsorption properties of regular (100) facets of the PdZn alloy with respect to the species involved in the initial phase of methanol decomposition (H, O, CH_2O, CH_3, and CH_3O) and characterized the transition state structures for both C-H and C-O bond breaking reactions of methoxide. The binding energies of these adsorbates (except atomic H) were calculated somewhat larger on the (100) surface than on the (111) surface. The transition state structures for C-H and C-O bond breaking on PdZn(100) are similar to those on the (111) surface. However, thermodynamically both reactions become slightly less favorable on the (100) surface because of the calculated relative stabilization of the reactant CH_3O on PdZn(100). Our results for the regular (111) and (100) surfaces of PdZn alloy show that C-H bond cleavage of CH_3O is more facile than C-O dissociation. However, the calculated activation energies indicate that the formation of formaldehyde from CH_3O via C-H breaking is slow on both PdZn(100) and PdZn(111) surfaces.

Next, we investigated the decomposition of methoxide on the stepped surface PdZn(221). The most favorable adsorption complexes involve step-edge atoms, consistent with the higher reactivity of low-coordinated atoms forming a step. The binding energies on substrate models with Pd, $(221)^{Pd}$ and Zn, $(221)^{Zn}$ steps exhibit an obvious trend: species preferring Pd-dominated sites feature the strongest binding on the Pd-terminated steps of $(221)^{Pd}$, while for adsorbates favoring Zn-dominated sites the adsorption interaction is the strongest on the Zn-terminated steps of $(221)^{Zn}$.

Compared to the flat PdZn surfaces, the activation energies for C-H and C-O bond cleavage on the $(221)^{Zn}$ surface do not decrease, because methoxide interacts stronger with the Zn step edge. On the other hand, the reaction barrier for C-H bond breaking on the $(221)^{Pd}$ surface is greatly reduced from ~90 kJ mol^{-1} to ~50 kJ mol^{-1} on flat surfaces. This crucial

activation barrier is lowered for two synergetic reasons: the reactant CH_3O interacts weaker with the catalyst while the product CH_2O binds to it stronger. Concomitantly, the calculated reaction rate constant for C-H cleavage is increased on $(221)^{Pd}$ by a factor of 10^8, reaching $\sim 10^4$–10^5 s^{-1} at 300 K.

Our calculated values for the activation barriers of C-H bond breaking on PdZn(111) (93 kJ mol^{-1}), PdZn(100) (90 kJ mol^{-1}), PdZn(221) (49 kJ mol^{-1}), and Cu(111) (112 kJ mol^{-1}) surfaces are in agreement with the reported apparent activation barrier of 95 kJ mol^{-1} on Pd/ZnO catalyst [116], and those on various commercial Cu/ZnO based catalysts, ranging from 74 to 122 kJ mol^{-1} [18]. Therefore, methoxide C-H bond breaking is likely to be the rate-determining step of the methanol steam reforming reaction on Cu and PdZn based catalysts. The wide range of reported apparent activation barriers for different commercial Cu based catalysts is probably an indication of the degree of defects (or surface irregularities) present due to different preparation methods employed.

For an improved understanding of methanol decomposition to carbon monoxide, we carried out a comparative computational study of formaldehyde dehydrogenation and formyl dehydrogenation on the planar surfaces Pd(111), Cu(111) and PdZn(111). We found that formyl binds least strongly to Cu(111) (BE = ~125 kJ mol^{-1}) and most strongly to Pd(111) (BE = ~210 kJ mol^{-1}). Like for all other adsorbates in this study, the binding energy of formyl on PdZn(111), ~160 kJ mol^{-1}, falls between those on Pd(111) and Cu(111). The calculated activation energies showed that formaldehyde dehydrogenation should be favorable on Pd(111) and unfavorable on the (111) surfaces of Cu and PdZn. The small amount of carbon monoxide observed experimentally during methanol decomposition on PdZn alloy can be assigned to formaldehyde dehydrogenation at metallic Pd site. This is in line with the experimentally observed high fraction of carbon monoxide produced during oxidative methanol steam reforming when the Pd loading of ZnO catalyst is outside the range of 5–37.5 %. One can rationalize the experimental finding by metallic Pd to be present at higher Pd loading and the abundance of defect sites at lower Pd loading.

To characterize the role of H_2O related species in the decomposition of methanol, we studied the adsorption of H, O, OH and H_2O on the surfaces PdZn(111) and Cu(111). We found that dissociative adsorption of H_2 (~20 kJ mol^{-1}/H atom) and O_2 (~160 kJ mol^{-1}/O atom) is exothermic, OH is bound to the surface by ~ 300 kJ mol^{-1} and H_2O is weakly adsorbed, BE = ~20 kJ mol^{-1}.

We employed thermodynamic arguments and kinetic modeling to investigate the most likely surface composition on PdZn(111) and Cu(111) under steam reforming conditions, i.e. at temperature near 500 K and H_2O partial pressure of ~1 atm. Studying individual equilibria by computational thermodynamics, we find that H_2O adsorption is not favorable on either catalyst surface under these conditions because the adsorption energy of H_2O is very small. Dissociative H_2 adsorption is also unfavorable at 500 K and a partial pressure of hydrogen p_{H2} = 1 atm, consistent with the experimental observation that H_2 is desorbed from both catalysts under methanol steam reforming conditions. From a thermodynamic study of individual equilibria, at p_{H2} below 10^{-15} atm, a stable oxygen covered surface of PdZn (Cu) is most favorable. For 10^{-15} atm < p_{H2} < 10^{-1} atm on PdZn (and 10^{-15} atm < p_{H2} < 2 atm on Cu), the OH phase is preferred and at higher values of the partial pressure of hydrogen (> 10^{-1} atm for PdZn and > 2 atm for Cu), the OH phase is converted to H_2O, which subsequently desorbs from the surface. However, this approach provides only qualitative arguments because coupled reactions are not taken into consideration and hence such a model does not represent the complex situation on the surface under experimental conditions.

Our kinetic modeling of coupled equilibria on PdZn(111) and Cu(111) surfaces is in qualitative agreement with the thermodynamics study of individual equilibria. On PdZn(111), at 500 K and p_{H2O} = 1 atm, when p_{H2} is less than 10^{-9} atm, O* was determined to be the dominating species (coverage of ~1). Both surfaces are essentially adsorbate-free when p_{H2} is greater than 10^{-8} atm. At p_{H2} greater than 10^{-8} atm, an O phase at the surface is transformed to an OH phase with a surface coverage of ~10^{-3}; at p_{H2} greater than 10^{-4} atm, the OH* surface coverage is reduced to ~10^{-5}. While a similar trend is found on Cu(111), the transition of adsorbates coverage is more distinct compared with PdZn(111). When p_{H2} is less than 10^{-8} atm, O* dominates the surface; OH* dominates the adsorbates on the surface with a coverage of ~0.1 when p_{H2} is between 10^{-8} atm and 10^{-4} atm. The surface is essentially adsorbate-free when p_{H2} is greater then 10^{-4} (OH* coverage ~10^{-3}). We found that on both surfaces, when methanol steam reforming reaches steady state where p_{H2} is relatively high, OH* is the most abundant O containing adsorbate related to H_2O on the surface. Thus, one expects OH* to serve as an oxygen source for the further reactions involving carbon containing methanol derivatives for the formation of CO_2 under methanol steam reforming conditions.

In conclusion, in this thesis, we have achieved the following objectives set out at the beginning of the study.

(i) We clarified the effects of surface morphology on methoxide C-H and C-O bond cleavage on the (111), (100) and (221) surfaces of PdZn alloy and we contributed to the understanding of the "structural" gap between surface science models and "real" experimental catalysts of methanol steam reforming;

(ii) We characterized computationally formaldehyde dehydrogenation on the (111) surfaces of Pd, Cu and PdZn characterized and we identified conditions that would minimize the production of the undesirable CO on PdZn alloy; and

(iii) We addressed the "pressure" gap by invoking thermodynamics and kinetic arguments to find the most stable H_2O related species on PdZn(111) and Cu(111) surfaces.

Although this thesis has answered a series of questions which we have intended to address, open problems remain because methanol steam reforming is a complex process. Several emerged from our work and merit further computational investigation, among them: (i) the effects of surface defects on formaldehyde dehydrogenation; (ii) the effects of surface defects on water dissociation; (iii) the effects of adsorbed OH on the binding energies and potential site-blocking affecting reactions of other surface intermediates; and (iv) the reactions that involve adsorbed OH in the methanol steam reforming process.

Appendix A

Supplementary Material for Methoxide Decomposition on (111) Surfaces of Pd, Cu, and PdZn

Table A1. Unit cell parameters of Pd(111), PdZn(111) and Cu(111)

	Pd(111)	PdZn(111)	Cu(111)
a = b, Å	5.592	5.354	5.131
c, Å	22.828	22.167	20.946
$\alpha = \beta$, degree	90.000	90.000	90.000
γ, degree	60.000	66.438	60.000

Table A2. Cartesian coordinates (Å) of the substrate atoms and the resulting total energy (eV)

	PdZn (111)			Pd (111)			Cu (111)		
	x	y	z	x	y	z	x	y	z
M_1	0.000	0.000	13.300	0.000	0.000	13.697	0.000	0.000	10.473
M_1	3.747	2.454	13.300	4.194	2.421	13.697	2.565	0.000	10.473
M_1	1.607	1.052	15.517	1.398	2.421	13.697	1.283	2.222	10.473
M_1	5.354	3.506	15.517	2.796	0.000	13.697	3.848	2.222	10.473
M_1	3.214	2.105	17.733	1.398	0.807	15.980	1.283	0.741	12.568
M_1	6.961	4.558	17.733	5.592	3.228	15.980	3.848	0.741	12.568
M_1	4.821	3.157	19.950	2.796	3.228	15.980	2.565	2.962	12.568
M_1	1.074	0.703	19.950	4.194	0.807	15.980	5.131	2.962	12.568
M_2	1.070	2.454	13.300	2.796	1.614	18.263	2.565	1.481	14.662
M_2	2.677	0.000	13.300	6.990	4.036	18.263	5.131	1.481	14.662
M_2	2.677	3.506	15.517	4.194	4.036	18.263	3.848	3.703	14.662
M_2	4.284	1.052	15.517	5.592	1.614	18.263	6.413	3.703	14.662
M_2	4.284	4.558	17.733	2.796	0.000	20.546	0.000	0.000	16.757
M_2	5.891	2.105	17.733	1.398	2.421	20.546	2.565	0.000	16.757
M_2	3.750	0.703	19.950	4.194	2.421	20.546	1.283	2.222	16.757
M_2	2.144	3.157	19.950	0.000	0.000	20.546	3.848	2.222	16.757
Total Energy			-55.717			-79.150			-55.769

M_1 = Pd, M_2 = Zn on PdZn(111); $M_1 = M_2$ = Pd or Cu on Pd(111) or Cu(111), respectively.

Table A3. Total energy (eV) of atoms and molecules in vacuum

Species	C	O	H	CO	CH_3	CH_3O	CH_2O
Total energy	-1.389	-1.810	-1.119	-14.851	-18.183	-24.477	-22.228

In Table A4 to A12, we provide the Cartesian coordinates (in Å) and the total energy (in eV) of the substrate with adsorbed species. For the adsorption sites on PdZn(111), refer to Fig. 3.1. On Pd(111) and Cu(111), site B^{Pd2} denotes a bridge site, F^{Pd2Zn} denotes an fcc site, H^{Pd2Zn} denotes an hcp site, T^{Pd} denotes a top site, and TBT^{Pd2} denotes a top-bridge-top site.

Table A4A. Atomic adsorption H, C and O on M(111)

Sites		PdZn			Pd			Cu		
		x	y	z	x	y	z	x	y	z
B^{Pd2}	H	2.508	3.396	12.357	3.495	1.211	12.697	3.207	1.111	9.398
B_1^{PdZn}		-1.246	0.937	12.356						
B_2^{PdZn}		3.899	0.852	12.300						
B^{Zn2}		2.503	1.639	12.319						
F^{Pd2Zn}		3.177	3.834	12.321	2.796	1.614	12.858	2.565	1.481	9.563
F^{PdZn2}		2.741	1.795	12.144						
H^{Pd2Zn}		2.473	3.373	12.361	1.398	0.807	12.858	1.283	0.741	9.559
H^{PdZn2}		0.781	0.511	11.962						
T^{Pd}		0.000	0.000	11.704	4.194	2.421	12.150	3.848	2.221	8.957
T^{Zn}		1.070	2.454	11.716						
B^{Pd2}	C	2.946	3.682	12.089	2.094	1.209	12.500	1.283	0.000	9.224
B_1^{PdZn}		1.257	-0.004	11.942						
B_2^{PdZn}		3.246	1.290	11.942						
B^{Zn2}		1.868	1.223	12.112						
F^{Pd2Zn}		3.303	3.916	12.140	2.796	1.614	12.691	2.565	1.481	9.374
F^{PdZn2}		2.456	1.608	12.162						
H^{Pd2Zn}		2.549	3.422	12.155	1.398	0.807	12.693	1.283	0.741	9.377
H^{PdZn2}		1.287	0.843	12.158						
T^{Pd}		0.001	0.001	11.499	0.000	0.000	11.965	0.000	0.000	8.746
T^{Zn}		1.070	2.454	11.423						
B^{Pd2}	O	2.939	3.677	11.891	1.398	0.000	12.341	1.283	0.000	9.176
B_1^{PdZn}		1.558	1.021	12.129						
B_2^{PdZn}		2.311	1.543	12.124						
B^{Zn2}		2.254	1.476	12.138						
F^{Pd2Zn}		3.643	4.138	12.018	2.796	1.614	12.516	2.565	1.481	9.304
F^{PdZn2}		2.258	1.479	12.129						
H^{Pd2Zn}		2.224	3.210	12.008	1.398	0.807	12.498	1.283	0.741	9.282
H^{PdZn2}		1.560	1.022	12.122						
T^{Pd}		-0.002	-0.001	11.415	0.000	0.000	11.882	3.848	2.222	8.748
T^{Zn}		1.079	2.460	11.525						

Table A4B. Total energy of atomic adsorption H, C and O on M(111)

Sites		PdZn	Pd	Cu
B^{Pd2}	H	-59.411	-82.956	-59.220
B_1^{PdZn}		-59.411		
B_2^{PdZn}		-59.364		
B^{Zn2}		-59.096		
F^{Pd2Zn}		-59.341	-83.109	-59.350
F^{PdZn2}		-59.161		
H^{Pd2Zn}		-59.411	-83.044	-59.348
H^{PdZn2}		-59.007		
T^{Pd}		-59.060	-82.584	-58.789
T^{Zn}		-58.349		
B^{Pd2}	C	-61.728	-86.455	-61.529
B_1^{PdZn}		-61.047		
B_2^{PdZn}		-61.000		
B^{Zn2}		-60.950		
F^{Pd2Zn}		-61.741	-87.118	-62.066
F^{PdZn2}		-61.386		
H^{Pd2Zn}		-61.720	-87.190	-61.988
H^{PdZn2}		-61.418		
T^{Pd}		-60.379	-84.755	-60.074
T^{Zn}		-59.072		
B^{Pd2}	O	-61.009	-84.780	-61.956
B_1^{PdZn}		-62.043		
B_2^{PdZn}		-62.156		
B^{Zn2}		-62.179		
F^{Pd2Zn}		-61.519	-85.324	-62.400
F^{PdZn2}		-62.178		
H^{Pd2Zn}		-61.623	-85.115	-62.294
H^{PdZn2}		-62.043		
T^{Pd}		-59.993	-83.633	-60.628
T^{Zn}		-60.361		

Table A5A. CO/M(111)

Sites		PdZn			Pd			Cu		
		x	y	z	x	y	z	x	y	z
B^{Pd2}	C	2.942	3.680	11.767	1.398	-0.007	12.262	1.283	0.000	8.985
	O	2.944	3.681	10.591	1.398	0.003	11.084	1.283	0.000	7.812
B_1^{PdZn}	C	0.027	0.502	11.419						
	O	0.095	0.793	10.298						
B_2^{PdZn}	C	3.537	1.722	11.519						
	O	3.317	1.269	10.471						
B^{Zn2}	C	1.864	1.221	11.613						
	O	1.880	1.231	10.445						
F^{Pd2Zn}	C	3.059	3.756	11.804	2.796	1.614	12.403	2.565	1.481	9.053
	O	3.137	3.808	10.635	2.796	1.614	11.216	2.565	1.481	7.873
F^{PdZn2}	C	3.685	2.413	11.349						
	O	3.666	2.401	10.192						
H^{Pd2Zn}	C	2.579	3.442	11.813	1.398	0.807	12.361	1.283	0.741	9.001
	O	2.398	3.324	10.656	1.398	0.807	11.176	1.283	0.741	7.823
H^{PdZn2}	C	7.381	4.833	11.361						
	O	7.289	4.773	10.209						
T^{Pd}	C	-0.008	-0.005	11.356	0.000	0.000	11.831	0.000	0.000	8.595
	O	0.001	0.001	10.199	0.000	0.000	10.676	0.000	0.000	7.435
T^{Zn}	C	1.068	2.452	11.137						
	O	1.071	2.455	9.985						

Table A5B. Total energy of CO/M(111)

Sites	PdZn	Pd	Cu
B^{Pd2}	-71.556	-95.703	-71.408
B_1^{PdZn}	-71.506		
B_2^{PdZn}	-71.439		
B^{Zn2}	-70.601		
F^{Pd2Zn}	-71.536	-95.865	-71.481
F^{PdZn2}	-71.569		
H^{Pd2Zn}	-71.481	-95.846	-71.453
H^{PdZn2}	-71.569		
T^{Pd}	-71.569	-95.291	-71.328
T^{Zn}	-70.705		

Table A6A. CH_2O/M(111)

Sites		PdZn			Pd			Cu		
		x	y	z	x	y	z	x	y	z
TBT^{Pd2}	H	2.707	2.251	10.749	2.663	0.651	11.217	3.105	3.165	7.104
	H	4.371	3.107	10.896	2.379	-1.176	11.511	3.105	1.271	7.104
	C	3.270	3.170	11.000	2.042	-0.130	11.689	3.156	2.222	7.758
	O	2.691	4.291	11.079	0.746	0.091	11.730	1.927	2.222	7.741
TBT^{PdZn}	H	3.025	2.550	10.681						
	H	4.887	2.510	10.879						
	C	3.928	3.016	11.128						
	O	3.920	4.297	11.349						

Table A6B. Total energy of CH_2O/M(111)

Sites	PdZn	Pd	Cu
TBT^{Pd2}	-78.049	-101.822	-78.102
TBT^{PdZn}	-78.190		

Table A7A. CH_3/M(111)

Sites		PdZn			Pd			Cu		
		x	y	z	x	y	z	x	y	z
B^{Pd2}	H	2.935	4.693	11.030	4.522	1.155	11.503	4.218	1.081	8.223
	H	2.036	3.153	10.915	2.970	0.286	11.566	2.689	0.206	8.288
	H	3.817	3.165	11.038	2.945	2.062	11.467	2.672	1.971	8.228
	C	2.884	3.649	11.379	3.495	1.211	11.889	3.207	1.111	8.659
B_1^{PdZn}	H	0.203	1.145	10.826						
	H	-0.806	-0.329	10.700						
	H	0.988	-0.462	10.807						
	C	0.104	0.102	11.135						
B_2^{PdZn}	H	3.222	2.260	10.922						
	H	2.363	0.743	11.149						
	H	4.137	0.716	10.920						
	C	3.307	1.264	11.383						
B^{Zn2}	H	1.874	2.260	10.992						
	H	0.973	0.707	11.019						
	H	2.769	0.711	10.992						
	C	1.879	1.230	11.374						
F^{Pd2Zn}	H	3.463	5.035	11.021	1.902	2.130	11.574	3.493	1.905	8.349
	H	2.554	3.510	10.840	2.796	0.582	11.574	2.469	0.466	8.349
	H	4.328	3.490	11.026	3.690	2.130	11.574	1.735	2.072	8.349
	C	3.399	3.986	11.347	2.796	1.614	11.980	2.565	1.451	8.778
F^{PdZn2}	H	3.246	3.170	10.775						
	H	2.350	1.635	10.979						
	H	4.130	1.603	10.802						
	C	3.283	2.165	11.210						
H^{Pd2Zn}	H	2.399	4.352	11.081	1.398	1.838	11.544	6.016	2.456	8.341
	H	1.514	2.806	11.045	0.506	0.292	11.544	4.251	2.446	8.342
	H	3.294	2.819	11.085	2.290	0.292	11.544	5.128	3.983	8.343
	C	2.388	3.319	11.474	1.398	0.807	11.952	5.131	2.962	8.773
H^{PdZn2}	H	0.697	1.488	10.996						
	H	7.354	4.869	10.607						
	H	3.748	4.873	10.962						
	C	0.641	0.412	11.227						
T^{Pd}	H	7.491	5.941	10.791	5.244	2.415	11.312	4.878	2.220	8.059
	H	6.600	4.391	10.768	3.664	1.519	11.304	3.332	1.330	8.059
	H	8.388	4.388	10.792	3.682	3.338	11.311	3.334	3.114	8.059
	C	7.487	4.903	11.142	4.194	2.421	11.633	3.848	2.222	8.441
T^{Zn}	H	6.423	3.489	10.841						
	H	7.669	6.845	10.853						
	H	9.461	6.843	10.843						
	C	6.429	2.457	11.211						

Table A7B. Total energy of CH_3/M(111)

Sites	PdZn	Pd	Cu
B^{Pd2}	-75.157	-98.844	-75.319
B_1^{PdZn}	-75.375		
B_2^{PdZn}	-75.281		
B^{Zn2}	-74.671		
F^{Pd2Zn}	-75.027	-98.909	-75.441
F^{PdZn2}	-75.399		
H^{Pd2Zn}	-75.286	-98.801	-75.417
H^{PdZn2}	-75.260		
T^{Pd}	-75.390	-99.113	-75.266
T^{Zn}	-74.964		

Table A8A. CH_3O/M(111)

Sites		PdZn			Pd			Cu		
		x	y	z	x	y	z	x	y	z
B^{Pd2}	H	2.944	4.715	9.812	2.121	2.233	10.305	3.600	2.221	7.141
	H	2.049	3.164	9.801	1.206	0.760	10.765	2.047	1.329	7.132
	H	3.840	3.163	9.813	2.942	0.638	10.329	2.048	3.114	7.131
	C	2.940	3.679	10.198	2.184	1.264	10.827	2.565	2.222	7.521
	O	2.944	3.681	11.614	2.579	1.490	12.178	2.565	2.222	8.946
B_1^{PdZn}	H	4.435	4.807	10.124						
	H	3.500	3.304	10.333						
	H	5.181	3.223	9.723						
	C	4.505	3.745	10.416						
	O	5.007	3.615	11.751						
B_2^{PdZn}	H	1.562	4.653	9.972						
	H	0.680	3.110	9.808						
	H	2.375	3.129	10.390						
	C	1.411	3.664	10.424						
	O	0.915	3.793	11.767						
B^{Zn2}	H	1.874	2.262	10.015						
	H	0.977	0.709	10.013						
	H	2.770	0.709	10.015						
	C	1.874	1.227	10.391						
	O	1.875	1.228	11.827						
F^{Pd2Zn}	H	2.422	2.621	9.842	3.835	1.614	10.467	3.599	1.480	7.260
	H	1.550	1.081	10.086	2.277	2.515	10.467	2.048	0.587	7.260
	H	3.322	1.075	9.855	2.276	0.714	10.467	2.050	2.377	7.260
	C	2.481	1.624	10.312	2.796	1.614	10.832	2.565	1.481	7.634
	O	2.656	1.738	11.720	2.796	1.614	12.256	2.565	1.481	9.063
F^{PdZn2}	H	2.407	2.604	10.094						
	H	1.510	1.057	9.938						
	H	3.300	1.065	10.086						
	C	2.373	1.554	10.418						
	O	2.247	1.473	11.843						

Table A8A. CH_3O/M(111) continued

Sites		PdZn			Pd			Cu		
		x	y	z	x	y	z	x	y	z
H^{Pd2Zn}	H	1.304	1.884	10.022	1.447	1.838	10.396	6.166	2.964	7.258
	H	0.412	0.345	9.780	0.466	0.339	10.428	4.615	2.065	7.258
	H	2.193	0.332	10.005	2.255	0.235	10.388	4.612	3.858	7.258
	C	1.252	0.819	10.314	1.398	0.809	10.773	5.131	2.962	7.631
	O	1.074	0.702	11.726	1.419	0.814	12.202	5.131	2.962	9.060
H^{PdZn2}	H	1.357	1.918	9.918						
	H	0.477	0.386	10.185						
	H	2.247	0.369	9.937						
	C	1.409	0.924	10.392						
	O	1.615	1.059	11.812						
T^{Pd}	H	7.492	5.936	9.454	0.051	1.031	9.908	4.883	2.221	6.834
	H	6.599	4.391	9.450	-0.926	-0.466	9.916	3.330	1.326	6.834
	H	8.385	4.391	9.454	0.860	-0.570	9.906	3.331	3.118	6.834
	C	7.493	4.907	9.859	0.000	0.000	10.309	3.848	2.222	7.228
	O	7.502	4.913	11.244	0.000	0.000	11.701	3.848	2.222	8.626
T^{Zn}	H	6.424	3.486	9.619						
	H	5.531	1.937	9.620						
	H	7.318	1.937	9.619						
	C	6.426	2.455	10.013						
	O	6.423	2.453	11.416						

Table A8B. Total energy of CH_3O/M(111)

Sites	PdZn	Pd	Cu
B^{Pd2}	-81.835	-105.321	-82.604
B_1^{PdZn}	-82.422		
B_2^{PdZn}	-82.291		
B^{Zn2}	-82.426		
F^{Pd2Zn}	-82.129	-105.308	-82.696
F^{PdZn2}	-82.482		
H^{Pd2Zn}	-82.203	-105.221	-82.683
H^{PdZn2}	-82.379		
T^{Pd}	-81.356	-104.560	-81.978
T^{Zn}	-81.866		

Table A9. $CH_3O \rightarrow CH_2O + H$ (Transition State)

	PdZn			Pd			Cu		
	x	y	z	x	y	z	x	y	z
H	3.203	3.461	11.956	2.307	1.101	12.406	3.652	3.557	9.252
H	5.004	2.783	10.904	2.003	1.021	10.683	3.780	2.126	7.895
H	3.611	3.682	10.054	2.352	-0.652	11.362	3.034	3.813	7.451
C	4.422	3.725	10.806	1.739	0.268	11.449	2.966	2.884	8.077
O	4.957	4.857	11.133	0.436	0.115	11.669	1.760	2.472	8.395
Total energy			-81.313			-104.978			-81.536

Table A10. $CH_3O \rightarrow CH_2O + H$ (Final State)

	PdZn			Pd			Cu		
	x	y	z	x	y	z	x	y	z
H	2.301	3.371	12.395	2.830	1.723	12.922	3.848	3.703	9.568
H	3.498	2.488	10.513	2.628	0.584	11.118	3.704	3.190	7.660
H	5.342	2.389	10.866	2.329	-1.226	11.487	3.697	1.365	7.173
C	4.413	2.999	10.869	1.996	-0.173	11.617	3.109	2.273	7.441
O	4.446	4.236	11.047	0.720	0.068	11.698	1.889	2.265	7.485
Total energy			-81.598			-105.590			-81.691

Table A11. $CH_3O \rightarrow CH_3 + O$ (Transition State)

	PdZn			Pd			Cu		
	x	y	z	x	y	z	x	y	z
H	3.877	3.509	10.355	4.689	3.579	11.514	5.285	1.531	8.217
H	3.014	2.088	11.086	2.894	3.530	11.149	4.305	-0.014	8.125
H	4.728	1.885	10.496	3.977	2.136	10.625	3.650	1.546	7.338
C	3.983	2.571	10.891	3.807	2.958	11.316	4.296	1.076	8.092
O	5.424	3.547	12.004	2.769	1.639	12.421	2.694	1.433	9.222
Total energy			-80.323			-103.809			-80.596

Table A12. $CH_3O \rightarrow CH_3 + O$ (Final State)

	PdZn			Pd			Cu		
	x	y	z	x	y	z	x	y	z
H	3.651	3.430	10.878	0.661	0.896	11.348	6.072	1.813	8.180
H	2.743	1.869	10.819	-0.995	0.141	11.310	5.026	0.402	8.448
H	4.547	1.870	10.879	0.491	-0.913	11.321	4.263	1.976	8.186
C	3.634	2.378	11.187	0.046	0.037	11.635	5.134	1.493	8.628
O	6.028	3.947	12.147	2.800	1.616	12.494	2.559	1.411	9.331
Total energy			-81.624			-105.232			-81.236

Appendix B

Supplementary Material for Methoxide Decomposition on PdZn(100)

Table B1. Unit cell parameters of PdZn(100)

a = b, Å	5.354
c, Å	16.592
$\alpha = \beta$, degree	90.000
γ, degree	78.433

Table B2. Cartesian coordinates (Å) of PdZn(100) substrate atoms and the resulting total energy (eV)

	x	y	z
Pd	0.000	0.000	10.370
Pd	3.214	2.623	10.370
Pd	1.607	1.311	12.444
Pd	4.821	3.934	12.444
Pd	0.000	0.000	14.518
Pd	3.214	2.623	14.518
Pd	1.607	1.311	16.592
Pd	4.821	3.934	16.592
Zn	2.677	0.000	10.370
Zn	0.537	2.623	10.370
Zn	2.144	3.934	12.444
Zn	4.284	1.311	12.444
Zn	2.677	0.000	14.518
Zn	0.537	2.623	14.518
Zn	2.144	3.934	16.592
Zn	4.284	1.311	16.592
Total Energy			-55.125

In Table B3 to B7, we provide the Cartesian coordinates (in Å) and the total energy (in eV) of the PdZn(100) slab with adsorbed species. Refer to Fig. 4.1 for the adsorption sites.

Table B3. Atomic adsorption H and CH_3 on Pd(100).

		T^{Pd}			H^{Pd2Zn}			$4H^{Pd2}$		
		x	y	z	x	y	z	x	y	z
H		0.000	0.000	8.764	1.916	3.748	9.559	2.144	3.934	9.553
Total energy				-58.434			-58.630			-58.629
CH_3	H	2.702	1.723	7.855	5.873	2.608	7.999	5.156	2.023	7.936
	H	2.689	3.520	7.860	5.255	0.947	8.150	4.525	0.372	8.145
	H	4.250	2.623	7.855	4.121	2.336	8.150	3.412	1.736	8.145
	C	3.213	2.623	8.212	5.110	1.985	8.493	4.427	1.428	8.471
Total energy				-74.786			-74.614			-74.426

Table B4. Atomic adsorption O and CH_3O on Pd(100).

		T^{Zn}			H^{PdZn2}			$4H^{Zn2}$		
		x	y	z	x	y	z	x	y	z
O		2.677	0.000	8.604	1.622	1.324	9.361	1.607	1.311	9.351
Total energy				-60.007			-61.686			-61.687
CH_3O	H	4.766	5.203	6.684	3.086	2.518	7.448	2.663	1.338	7.119
	H	3.194	6.057	6.670	2.514	0.896	6.979	1.201	2.375	7.152
	H	3.252	4.268	6.722	1.382	2.284	6.979	1.037	0.596	7.069
	C	3.736	5.191	7.091	2.235	1.824	7.505	1.631	1.421	7.497
	O	3.744	5.228	8.494	1.896	1.547	8.883	1.618	1.358	8.942
Total energy				-81.482			-81.929			-82.024

Table B5. Atomic adsorption CH_2O on Pd(100).

		TBT^{PZ}			TBT^{Pd}			Π		
		x	y	z	x	y	z	x	y	z
CH_2O	H	2.987	3.519	7.929	0.707	4.914	7.764	3.808	3.877	7.872
	H	2.948	1.657	7.854	1.243	5.876	7.900	4.319	2.065	7.844
	C	2.483	2.584	8.219	1.765	4.941	8.099	3.536	2.821	8.046
	O	1.194	2.616	8.393	2.396	3.856	8.304	2.327	2.472	8.180
Total energy				-77.598			-77.508			-77.576

Table B6. $CH_3O \rightarrow CH_2O + H$

	Transition state			Final state		
	x	y	z	x	y	z
H	3.330	1.487	9.062	4.290	1.336	9.682
H	2.781	3.393	8.007	3.015	3.540	7.925
H	2.727	1.704	7.269	2.928	1.678	7.771
C	2.325	2.385	8.038	2.488	2.604	8.187
O	1.074	2.260	8.380	1.213	2.647	8.400
Total energy			-80.920			-81.063

Table B7. $CH_3O \rightarrow CH_3 + O$

	Transition state			Final state		
	x	y	z	x	y	z
H	4.001	2.192	8.171	3.112	2.029	7.903
H	2.615	3.389	7.954	3.070	3.831	7.959
H	2.550	1.749	7.218	4.657	2.978	7.950
C	2.905	2.339	8.049	3.611	2.933	8.274
O	1.708	1.395	9.187	1.489	1.215	9.353
Total energy			-80.295			-81.049

Table B8. Frequencies (cm^{-1}) of initial state (IS), transition state (TS) for C-H and C-O bond breaking of adsorbed methoxy on (100) and (111) surface of PdZn alloy

	(100)			(111)		
	IS	TS^{C-H}	TS^{C-O}	IS	TS^{C-H}	TS^{C-O}
ν_1	3010	2974	3214	3021	2947	3210
ν_2	3000	2900	3095	3001	2862	3141
ν_3	2948	1483	2873	2913	1494	2984
ν_4	1452	1461	1416	1450	1336	1388
ν_5	1447	1278	1374	1445	1247	1364
ν_6	1406	1163	1138	1409	1161	1047
ν_7	1124	1079	775	1132	1039	740
ν_8	1118	746	760	1124	710	646
ν_9	954	601	338	1003	578	355
ν_{10}	238	339	288	255	303	333
ν_{11}	221	209	282	242	190	233
ν_{12}	210	163	133	201	135	184
ν_{13}	151	126	115	163	72	105
ν_{14}	67	63	34	81	33	67
ν_{15}	56	767*i*	534*i*	67	792*i*	507*i*

Appendix C

Supplementary Material for Methoxide Decomposition on PdZn(221)

Table C1. Unit cell parameters of PdZn(221)

a, Å	7.378
b, Å	5.866
c, Å	21.531
$\alpha = \beta = \gamma$, degree	90

Table C2. Cartesian coordinates (Å) of substrate atoms and the resulting total energy (eV)

	$(221)^{Pd}$			$(221)^{Zn}$			Bulk Truncated [a]		
	x	y	z	x	y	z	x	y	z
Pd	0.061	0.000	8.775	2.119	1.467	9.397	0.000	0.000	8.612
Pd	4.165	0.000	10.028	6.319	1.467	10.568	4.272	0.000	9.958
Pd	0.061	2.933	8.775	2.119	4.400	9.397	0.000	2.933	8.612
Pd	4.165	2.933	10.028	6.319	4.400	10.568	4.272	2.933	9.958
Pd	1.148	0.000	11.326	3.334	1.467	11.978	1.166	0.000	11.304
Pd	5.470	0.000	12.662	0.188	1.467	13.326	5.438	0.000	12.649
Pd	1.148	2.933	11.326	3.334	4.400	11.978	1.166	2.933	11.304
Pd	5.470	2.933	12.662	0.188	4.400	13.326	5.438	2.933	12.649
Pd	2.332	0.000	13.995	4.468	1.467	14.668	2.332	0.000	13.995
Pd	6.604	0.000	15.341	1.362	1.467	16.014	6.604	0.000	15.341
Pd	2.332	2.933	13.995	4.468	4.400	14.668	2.332	2.933	13.995
Pd	6.604	2.933	15.341	1.362	4.400	16.014	6.604	2.933	15.341
Pd	3.498	0.000	16.686	5.634	1.467	17.359	3.498	0.000	16.686
Pd	0.392	0.000	18.032	2.528	1.467	18.705	0.392	0.000	18.032
Pd	3.498	2.933	16.686	5.634	4.400	17.359	3.498	2.933	16.686
Pd	0.392	2.933	18.032	2.528	4.400	18.705	0.392	2.933	18.032
Zn	2.158	1.467	9.226	0.105	0.000	8.728	2.136	1.467	9.285
Zn	6.298	1.467	10.567	4.244	0.000	9.860	6.408	1.467	10.631
Zn	2.158	4.400	9.226	0.105	2.933	8.728	2.136	4.400	9.285
Zn	6.298	4.400	10.567	4.244	2.933	9.860	6.408	4.400	10.631
Zn	3.294	1.467	12.008	1.149	0.000	11.351	3.302	1.467	11.977
Zn	0.202	1.467	13.329	5.448	0.000	12.645	0.196	1.467	13.322
Zn	3.294	4.400	12.008	1.149	2.933	11.351	3.302	4.400	11.977
Zn	0.202	4.397	13.329	5.448	2.933	12.645	0.196	4.400	13.322
Zn	4.468	1.467	14.668	2.332	0.000	13.995	4.468	1.467	14.668
Zn	1.362	1.467	16.014	6.604	0.000	15.341	1.362	1.467	16.014
Zn	4.468	4.400	14.668	2.332	2.933	13.995	4.468	4.400	14.668
Zn	1.362	4.400	16.014	6.604	2.933	15.341	1.362	4.400	16.014
Zn	5.634	1.467	17.359	3.498	0.000	16.686	5.634	1.467	17.360
Zn	2.528	1.467	18.705	0.392	0.000	18.032	2.528	1.467	18.705
Zn	5.634	4.400	17.359	3.498	2.933	16.686	5.634	4.400	17.359
Zn	2.528	4.400	18.705	0.392	2.933	18.032	2.528	4.400	18.705
Total Energy			-112.095			-112.118			-111.846

[a] Coordinates of unrelaxed $(221)^{Pd}$; for unrelaxed $(221)^{Zn}$, interchange Pd and Zn atoms.

In Tables C3 to C8, we provide the Cartesian coordinates (Å) of various adsorbed species on PdZn(221) slabs and the corresponding total energies (eV).

Table C3. Most favorable adsorption site of H, O, CH_3, CH_3O, and CH_2O on PdZn(221)

		$(221)^{Pd}$			$(221)^{Zn}$		
		X	y	z	x	y	z
H		7.077	1.467	7.867	2.799	2.933	8.523
Total energy				-115.832			-115.613
O		2.326	0.000	8.018	0.667	1.467	7.668
Total energy				-118.125			-118.817
CH_3	H	0.104	2.956	6.100	1.658	2.355	6.709
	H	5.985	3.765	6.709	1.658	0.578	6.709
	H	6.087	1.972	6.688	3.178	1.467	6.949
	C	6.656	2.902	6.820	2.105	1.467	7.172
Total energy				-131.992			-131.522
CH_3O	H	5.637	0.717	6.062	6.321	2.352	5.636
	H	6.973	1.451	5.086	6.321	0.581	5.636
	H	5.817	2.492	6.012	7.874	1.467	5.498
	C	6.384	1.539	6.036	6.882	1.467	5.976
	O	7.314	1.495	7.149	6.988	1.467	7.409
Total energy				-138.690			-139.312
CH_2O	H	4.415	5.730	7.196	2.086	3.310	6.858
	H	4.331	1.736	6.918	2.267	5.115	6.810
	C	4.946	0.828	7.071	1.731	4.270	7.250
	O	6.188	0.901	7.072	0.339	4.379	7.260
Total energy				-134.770			-134.809

Table C4. Transition states of $CH_3O \rightarrow CH_2O + H$ on $(221)^{Pd}$ and $(221)^{Zn}$

	$(221)^{Pd}$ terrace			$(221)^{Pd}$ edge			$(221)^{Zn}$		
	X	y	z	x	y	z	x	y	z
H	4.528	0.564	8.473	6.320	5.173	7.739	2.000	3.427	7.968
H	4.777	0.421	6.513	5.722	0.142	6.078	1.605	3.292	6.229
H	4.485	2.182	7.192	4.912	0.837	7.624	2.051	5.016	6.684
C	5.140	1.281	7.119	5.817	0.773	6.982	1.356	4.181	6.815
O	6.429	1.441	7.245	6.632	1.760	6.943	0.101	4.438	7.080
Total energy			-137.987			-137.969			-138.037

Table C5. Transition states of $CH_3O \rightarrow CH_3 + O$ on $(221)^{Pd}$

	$(221)^{Pd}$ terrace			$(221)^{Pd}$ terrace_2			$(221)^{Pd}$ edge		
	x	y	z	x	y	z	x	y	z
H	5.783	1.308	6.697	3.567	4.492	8.027	6.342	2.163	5.841
H	7.009	2.320	5.807	4.821	5.239	7.122	0.786	2.540	5.936
H	5.563	3.102	6.657	3.301	0.391	7.425	6.888	3.859	6.301
C	6.301	2.282	6.658	4.038	5.531	7.837	7.138	2.775	6.295
O	0.675	1.480	7.478	5.594	0.990	8.505	6.430	1.499	7.750
Total energy			-136.460			-135.712			-136.536

Table C6. Transition state and final states of $CH_3O \rightarrow CH_3 + O$ on $(221)^{Zn}$

	Transition state			Final state		
	x	y	z	x	y	z
H	1.839	2.372	6.508	1.721	2.357	6.782
H	1.839	0.561	6.508	1.721	0.576	6.782
H	3.262	1.467	7.200	3.262	1.467	6.990
C	2.175	1.467	7.045	2.188	1.467	7.219
O	0.336	1.467	7.500	6.360	1.467	8.212
Total energy			-136.948			-138.198

Table C7. Final states of $CH_3O \rightarrow CH_2O + H$ on $(221)^{Pd}$ and $(221)^{Zn}$

	$(221)^{Pd}$ terrace			$(221)^{Pd}$ edge			$(221)^{Zn}$		
	x	y	z	x	y	Z	x	y	z
H	4.077	4.398	8.936	7.339	4.377	7.805	2.800	2.901	8.612
H	4.416	5.731	7.195	4.588	5.772	7.181	2.179	3.633	6.968
H	4.332	1.735	6.917	4.266	1.716	6.747	2.090	5.448	6.795
C	4.948	0.828	7.070	4.992	0.924	7.018	1.695	4.497	7.162
O	6.186	0.900	7.071	6.203	1.166	7.094	0.322	4.410	7.229
Total energy			-138.159			-138.198			-138.140

Table C8. Final states of $CH_3O \rightarrow CH_3 + O$ on $(221)^{Pd}$

	$(221)^{Pd}$ terrace			$(221)^{Pd}$ terrace_2			$(221)^{Pd}$ edge		
	x	y	z	x	y	z	x	y	z
H	6.328	2.468	6.459	4.531	0.301	7.610	0.535	3.351	6.144
H	0.538	3.331	6.249	3.062	1.191	7.246	6.434	4.267	6.629
H	6.410	4.258	6.627	2.989	5.291	7.241	6.362	2.465	6.514
C	6.948	3.316	6.773	3.443	0.282	7.754	6.994	3.336	6.743
O	2.354	0.003	8.031	6.009	1.511	8.484	5.642	1.248	8.711
Total energy			-137.976			-137.132			-137.318

Table C9. Vibrational frequencies (cm^{-1}) of adsorbed CH_2O and the initial state (IS) of CH_3O on $(221)^{Pd}$ and $(221)^{Zn}$.

	CH_2O		IS	
	$(221)^{Pd}$	$(221)^{Zn}$	$(221)^{Pd}$	$(221)^{Zn}$
ν_1	2973	3080	2916	3004
ν_2	2892	3008	2878	2992
ν_3	1578	1453	2783	2928
ν_4	1444	1142	1453	1455
ν_5	1201	1089	1446	1453
ν_6	1006	883	1420	1420
ν_7	293	609	1124	1138
ν_8	230	423	1119	1119
ν_9	178	295	925	1138
ν_{10}	140	236	295	993
ν_{11}	93	169	281	317
ν_{12}	31	136	267	260
ν_{13}			201	149
ν_{14}			118	134
ν_{15}			64	86

Table C10. Vibrational frequencies (cm^{-1}) of transition states for C-H and C-O bond breaking of adsorbed CH_3O on $(221)^{Pd}$ and $(221)^{Zn}$.

	C-H bond breaking			C-O bond breaking			
	terrace	edge	$(221)^{Zn}$	terrace	Terrace_2	edge	$(221)^{Zn}$
ν_1	2896	2958	3082	3041	3032	3034	3019
ν_2	2795	2849	3014	3021	2859	2983	2988
ν_3	1482	1605	1543	2909	2364	2865	2912
ν_4	1429	1465	1478	1428	1493	1429	1429
ν_5	1244	1281	1287	1382	1322	1392	1385
ν_6	1200	1185	1173	1150	1084	1117	1215
ν_7	883	1065	1070	824	750	850	938
ν_8	725	780	977	690	713	746	771
ν_9	540	475	608	421	350	425	400
ν_{10}	321	334	328	342	332	378	384
ν_{11}	251	217	209	306	282	286	320
ν_{12}	241	198	146	190	193	206	273
ν_{13}	129	82	82	107	114	102	101
ν_{14}	9	25	66	45	45	39	46
ν_{15}	510*i*	699*i*	845*i*	513*i*	432*i*	488*i*	627*i*

Appendix D

Supplementary Material for Formaldehyde Dehydrogenation on (111) Surfaces of Pd, Cu and PdZn

In Tables D1 to D6, we provide the Cartesian coordinates (in Å) and the total energy (in eV) of the substrate with adsorbed species.

Table D1. $CH_2O \rightarrow CHO + H$ (Initial State)

	PdZn			Pd			Cu		
	x	y	z	x	y	z	x	y	Z
H	3.243	3.467	10.879	3.959	1.480	11.374	3.865	3.171	8.072
H	3.951	1.745	10.682	3.962	3.358	11.355	3.890	1.302	8.000
C	3.163	2.386	11.128	3.461	2.424	11.678	3.362	2.219	8.317
O	1.992	1.866	11.349	2.152	2.428	11.728	2.036	2.192	8.494
Total energy			-78.190			-101.822			-78.106

Table D2. $CH_2O \rightarrow CHO + H$ (Transition State)

	PdZn			Pd			Cu		
	x	y	z	x	Y	z	x	y	z
H	2.878	3.536	12.424	4.267	2.584	11.112	3.241	3.267	9.229
H	3.615	2.409	10.713	3.672	4.062	12.291	3.866	1.363	7.920
C	2.921	2.385	11.586	3.478	2.752	11.868	3.133	1.489	8.711
O	1.704	2.403	11.319	2.281	2.494	11.614	1.880	1.563	8.372
Total energy			-77.380			-101.431			-77.272

Table D3. $CH_2O \rightarrow CHO + H$ (Final State)

	PdZn			Pd			Cu		
	x	y	z	x	y	z	x	y	z
H	3.350	4.044	12.383	4.374	2.313	11.098	3.838	3.730	9.624
H	4.425	1.973	10.712	4.197	4.412	12.771	3.742	1.667	8.735
C	3.483	1.890	11.302	3.551	2.308	11.841	2.561	1.553	8.873
O	2.428	1.673	10.743	2.380	2.347	11.486	1.927	1.413	7.847
Total energy			-77.955			-102.085			-77.543

Table D4. $CHO \rightarrow CO + H$ (Initial State)

	PdZn			Pd			Cu		
	x	Y	z	x	y	z	x	y	z
H	4.737	3.097	10.829	5.208	3.003	11.382	4.708	2.718	7.854
C	3.853	2.522	11.200	4.281	2.472	11.713	3.849	2.222	8.363
O	3.096	2.031	10.397	3.482	2.013	10.940	2.972	1.716	7.688
Total energy			-74.435			-98.445			-74.135

Table D5. $CHO \rightarrow CO + H$ (Transition State)

	PdZn			Pd			Cu		
	x	Y	z	x	y	z	x	y	z
H	6.252	3.938	11.894	4.685	2.727	11.900	4.558	2.631	8.856
C	4.824	2.959	11.567	3.584	2.103	11.776	3.408	1.967	8.499
O	4.656	2.753	10.395	2.967	1.755	10.834	3.142	1.814	7.358
Total energy			-73.974			-97.824			-73.813

Table D6. $CHO \rightarrow CO + H$ (Final State)

	PdZn			Pd			Cu		
	x	Y	z	x	y	z	x	y	Z
H	6.327	4.143	12.291	7.008	4.046	10.589	6.389	3.688	9.652
C	3.725	2.439	11.359	2.810	1.622	10.074	2.574	1.486	9.030
O	3.756	2.459	10.205	2.797	1.615	8.888	2.576	1.487	7.854
Total energy			-74.899			-99.705			-74.960

Table D7. Frequencies (cm^{-1}) of initial state (IS) and transition state (TS) for C-H bond breaking of adsorbed formaldehyde.

	IS			TS		
	PdZn	Pd	Cu	PdZn	Pd	Cu
ν_1	2929	2937	2998	2841	2945	3116
ν_2	2860	2854	2914	1545	1503	1229
ν_3	1495	1436	1447	1296	1226	1115
ν_4	1271	1237	1114	1262	1087	1061
ν_5	1162	1138	1111	950	816	679
ν_6	990	916	814	840	660	597
ν_7	602	515	449	508	498	432
ν_8	341	423	362	242	277	283
ν_9	202	272	186	207	186	151
ν_{10}	150	155	107	107	130	72
ν_{11}	106	115	61	80	93	21
ν_{12}	41	44	17	557*i*	798*i*	541*i*

Table D8. Frequencies (cm^{-1}) of initial state (IS) and transition state (TS) for C-H bond breaking of adsorbed formyl.

	IS			TS		
	PdZn	Pd	Cu	PdZn	Pd	Cu
ν_1	2708	2792	2808	1685	1872	1845
ν_2	1707	1727	1643	906	1593	1327
ν_3	1198	1111	1198	420	694	439
ν_4	719	729	632	406	549	377
ν_5	410	476	328	292	229	202
ν_6	232	256	159	226	125	172
ν_7	129	126	123	99	57	60
ν_8	72	70	70	54	50	20
ν_9	30	41	21	824*i*	478*i*	717*i*

Appendix E

Estimation of Energy and Entropy Contributions

Table E1. The calculated vibrational frequencies (cm^{-1}) of adsorbed H, O, OH and H_2O on PdZn(111) and Cu(111) surfaces.

	H		O		OH		H_2O	
	PdZn	Cu	PdZn	Cu	PdZn	Cu	PdZn	Cu
ν_1	1008	1031	431	447	3693	3685	3710	3703
ν_2	935	846	398	324	543	438	3593	3603
ν_3	653	830	245	315	458	419	1559	1558
ν_4					324	367	401	406
ν_5					182	193	371	340
ν_6					157	177	204	125
ν_7							124	88
ν_8							85	75
ν_9							61	54

Table E2. The calculated F^{vib} (meV) at 500 K for adsorbed H, O, OH and H_2O on PdZn(111) and Cu(111) surfaces.

	PdZn	Cu
H	148	157
O	6	10
OH	205	203
H_2O	360	310

For the gases species, there are additional contribution form the rotational and translation motion to the Helmholtz energy. The translational partition function [125] is given by

$$q_{tran} = \left(\frac{2\pi mkT}{h^2} \right)^{3/2} V \tag{E.1}$$

The translational energy [125] is defined as

$$\begin{aligned} E^{tran}(T,V) &= kT^2 \frac{\partial}{\partial T} \ln q_{tran} \\ &= \frac{3}{2} kT \end{aligned}, \tag{E.2}$$

and the entropy contributaion [125] is given by

$$\begin{aligned} S^{tran}(T,V) &= k\left(\ln q_{tran} e + \left(\frac{E^{tran}}{kT} \right) \right) \\ &= k\left(\ln q_{tran} + 1 + \frac{3}{2} \right) \end{aligned} \tag{E.3}$$

With $F^{tran} = E^{tran} - TS^{tran}$

$$F^{tran}(T,V) = -kT\left(\ln q_{tran} + 1 \right) \tag{E.4}$$

Therefore, at 0 K, $F^{tran} = 0$. The rotational partition function [125] for non-linear molecule is given by

$$q_{rot} = \frac{\pi^{1/2}}{\sigma_r} \left(\frac{T^{3/2}}{\left(\theta_{rx} \theta_{ry} \theta_{rz} \right)^{1/2}} \right), \tag{E.5}$$

and for linear molecule is given by

$$q_{rot} = \frac{1}{\sigma_r} \left(\frac{T}{\theta_r} \right), \tag{E.6}$$

where σ_r is the symmetry number and $\theta_{rx} = h^2/(8\pi I_{rx}k)$, where I_{rx} is the moment of inertia. The rotational energy [125] contribution for non-linear molecule is then given by

$$E^{rot}(T) = kT^2 \frac{\partial}{\partial T} \ln q_{tran} = \frac{3}{2} kT \quad , \tag{E.7}$$

and for linear molecule, it is

$$E^{rot}(T) = kT \quad , \tag{E.8}$$

The rotational entropy [125] contribution for non-linear molecule is given by

$$S^{rot}(T) = k\left(\ln q_{rot} + \beta E^{rot}\right) = k\left(\ln q_{rot} + \frac{3}{2}\right) \quad , \tag{E.9}$$

and for linear molecule,

$$S^{rot}(T) = k\left(\ln q_{rot} + \beta E^{rot}\right) = k\left(\ln q_{rot} + 1\right) \quad , \tag{E.10}$$

With $F^{rot} = E^{rot} - TS^{rot}$, we have

$$F^{rot}(T) = -kT\left(\ln q_{rot}\right) \tag{E.11}$$

Therefore, at 0 K, $F^{rot} = 0$.

Table E3. The calculated vibrational frequencies (cm^{-1}) of gas phase H_2, O_2, and H_2O.

	H_2	O_2	H_2O
ν_1	3064	1094	3841
ν_2			3745
ν_3			1586

Table E4. The calculated $F^{vib}(0)$ (meV) for gas phase H_2, O_2 and H_2O.

	Gas phase
H_2	190
O_2	68
H_2O	569

Appendix F

Tabulated Thermodynamic Data

Table F1 shows the calculated chemical potential of species *i* at standard pressure (1 bar) obtained from thermodynamic tables [138] using equation G.1.

$$\mu_i(T, p_i^0) = \left[H(T, p_i^0) - H(0, p_i^0) \right] - T\left[S(T, p_i^0) - S(0, p_i^0) \right] \qquad \text{(F.1)}$$

Table F1. Tabulated values of enthalpy, ΔH (kJ mol^{-1}) and entropy, ΔS (J K^{-1} mol^{-1}) at pressure 0.1 MPa and the corresponding calculated chemical potential from Eq. G.1 for gas phase species H_2, O_2 and H_2O.

	ΔH(T-T_r[a])[b]	**ΔH(T_r[a]-0)[b]**	**ΔH(T-0)**	**ΔS(T-0)[b]**	**Δμ(T), kJ mol^{-1}**	**Δμ(T), eV**
H_2						
300 K	0.053	8.467	8.520	130.858	-30.74	-0.32
400 K	2.959		11.426	139.216	-44.26	-0.46
500 K	5.882		14.349	145.737	-58.52	-0.61
600 K	8.811		17.278	151.077	-73.37	-0.76
O_2						
300 K	0.054	8.683	8.737	205.329	-52.86	-0.55
400 K	3.025		11.708	213.871	-73.84	-0.77
500 K	6.084		14.767	220.693	-95.58	-0.99
600 K	9.244		17.927	226.451	-117.94	-1.22
H_2O						
300 K	0.062	9.904	9.966	189.042	-46.7	-0.48
400 K	3.452		13.356	198.788	-66.2	-0.69
500 K	6.925		16.829	206.534	-86.4	-0.90
600 K	10.501		20.405	213.052	-107.4	-1.11

[a] T_r is the reference temperature, 298.15 K.

[b] The values are obtained from the NIST-JANAF handbook [138].

Table F2 shows the calculated chemical potential with respect to various pressures using equation G.2.

$$\tilde{\mu}_i(T, p_i) = \mu_i\left(T, p^0\right) + k_B T \ln\left(\frac{p_i}{p^0}\right) \tag{F.2}$$

Table F2. Tabulated $\tilde{\mu}_{H2}$, $\tilde{\mu}_{O2}$, and $\tilde{\mu}_{H2O}$ (eV) calculated from Eq. G.2 at various temperatures and pressures.

	300 K	**400 K**	**500 K**	**600 K**
$\tilde{\mu}_{H2}$				
10^{-15} atm	-1.21	-1.65	-2.10	-2.55
10^{-10} atm	-0.91	-1.25	-1.60	-1.95
10^{-5} atm	-0.62	-0.86	-1.10	-1.36
10^{-2} atm	-0.44	-0.62	-0.81	-1.00
1 atm	-0.32	-0.46	-0.61	-0.76
$\tilde{\mu}_{O2}$				
10^{-15} atm	-1.44	-1.96	-2.48	-3.01
10^{-10} atm	-1.14	-1.56	-1.98	-2.41
10^{-5} atm	-0.85	-1.16	-1.49	-1.82
10^{-2} atm	-0.67	-0.92	-1.19	-1.46
1 atm	-0.55	-0.76	-0.99	-1.22
$\tilde{\mu}_{H2O}$				
10^{-15} atm	-1.38	-1.88	-2.38	-2.90
10^{-10} atm	-1.08	-1.48	-1.89	-2.30
10^{-5} atm	-0.78	-1.08	-1.39	-1.71
10^{-2} atm	-0.60	-0.84	-1.09	-1.35
1 atm		-0.69	-0.90	-1.11

Note that $\tilde{\mu}_H = 1/2\ \tilde{\mu}_{H2}$ and $\tilde{\mu}_O = 1/2\ \tilde{\mu}_{O2}$

Appendix G

Supplementary Material for OH and H_2O adsorption on PdZn(111) and Cu(111) Surfaces

Table G1. Total energy (eV) of molecules in vacuum and bulk metal

Species	H_2	O_2	OH	H_2O	Cu	PdZn
Total energy	-6.788	-9.788	-7.668	-14.274	-3.730	-3.735

In Tables G2 and G3, we provide the Cartesian coordinates (in Å) and the total energy, TE (in eV) of the substrate with adsorbed species. For the adsorption sites on PdZn(111), refer to Fig. 3.1. On Cu(111), site B^{Pd2} denotes a bridge site, F^{Pd2Zn} denotes an fcc site, H^{Pd2Zn} denotes an hcp site, T^{Pd} denotes a top site, and TBT^{Pd2} denotes a top-bridge-top site.

Table G2. OH/M(111)

Sites		PdZn				Cu			
		x	y	z	TE	x	y	z	TE
B^{Pd2}	H	4.543	1.222	8.440		0.642	1.110	7.996	
	O	4.543	1.219	9.413	-65.743	0.639	1.112	8.968	-66.484
B^{Zn2}	H	1.882	1.233	8.650					
	O	1.886	1.235	9.628	-66.395				
F^{Pd2Zn}	H	5.187	1.644	8.565		2.565	1.481	8.080	
	O	5.332	1.739	9.524	-66.049	2.565	1.481	9.054	-66.642
F^{PdZn2}	H	2.527	1.655	8.725					
	O	2.268	1.485	9.650	-66.430				
H^{Pd2Zn}	H	3.915	0.811	8.605		1.283	0.741	8.071	
	O	3.791	0.730	9.564	-66.162	1.283	0.741	9.045	-66.632
H^{PdZn2}	H	1.268	0.830	8.714					
	O	1.513	0.991	9.641	-66.335				
T^{Pd}	H	4.576	4.749	8.553		0.000	0.000	7.666	
	O	3.128	0.295	9.074	-65.710	0.000	0.000	8.632	-65.843
T^{Zn}	H	0.001	0.001	8.257					
	O	0.000	0.000	9.225	-65.753				

Table G3. H_2O/M(111)

Sites		PdZn				Cu			
		x	y	z	TE	x	y	z	TE
B^{Pd2}	H	3.602	1.277	8.382		6.261	2.073	7.467	-70.224
	H	4.882	2.115	8.378		2.627	1.996	7.814	
	O	4.577	1.191	8.351	-70.130	1.842	1.435	7.667	
B^{Zn2}	H	0.919	1.271	8.377					
	H	2.213	2.118	8.378					
	O	1.894	1.195	8.374	-70.150				
F^{Pd2Zn}	H	4.223	1.684	8.383		1.085	1.014	8.069	
	H	5.509	2.529	8.372		2.422	1.781	8.072	
	O	5.200	1.603	8.367	-70.135	2.049	0.879	7.948	-70.216
F^{PdZn2}	H	1.546	1.682	8.376					
	H	2.834	2.529	8.379					
	O	2.518	1.601	8.366	-70.129				
H^{Pd2Zn}	H	2.975	0.869	8.374		3.114	0.802	7.865	
	H	4.261	1.710	8.383		4.488	1.487	7.852	
	O	3.947	0.781	8.364	-70.118	4.061	0.619	7.706	-70.212
H^{PdZn2}	H	5.649	0.866	8.378					
	H	1.588	1.709	8.377					
	O	1.271	0.786	8.367	-70.144				
T^{Pd}	H	2.794	2.503	8.376		1.558	0.196	7.950	
	H	4.083	3.347	8.375		2.893	0.977	7.953	
	O	3.768	2.422	8.383	-70.198	2.527	0.700	8.009	-70.283
T^{Zn}	H	1.721	0.046	8.375					
	H	3.016	0.893	8.376					
	O	2.696	-0.030	8.391	-70.229				

Bibliography

[1] D. L. Trimm, Z. I. Önsan. On-board fuel conversion for hydrogen fuel cells: Comparison of different fuels by computer simulations. Catal. Rev. 43 (2001) 31.

[2] J. D. Holladay, Y. Wang, E. Jones. Review of developments in portable hydrogen production using microreactor technology. Chem. Rev. 104 (2004) 4767.

[3] J. Agrell, H. Birgersson, M. Boutonnet, I. Melián-Cabrera, R. M. Navarro, J. L. G. Fierro. Production of hydrogen from methanol over Cu/ZnO catalysts promoted by ZrO_2 and Al_2O_3. J. Catal. 219 (2003) 389.

[4] M. M. Günter, T. Ressler, R. E. Jentoft, B. Bems. Redox behavior of copper oxide/zinc catalysts in the steam reforming of methanol studied by in situ X-ray differaction and adsorption spectroscopy. J. Catal. 203 (2001) 133.

[5] N. Iwasa, N. Takezawa. New supported Pd and Pt alloy catalysts for steam reforming and dehydrogenation of methanol. Top. Catal. 22 (2003) 215.

[6] M. L. Cubeiro, J. L. G. Fierro. Selective production of hydrogen by partial oxidation of methanol over ZnO-supported padallium catalysts. J. Catal. 179 (1998) 150.

[7] Y.-H. Chin, R. Dagle, J. Hu, A. C. Dohnalkova, Y. Wang. Steam reforming of methanol over highly active Pd/ZnO catalyst. Catal. Today 77 (2002) 79.

[8] N. Iwasa, T. Mayanagi, S. Masuda, N. Takezawa. Steam reforming of methanol over Pd-Zn catalysts. React. Kinet. Catal. Lett. 69 (2000) 355.

[9] C. M. Friend, X. Xu. Reactions on transition metal surface. Annu. Rev. Phys. Chem. 42 (1991) 251.

[10] J.-J. Chen, Z. C. Jiang, Y. Zhou, B. R. Chakraborty, N. Winograd. Spectroscopic studies of methanol decomposition on Pd(111). Surf. Sci. 328 (1995) 248.

[11] F. Solymosi, A. Berko, Z. Toth. Adsorption and dissociation of CH_3OH on clean and K-promoted Pd(100) surfaces. Surf. Sci. 285 (1993) 197.

[12] M. Rebholz, N. J. Kruse. Mechanism of methanol decomposition on Pd(111). Chem. Phys. 95 (1991) 7745.

[13] N. Kruse, M. Rebholz, V. Matolin, G. K. Chuah, J. H. Block. Methanol decomposition on Pd(111) single crystal surfaces. Surf. Sci. 238 (1991) L457.

[14] R. J. Levis, Z. C. Jiang, N. Winograd. Evidence for activation of the carbon-oxygen bond of methanol on the padllium(111) surfaces after low temperature adsorption. J. Am. Chem. Soc. 110 (1988) 4431; 111 (1989) 4605.

[15] S. Schauermann, J. Hoffmann, V. Johanek, J. Hartmann, J. Libuda, H.-J. Freund. The molecular origins of selectivity in methanol decomposition on Pd nanoparticles. Catal. Lett. 84 (2002) 209.

[16] J. L. Davis, M. A. Barteau. Spectroscopic identification of alkoxide, aldehyde, and acyl intermediates in alcohol decomposition on Pd(111). Surf. Sci. 235 (1990) 235.

[17] K. R. Harikumar, C. P. Vinod, G. U. Kulkarni, C. N. R. Rao. Facile C-O bond scission in alcohols on Zn surfaces. J. Phys. Chem. B 103 (1999) 2445.

[18] J. K. Lee, J. B. Ko, D. H. Kim. Methanol steam reforming over $Cu/ZnO/Al_2O_3$ catalyst: Kinetics and effectiveness factor. Appl. Catal. A 278 (2004) 25.

[19] T. V. Choudhary, D. W. Goodman. CO-free fuel processing for fuel cell applications. Catal. Today 77 (2002) 65.

[20] P. Pfeifer, K. Schubert, M. A. Liauw, G. Emig. PdZn catalysts prepared by washcoating microstructured reactors. Appl. Catal. A 207 (2004) 165.

[21] N. Iwasa, T. Mayanagi, N. Ogawa, K. Sakata, N. Takezawa. New catalytic functions of Pd-Zn, Pd-Ga, Pd-In, Pt-Zn, Pt-Ga, and Pt-In alloys in the conversions of methanol. Catal. Letts. 54 (1998) 119.

[22] G. Wang, L. Jiang, Z. Cai, Y. Pan, X. Zhao, W. Huang, K. Xie, Y. Li, Y. Sun, B. Zhong. Surface structure sensitivity of the water-gas shift reaction on Cu(hkl) surfaces: A theoretical study. J. Phys. Chem. B 107 (2003) 557.

[23] A. H. Jones, S. Poulston, R. A. Bennett, M. Bowker. Methanol oxidation to formate on Cu(110) studied by STM. Surf. Sci. 380 (1997) 31.

[24] M. Bowker, E. Rowbotham, F. M. Leibsle, S. Haq. The adsorption and decomposition of formic acid on Cu(110). Surf. Sci. 349 (1996) 97.

[25] J. R. B. Gomes, J. A. N. F. Gomes, F. Illas. First-principles study of the adsorption of formaldehyde on the clean and atomic oxygen covered Cu(111) surface. J. Mol. Catal. A 170 (2001) 187.

[26] J. R. B. Gomes, J. A. N. F. Gomes. A DFT study of the methanol oxidation catalyzed by a copper surface. Surf. Sci. 471 (2001) 59.

[27] M. A. Henderson. The interaction of water with solid surface: Fundamental aspects revisited. Surf. Sci. Rep. 46 (2002) 1.

[28] C. T. Au, J. Breza, M. W. Roberts. Hydroxylation and dehydrogenation at Cu(111) surfaces. Chem. Phys. Lett. 66 (1979) 340.

[29] B. J. Hinch, L. H. Dubois. Stable and metastable phases of water adsorbed on Cu(111). J. Chem. Phys. 96 (1992) 3262.

[30] A. F. Carley, P. R. Davies, M. W. Roberts, N. Shukla, Y. Song, K. K. Thomas. The hydroxylation of Cu(111) and Zn(0001) Surfaces. Appl. Surf. Sci. 81 (1994) 265.

[31] M. Canepa, P. Canyini, E. Narducci, M. Salvietti, S. Terrni, L. Mattera. Coexistence of OH phases on Ag(110). Surf. Sci. 343 (1995) 176.

[32] K. Bedurftig, S. Volkening, Y. Wang, J. Wintterlin, K. Jacobi, G. Ertl. Vibrational and structural properties of OH adsorbed on Pt(111). J. Chem. Phys. 111 (1999) 11147.

[33] S. Kandoi, A. A. Gokhale, L. C. Grabow, J. A. Dumesic, M. Mavrikakis. Why Au and Cu are more selective than Pt for preferential oxidation of CO at low temperature. Catal. Letts. 93 (2004) 93.

[34] W. Koch, M. C. Holthausen. A chemist's guide to density functional theory. 2nd Ed. Wiley-VCH, Weinheim, 2001, p. 157-163.

[35] J. A. Pope. Nobel lecture: Quantum chemical models. Rev. Mod. Phys. 71 (1999) 1267.

[36] E. Schrödinger. An undulatory theory of the Mechanics of atoms and molecules. Phys. Rev. 28 (1926) 1049.

[37] P. A. M. Dirac. The quantum theory of the electron. Proc. Roy. Soc. London. A117 (1928) 610.

[38] P. Hohenberg, W. Kohn. Inhomogeneous electron gas. Phys. Rev. 136 (1964) B864.

[39] W. Kohn, L. J. Sham. Self-consistent equations including exchange and correlation effects. Phys. Rev. 140 (1965) A1133.

[40] P. W. Atkins, R. S. Friedman. Molecular quantum mechanics. 3rd Ed. Oxford University Press, Oxford, 1996.

[41] W. Koch, M. C. Holthausen. A chemist's guide to density functional theory. 2nd Ed. Wiley-VCH, Weinheim, 2001, p. 65-91.

[42] G. Kresse, J. Furthmüller. Efficient iterative schemes for ab initio total-energy calculations using a plane-wave basis set. Phys. Rev. B 54 (1996) 11169.

[43] G. Kresse, J. Hafner. Ab initio molecular dynamics for liquid metals. Phys. Rev. B 47 (1993) 558.

[44] G. Kresse, J. Furthmüller. Efficiency of ab initio total-energy calculations for metals and semiconductors using a plane-wave basis set. Comp. Mat. Sci. 6 (1999) 15.

[45] J. P. Perdew, Y. Wang. Accurate and simple analytic representation of the electron-gas correlation energy. Phys. Rev. B 45 (1992) 13244.

[46] P. E. Blöchl. Projector augmented-wave method. Phys. Rev. B 50 (1994) 17953.

[47] G. Kresse, D. Joubert. From ultrasoft pseduopotentials to the projector augmented-wave method. Phys. Rev. B 59 (1999) 1758.

[48] H. J. Monkhorst, J. D. Pack. Special points for Brillouin-zone integrations. Phys. Rev. B 13 (1976) 5188.

[49] M. Methfessel, A. T. Paxton. High-precision sampling for Brillouin-zone integration in metals. Phys. Rev. B 40 (1989) 3616.

[50] Z.-X. Chen, K. M. Neyman, A. B. Gordienko, N. Rösch. Surface structure and stability of PdZn and PtZn alloys: Density-functional slab model studies. Phys. Rev. B 68 (2003) 75417.

[51] M. Hansen. Costitution of Binary Alloys. 2nd ed. McGraw Hill, New York, 1958.

[52] G. Mills, H. Jónsson, G. K. Schenter. Reversible work transition state theory: Application to dissociative adsorption of hydrogen. Surf. Sci. 324 (1995) 305.

[53] H. Jónsson, G. Mills, K. W. Jacobsen. Classical and quantum dynamics in condensed phase simulations. B. J. Berne, G. Ciccotti and D. F. Coker (eds.), World Scientific: Singapore, 1998, p. 385.

[54] W. F. K. Wynne-Jones, H. Eyring. The absolute rate of reactions in condensed phases. J. Chem. Phys. 3 (1935) 492.

[55] T. L. Hill. An introduction to statistical theromodynamics. Dover, New York, 1986.

[56] G. A. Somorjai. Introduction to surface chemistry and catalysis. Wiley, New York, 1994.

[57] Y. Gauthier, M. Schmid, S. Padovani, E. Lundgren, V. Bus, G. Kresse, J. Redinger, P. Varga. Adsorption sites and ligand effect for CO on an alloy surface: A direct view. Phys. Rev. Lett. 87 (2001) 36103.

[58] E. Shustorovich. The bond-order conservation approach to chemisorption and heterogeneous catalysis: Applications and implications. Adv. Catal. 37 (1990) 101.

[59] A. D. Becke. Density-functional exchange-energy approximation with correct asymptotic behavior. Phys. Rev. A 38 (1988) 3098.

[60] J. P. Perdew. Density-functional approximation for the correction energy of the inhomogeneous electron gas. Phys. Rev. B 33 (1986) 8822; 34 (1986) 7406.

[61] I. V. Yudanov, K. M. Neyman, N. Rösch. Density functional study of Pd nanoparticles with subsurface impurities of light element atoms. Phys. Chem. Chem. Phys. 6 (2004) 116.

[62] K. M. Neyman, C. Inntam, N. Rösch. Adsorption of carbon on Pd clusters of nanometer size: A first principles theoretical study. J. Chem. Phys. 122 (2005) 174705.

[63] J. F. Paul, P. Sautet. Chemisorption and transformation of CHx fragments (x = 0-3) on a Pd(111) surface: A periodic density functional study. J. Phys. Chem. B 102 (1998) 1578.

[64] C. T. Au, C. F. Ng, M. S. Liao. Methane dissociation and syngas formation on Ru, Os, Rh, Pd, Pt, Cu, Ag and Au: A theoretical study. J. Catal. 185 (1999) 12.

[65] G. C. Wang, L. Jiang, Z. S. Cai, Y. M. Pan, N. J. Guan, Y. Wu, X. Z. Zhao, Y. W. Li, Y. H. Sun, B. Zhong. Interaction of the atoms (H, S, O, C) with the Cu(111) surfaces. J. Mol. Struct.: Theochem 589/590 (2002) 371.

[66] M. Mavrikakis, B. Hammer, J. K. Nørskov. Effect of strain on the reactivity of metal surfaces. Phys. Rev. Lett. 81 (1998) 2819.

[67] T. E. Felter, E. C. Sowa, M. A. Van Hove. Location of hydrogen adsorbed on palladium (111) studied by low-energy electron diffraction. Phys. Rev. B 40 (1989) 891.

[68] W. Dong, V. Ledentu, P. Sautet, A. Eichler, J. Hafner. Hydrogen adsorption on palladium: A comparative theoretical study of different surfaces. Surf. Sci. 411 (1998) 123 and references therein.

[69] M. Wilde, M. Matsumoto, K. Fukuani, T. Aruga. Depth-resolved analysis of subsurface hydrogen absorbed by Pd(100). Surf. Sci. 482-485 (2001) 346.

[70] M. Morkel, G. Rupprechter, H-J Freund. Finite size effects on supported Pd nanoparticles: Interaction of hydrogen with CO and C_2H_4. Surf. Sci. 588 (2005) L209.

[71] K. H. Lim, N. Rösch, unpublished.

[72] J. Greeley, M. Mavrikakis. Methanol decomposition on Cu(111): A DFT study. J. Catal. 208 (2002) 291.

[73] A. Steltenpohl, N. Memmel. Adsorption site of oxygen on Pd(111). Surf. Sci. 443 (1999) 13.

[74] A. P. Seitsonen, Y. D. Kim, S. Schwegmann, H. Over. Comprehensive characterization of the (2x2)-O and the CO-induced (Sqrt(3)xSqrt(3))R30°-O overlayers on Pd(111). Surf. Sci. 468 (2000) 176.

[75] K. Honkala, K. Laasonen. Ab initio study of O_2 precursor states on the Pd(111) surface. J. Chem. Phys. 115 (2001) 2297.

[76] D. Loffreda, D. Simon, P. Sautet. Molecular and dissociative chemisorption of NO on palladium and rhodium (100) and (111) surfaces: A density-functional periodic study. J. Chem. Phys. 108 (1998) 6447.

[77] L. H. Dubois. Oxygen chemisorption and cuprous oxide formation on Cu(111) : A high resolution EELS study. Surf. Sci. 119 (1982) 399.

[78] J. Haase, H.-J. Kuhr. Reconstruction and relaxation of the oxygen-covered Cu(111) surface: A SEXAFS study. Surf. Sci. 203 (1988) L695.

[79] Y. Xu, M. Mavrikakis. The adsorption and dissociation of O_2 molecular precursors on Cu: The effect of steps. Surf. Sci. 538 (2003) 219.

[80] J. Greeley, J. K. Nørskov, M. Mavrikakis. Electronic structure and catalysis on metal surfaces. Annu. Rev. Phys. Chem. 53 (2002) 319.

[81] K. M. Neyman, R. Sahnoun, C. Inntam, S. Hengrasmee, N. Rösch. Computational study of model Pd-Zn nanoclusters and their adsorption complexes with CO molecules. J. Phys. Chem. B 108 (2004) 5424.

[82] G. Blyholder, Molecular orbital view of chemisorbed carbon monoxide. J. Phys. Chem. 68 (1964) 2772.

[83] A. Föhlisch, M. Nyberg, P. Bennich, L. Triguero, J. Hasselström, O. Karis, L. G. M. Pettersson, A. Nilsson. The bonding of CO to metal surfaces. J. Chem. Phys. 112 (2000) 1946.

[84] P. Sautet, M. K. Rose, J. C. Dunphy, S. Behler, M. Salmeron. Adsorption and energetics of isolated CO molecules on Pd(111). Surf. Sci. 453 (2000) 25.

[85] D. Loffreda, D. Simon, P. Sautet. Dependence of stretching frequency on surface coverage and adsorbate-adsorbate interactions: A density-functional theory approach of CO on Pd(111). Surf. Sci. 425 (1999) 68.

[86] N. Lopez, J. K. Nørskov. Synergetic effects in CO adsorption on Cu-Pd(111) alloys. Surf. Sci. 477 (2001) 59.

[87] J. A. Rodriguez. Interactions in bimetallic bonding: Electronic and chemical properties of PdZn surfaces. J. Phys. Chem. 98 (1994) 5758.

[88] J. Araña, N. Homs, J. Sales, J. L. G. Fierro, P. Ramirez de la Piscina. CO/CO_2 hydrogenation and ethylene hydroformylation over silica-supported PdZn Catalysts. Catal. Lett. 72 (2001) 183.

[89] S. H. Vosko, L. Wilk, M. Nusair. Accurate spin-dependent electron liquid correction energies for local spin-density calculations – A critical analysis. Can. J. Phys. 58 (1980) 1200.

[90] M. Pascal, C. L. A. Lamont, M. Kittel, J. T. Hoeft, L. Constant, M. Polcik, A. M. Bradshaw, R. L. Toomes, D. P. Woodruff. Methyl on Cu(111) – structural determination including influence of co-adsorbed iodine. Surf. Sci. 512 (2002) 173.

[91] B. Hammer, L. B. Hansen, J. K. Nørskov. Improved adsorption energetics within density-functional theory using Perdew-Burke-Ernzerhof functionals. Phys. Rev. B 59 (1999) 7413. Often, this GGA functional, commonly referred to as RPBE, yields binding energies smaller than those obtained in PW91 calculations. Our PW91 binding energies are close to results of other studies using that same functional (Ref. 93), but lower than the RPBE binding energy reported in Ref. 92. The reason for this unusual situation is not clear. Note that in Ref. 92 a five-layer slab model of coverage 1/3 was studied, whereas we used a four-layer model at coverage 1/4.

[92] R. Robinson, D. P. Woodruff. The local adsorption geometry of CH_3 and NH_3 on Cu(111): A density functional theory study. Surf. Sci. 498 (2002) 203.

[93] A. Michaelides, P. Hu. Softened C-H modes of adsorbed methyl and their implications for dehydration: An ab initio study. J. Chem. Phys. 114 (2001) 2523.

[94] G. Papoian, J. K. Nørskov, R. Hoffmann. A comparative theoretical study of the hydrogen, methyl, and ethyl chemisorption on the Pt(111) surface. J. Am. Chem. Soc. 122 (2000) 4129.

[95] M. Mavrikakis, M. A. Barteau. Oxygenated reaction pathways on transition metal surfaces. J. Mol. Catal. A 131 (1998) 135.

[96] J. Kua, G. A. III Goddard. “Oxidation of methanol and 2nd and 3rd row group VIII transition metals (Pt, Ir, Os, Pd, Rh and Ru): Application to direct methanol fuel cells. J. Am. Chem. Soc. 121 (1999) 10928.

[97] M. Neurock. First-principles analysis of the hydrogenation of carbon monoxide over palladium. Top. Catal. 9 (1999) 135.

[98] R. Schennach, A. Eichler, K. D. Rendulic. Adsorption and desorption of methanol on Pd(111) and on a Pd/V surface alloy. J. Phys. Chem. B 107 (2003) 2552. Deviations from the present results are due to small differences in the model. These authors used a four-layer slab model of coverage 1/6 where the structure of the two top layers was relaxed.

[99] S. K. Desai, M. Neurock, K. Kourtakis. A periodic density functional study of the dehydrogenation of methanol over Pt(111). J. Phys. Chem. B 106 (2002) 2559. These authors used a three-layer slab model of coverage 1/4 with the two top layers relaxed.

[100] J. L. Davis, M. A. Barteau. Polymerization and decarbonylation reaction of aldehydes on the Pd(111) surface. J. Am. Chem. Soc. 111 (1989) 1782.

[101] K. Amemiya, Y. Kitajima, Y. Yonamoto, S. Terada, H. Tsukabayashi, T. Yokoyama, T. Ohta. Oxygen K-edge x-ray-absorption fine-structure study of surface methoxy species on Cu(111) and Ni(111). Phys. Rev. B 59 (1999) 2307 and references therein.

[102] Ph. Hofmann, K.-M. Schindler, S. Bao, V. Fritzschem, D. E. Ricken, A. M. Bradshaw, D. P. Woodruff. The geometric structure of the surface methoxy species on Cu(111). Surf. Sci. 304 (1994) 74.

[103] S. M. Johnston, A. Mulligan V. Dhanak, M. Kadodwala. The structure of methanol and methoxy on Cu(111). Surf. Sci. 530 (2003) 111.

[104] J. R. B. Gomes, J. A. N. F. Gomes. Comparative study of geometry and bonding character for methoxy radical adsorption on noble metals. J. Mol. Struct.: Theochem 503 (2000) 189.

[105] J. R. B. Gomes, J. A. N. F. Gomes, F. Illas. Methoxy radical reaction to formaldehyde on clean and hydroxy radical-covered copper (111) surfaces: A density functional theory study. Surf. Sci. 443 (1999) 165.

[106] M. Witko, K. Hermann. Site-dependent binding of methoxy on Cu(111): Cluster model studies. J. Chem. Phys. 101 (1994) 10173.

[107] A. Alavi, P. J. Hu, T. Deutsch, P. L. Silverstrelli, J. Hutter. “CO oxidation on Pt(111): An ab initio density functional theory study. Phys. Rev. Lett. 80 (1998) 3650.

[108] J. Greeley, M. Mavrikakis. Competitive paths for methanol decomposition on Pt(111). J. Am. Chem. Soc. 126 (2004) 3910.

[109] L. J. Richter, B. A. Gurney, J. S. Villarrubia, W. Ho. Temperature programmed electron energy loss spectroscopy: Kinetics of CH_3OH decomposition on Ni(110). Chem. Phys. Lett. 111 (1984) 185.

[110] J. Libada, H-J Freund. Molecular beam experiments on model catalysts. Surf. Sci. Reports 57 (2005) 157.

[111] Z. P. Liu, P. Hu. General rules for predicting where a catalytic reaction should occur on metal surfaces: A density functional theory study of C-H and C-O bond breaking/ making on flat, stepped, and kinked metal surfaces. J. Am. Chem. Soc. 125 (2003) 1958.

[112] M. Bron, D. Teschner, A. Knop-Gericke, B. Steinhauer, A. Scheybal, M. Hävecker, D. Wang, R. Födisch, D. Hönicke, A. Wootsch, R. Schlögl, P. Claus. Bridging the pressure and material gap: In-depth characterization and reaction studies of silver-catalysed acrolein hydrogenation. J. Catal. 234 (2005) 37.

[113] R. D. Ramsier, q. Gao, H. Neergaard Waltenburg, J. T. Yates, Jr.. Thermal dissociation of NO on Pd surfaces: The influence of step sites. J. Chem. Phys. 100 (1994) 6837.

[114] S. Dahl, A. Logadottir, R. C. Egeberg, J. H. Larsen, I. Chorkendorff, E. Törnqvist, J. K. Nørskov. Role of steps in N_2 activation on Ru(0001). Phys. Rev. Letts. 83 (1999) 1814.

[115] B. Hammer. Adsorption, diffusion and dissociation of NO, N and O on flat and stepped Ru(0001). Surf. Sci. 459 (2000) 323.

[116] C. Cao, G. Xia, J. Holladay, E. Jones, Y. Wang. Kinetic studies of methanol steam reforming over Pd/ZnO catalyst using a microchannel reactor. Appl. Catal. A 19 (2004) 262.

[117] I. Chorkendorff, J. W. Niemantsverdriet. Concepts of modern catalysis and kinetics. Wiley-VCH , Weinheim, 2003, p. 65.

[118] A. Gil, A. Clotet, J. M. Ricart, G. Kresse, M. García-Hernández, N. Rösch, P. Sautet. Site Preference of CO Chemisorbed on Pt(111) from Density Functional Calculations. Surf. Sci. 530 (2003) 71.

[119] K. M. Neyman, F. Illas. Theoretical aspects of heterogeneous catalysis: Applications of density functional methods. Catal. Today 105 (2005) 2.

[120] J. R. B. Gomes, J. A. N. F. Gomes. Adsorption of the formyl species on transition metal surface. J. Electroanal. Chem. 483 (2000) 180.

[121] S. Liu, K. Takahashi, K. Uematsu, M. Ayabe. Hydrogen production by oxidative methanol reforming on Pd/ZnO. Appl. Catal. A 283 (2005) 125.

[122] T. S. Askgaard, J. K. Norskov, C. V. Ovesen, P. Stoltze. A kinetic model of methanol synthesis. J. Catal. 156 (1995) 229.

[123] N. Iwasa, H. Suzuki, M. Terracita, M. Arai, N. Takezawa. Methanol synthesis from CO2 under atmospheric pressure over supported Pd catalysts. Catal. Letts. 68 (2004) 7514.

[124] K. Reuter, C. Stampfl, M. Scheffler. Ab initio atomistic thermodynamics and statistical mechanics of surface properties and functions, in Handbook of materials modeling, Part A Methods, S. Yip Ed. Springer, Berlin, 2005, pg. 149–194.

[125] D. A. McQuarrie, J. D. Simon. Molecular thermodynamics. University Science Book, California 1999, Chapter 4, p. 143–168.

[126] X.-G. Wang, A. Chaka, M. Scheffler. Effect of the environment on α-Al_2O_3(0001) surface structures. Phys. Rev. Letts. 84 (2000) 3650.

[127] K. Reuter, M. Scheffler. Composition, structure, and stability of RuO_2(110) as a function of oxygen pressure. Phys. Rev. B 65 (2001) 35406.

[128] K. Reuter, M. Scheffler. Effect of a humid environment on the surface structure of RuO_2(110). Phys. Rev. B 67 (2003) 205424.

[129] K. Reuter, M. Scheffler. First-principles atomistic thermodynamics for oxidation catalysis: Surface phase diagrams and catalytically interesting regions. Phys. Rev. Letts. 90 (2003) 46103.

[130] K. Reuter, M. Scheffler. Composition and structure of the RuO_2(110) surface in an O_2 and CO environment: Implications for the catalytic formation of CO_2. Phys. Rev. B 68 (2003) 45407.

[131] G. Kresse, O. Dulub, U. Diebold. Competing stabilization mechanism for the polar ZnO(0001)-Zn surface. Phys. Rev. B 68 (2003) 245409.

[132] W.-X. Li, C. Stampfl, M. Scheffler. Why a noble metal catalytically active? The role of the O-Ag interaction in the function of silver as an oxidation catalyst. Phys. Rev. Letts. 90 (2003) 256102.

[133] W.-X. Li, C. Stampfl, M. Scheffler. Insights into the function of silver as an oxidation catalyst by ab initio atomistic thermodynamics. Phys. Rev. B 68 (2003) 165412.

[134] K. Reuter, M. Scheffler. Oxide formation at the surface of late 4d transition metals: ingights from first-principles atomistic thermodynamics. Appl. Phys. A. 78 (2004) 793.

[135] E. Lundgren, J. Gustafson, A. Mikkelsen, J. N. Andersen, A. Stierle, H. Dosch, M. Todorova, J. Rogal, K. Reuter, M. Scheffler. Kinetic Hinderance during the initial oxidation of Pd(100) at ambient pressure. Phys. Rev. Letts. 92 (2004) 46101.

[136] J. Rogal, K. Reuter, M. Scheffler, Thermodynamic stability of PdO surfaces. Phys. Rev. B, 69 (2004) 75421.

[137] D. A. McQuarrie, J. D. Simon. Molecular thermodynamics. University Science Book, California 1999, p. 308.

[138] M. W. Chase, Jr, NIST-JANAF Thermochemical Tables, 4th ed., National Institute of Standards and Technology, 1998.

[139] P. W. Atkins. Physical chemistry. ELBS, Great Britain, 4th Edn. 1990, p. 164.

[140] J. P. Perdew, K. Burke, M. Ernzerhof. Generalized gradient approximation made simple. Phys. Rev. Letts. 77 (1996) 3685.

[141] D. R. Lide (ed.). CRC handbook of chemistry and physics. CRC Press, London, 77th Edn. 1996.

[142] M. Nakamura, M. Ito. Monomer and tetramer water clusters adsorbed on Ru(0001). Chem. Phys. Letts. 325 (2000) 293.

[143] A. Michaelides, A. Alavi, D. A. King. Different surface chemistries of water on Ru(0001): From monomer adsorption to partially dissociated bilayers. J. Am. Chem. Soc. 125 (2003) 2746.

[144] A. Michaelides, P. Hu. Catalytic water formation on platinum: A first-principles studies. J. Am. Chem. Soc. 123 (2001) 4235.

[145] P. J. Feibelman. Partial dissociation of water on Ru(0001). Science 295 (2002) 99.

[146] A. Michaelides, A. Alavi, D. A. King. Insight into H_2O-ice adsorption and dissociation on metal surfaces from first-principles simulations. Phy. Rev. B 69 (2004) 113404.

[147] W. Koch, M. C. Holthausen. A chemist's guide to density functional theory. Wiley-VCH: Weinheim, 2000. p. 117.

[148] I. V. Yudanov, R. Sahnoun, K. M. Neyman, N. Rösch. Metal nanoparticles as models of single crystal surfaces and supported catalysts: Density functional study of size effects for CO/Pd(111). J. Chem. Phys. 117 (2002) 9887.

[149] P. H. Matter, U. S. Ozkan. Effect of pretreatment conditions on Cu/Zn/Zr-based catalysts for steam reforming of methanol to H_2. J. Catal. 234 (2005) 463.

[150] I. Chorkendorff, J. W. Niemantsverdriet. Concepts of modern catalysis and kinetics. Wiley, Weinheim, 2003. p. 290.

[151] S. R. Samms, R. F. Savinell. Kinetics of methanol-steam reforming in an internal reforming fuel cell. J. Power Sources 112 (2002) 13.